NASA/CR–2014-218147

Active Vibration Control for Helicopter Interior Noise Reduction Using Power Minimization

J. Mendoza, K. Chevva, F. Sun, A. Blanc, and S. B. Kim
United Technologies Research Center, East Hartford, Connecticut

January 2014

NASA STI Program . . . in Profile

Since its founding, NASA has been dedicated to the advancement of aeronautics and space science. The NASA scientific and technical information (STI) program plays a key part in helping NASA maintain this important role.

The NASA STI program operates under the auspices of the Agency Chief Information Officer. It collects, organizes, provides for archiving, and disseminates NASA's STI. The NASA STI program provides access to the NASA Aeronautics and Space Database and its public interface, the NASA Technical Report Server, thus providing one of the largest collections of aeronautical and space science STI in the world. Results are published in both non-NASA channels and by NASA in the NASA STI Report Series, which includes the following report types:

- TECHNICAL PUBLICATION. Reports of completed research or a major significant phase of research that present the results of NASA Programs and include extensive data or theoretical analysis. Includes compilations of significant scientific and technical data and information deemed to be of continuing reference value. NASA counterpart of peer-reviewed formal professional papers, but having less stringent limitations on manuscript length and extent of graphic presentations.

- TECHNICAL MEMORANDUM. Scientific and technical findings that are preliminary or of specialized interest, e.g., quick release reports, working papers, and bibliographies that contain minimal annotation. Does not contain extensive analysis.

- CONTRACTOR REPORT. Scientific and technical findings by NASA-sponsored contractors and grantees.

- CONFERENCE PUBLICATION. Collected papers from scientific and technical conferences, symposia, seminars, or other meetings sponsored or co-sponsored by NASA.

- SPECIAL PUBLICATION. Scientific, technical, or historical information from NASA programs, projects, and missions, often concerned with subjects having substantial public interest.

- TECHNICAL TRANSLATION. English-language translations of foreign scientific and technical material pertinent to NASA's mission.

Specialized services also include organizing and publishing research results, distributing specialized research announcements and feeds, providing information desk and personal search support, and enabling data exchange services.

For more information about the NASA STI program, see the following:

- Access the NASA STI program home page at *http://www.sti.nasa.gov*

- E-mail your question to help@sti.nasa.gov

- Fax your question to the NASA STI Information Desk at 443-757-5803

- Phone the NASA STI Information Desk at 443-757-5802

- Write to:
  STI Information Desk
  NASA Center for AeroSpace Information
  7115 Standard Drive
  Hanover, MD 21076-1320

NASA/CR–2014-218147

Active Vibration Control for Helicopter Interior Noise Reduction Using Power Minimization

J. Mendoza, K. Chevva, F. Sun, A. Blanc, and S. B. Kim
United Technologies Research Center, East Hartford, Connecticut

National Aeronautics and
Space Administration

Langley Research Center
Hampton, Virginia 23681-2199

Prepared for Langley Research Center
under Contract NNL11AA06C

January 2014

Available from:

NASA Center for AeroSpace Information
7115 Standard Drive
Hanover, MD 21076-1320
443-757-5802

Abstract

This report describes work performed by United Technologies Research Center (UTRC) for NASA Langley Research Center (LaRC) under Contract NNL11AA06C. The objective of this program is to develop technology to reduce helicopter interior noise resulting from multiple gear meshing frequencies. A novel active vibration control approach called Minimum Actuation Power (MAP) is developed. MAP is an optimal control strategy that minimizes the total input power into a structure by monitoring and varying the input power of controlling sources. MAP control was implemented without explicit knowledge of the phasing and magnitude of the excitation sources by driving the real part of the input power from the controlling sources to zero. It is shown that this occurs when the total mechanical input power from the excitation and controlling sources is a minimum. MAP theory is developed for multiple excitation sources with arbitrary relative phasing for single or multiple discrete frequencies and controlled by a single or multiple controlling sources. Simulations and experimental results demonstrate the feasibility of MAP for structural vibration reduction of a realistic rotorcraft interior structure. MAP control resulted in significant average global vibration reduction of a single frequency and multiple frequency excitations with one controlling actuator. Simulations also demonstrate the potential effectiveness of the observed vibration reductions on interior radiated noise.

Acknowledgements

The authors would like to acknowledge the technical support and leadership of Ran Cabell and the project support of Susan Gorton from the NASA Langley Research Center. This work was sponsored by the NASA Subsonic Rotary Wing Project under the Fundamental Aeronautics Program. The authors would also like to acknowledge Paul Braunwart and Kenji Homma from UTRC for their help with the experiments and thank Bill Welsh and Tom Millott of Sikorsky Aircraft Corporation for their active participation in the program providing insights into practical helicopter interiors, dynamics, and controls.

Contents

List of Figures

List of Tables

Nomenclature

Variables

L_x	length of the plate
L_y	width of the plate
H	thickness of the plate
m	mass of the plate
ρ	mass density of the plate
E	elastic modulus of the plate
μ	poison ratio for the plate
η	structural damping of the plate
a	width of the PZT patch
h	thickness of the PZT patch
d_{31}	piezoelectric coupling coefficient between x and z axes
d_{32}	piezoelectric coupling coefficient between y and z axes
Y_{11}	elastic modulus of PZT patch
ε_{33}	complex dielectric constant of the PZT patch
$\bar{\varepsilon}_{33}$	real part of ε_{33}
δ	dielectric loss factor
ν_p	poison ratio for the PZT patch
Δe	discretization of the patch edge
$\bar{M}_p$	line moment per unit length (complex amplitude) generated by the primary patch
$\bar{M}_s$	line moment per unit length (complex amplitude) generated by the secondary patch
M_p	line moment (complex amplitude) generated by the primary patch element
M_s	line moment (complex amplitude) generated by the secondary patch element
$\bar{\mathrm{V}}_p$	voltage (complex amplitude) applied to primary patch
$\bar{\mathrm{V}}_s$	voltage (complex amplitude) applied to secondary patch
$\bar{P}$	time average total input power
$\bar{P}_p$	total input power due to the primary patch
$\bar{P}_s$	total input power due to the secondary patch
$\bar{P}_{se}$	net electrical power in the secondary patch

P_{pp}	equivalent point angular mobility for the primary patch
P_{ss}	equivalent point angular mobility for the secondary patch
P_{ps}	equivalent transfer angular mobility for the primary patch due to the secondary patch
P_{sp}	equivalent transfer angular mobility for the secondary patch due to the primary patch
S_{pp}	real part of P_{pp}
S_{ss}	real part of P_{ss}
S_{ps}	real part of P_{ps}
S_{sp}	real part of P_{sp}
ω	excitation frequency
ω_n	n^{th} resonant frequency
f	point force
f_k	component of f with frequency ω_k
v	transverse velocity
v_k	component of v with frequency ω_k
$\bar{P}_k$	average input power corresponding to ω_k
F	complex amplitude of f
R	real part of linear mobility
E	global energy of plate
$\overline{E}_{kin}$	time averaged global kinetic energy
$\overline{E}_{pot}$	time averaged global potential energy
$\overline{E}_{kin}^{opt}$	time averaged global vibrational energy with MAP control
$\overline{E}_{kin}^{red}$	normalized reduction in vibrational energy
$\overline{E}_{kin}^{k}$	time averaged global vibrational energy corresponding to ω_k

Subscripts

e	electrical
p	primary excitation
s	secondary excitation
pp	at primary location due to primary excitation
ss	at secondary location due to secondary excitation
ps	at primary location due to secondary excitation
sp	at secondary location due to primary excitation

Acronyms

MAP	Minimum Actuation Power
AVC	Active Vibration Control
ANC	Active Noise Control
ACSR	Active Control of Structural Response
ASAC	Active Structural Acoustic Control
PZT	Piezoelectric
SOW	Statement of Work

Chapter 1

Executive Summary

The objective of this work was to develop and demonstrate an approach for active vibration reduction on a rotorcraft structure to reduce noise in the passenger cabin of the rotorcraft. Vibration reduction at frequencies where gear-mesh tones and harmonics occur (500–2000 Hz) due to structure-borne excitation from the main gearbox is of interest to the rotorcraft cabin noise community. The proposed work developed and demonstrated a control methodology that is simpler to implement than traditional control approaches and potentially more robust and reliable for on-board implementation. Successful completion of this 3 year program will assist NASA in addressing the goals of the Quiet Cabin Technical Challenge within the Subsonic Rotary Wing project, where methods and concepts are sought-after that can be applied to or integrated into the structure to reduce rotorcraft cabin noise.

Conventional active vibration control (AVC)/active noise control (ANC) typically incorporates a sensor array for monitoring the vibratory or acoustic response, a controller, and control actuators. In many cases, applications of active control are hampered by the added system complexity, reduced reliability, and potential weight penalty. A novel approach to AVC/ANC, Minimum Actuation Power (MAP), is demonstrated that results in control of a single scalar objective, simpler and faster real time implementation through monitoring and adjusting the electrical input power of the control actuator and reduced hardware for

distributed vibratory response sensing, as compared with the conventional approach. MAP control features the following principle characteristics; 1) formulating the AVC process as real power control between vibration sources and actuators, 2) suppressing vibration by minimizing the total input power as the sole objective function, and 3) eliminating the need for error sensing by using the reactive nature of actuator for self-sensing of vibratory response.

The theory of Minimum Actuation Power (MAP) was first developed for a structure excited by a single primary (disturbance) source and controlled by a single secondary (control) source. It was shown that the real input(mechanical) power in the secondary source goes exactly to zero when the total input power from both the primary and secondary source is minimized. This leads to a novel way to implement MAP control without explicit knowledge about the magnitude and location of the primary excitation. In order to validate the theoretical findings, a model for a simply supported plate excited by a primary piezo-electric (PZT) patch actuator and controlled by a secondary piezo-electric patch actuator was developed. An electromechanical coupling model of piezoelectric patch actuator with a structure is developed and integrated with plate MAP model. A simple relation between the real electrical power and the real input power of the piezo-electric actuator was developed. This enabled implementing MAP control using the real electric power in the secondary actuator. The effectiveness of MAP control was demonstrated for resonant and off-resonant excitation frequencies. It was shown through simulations that optimizing the location of the secondary actuator can help control otherwise uncontrolled modes very effectively. The MAP theory was extended to multi-frequency excitation and simulations were presented to validate the theory. A test setup that mimics simply supported boundary conditions was built to validate the theoretical findings. To implement MAP using electrical power, tests were done to characterize the power consumption of the plate and the dielectric loss of the piezo-electric patch actuators. The MAP control algorithm was tested for on-resonance and off-resonance frequencies and effectiveness of MAP for vibration reduction. We demonstrated up to 47 dB vibration reduction at resonance and 7 dB vibration reduction at off-resonance, as measured by a single accelerometer at the plate center. There was good qualitative agreement between the experimental results and theoretical findings.

The MAP control approach was extended to multiple primary excitations with zero relative phasing and multiple secondary excitations. It was shown that when the primary excitations have the same phasing, then the real secondary power is zero when the total input power is

minimized. However, when the primary excitations have arbitrary phasing, the secondary real power is not always zero when the total input power is minimized. One way the MAP condition is satisfied is when the secondary sources are located symmetrically with respect to the primary sources. In general, such a symmetry constraint is difficult to satisfy for arbitrary locations of the primary sources. An electro-mechanical model for a simply supported plate excited by multiple primary and multiple secondary PZT patch actuators was developed. Performance of MAP control as a function of the location and number of the secondary sources was assessed. It was seen that increasing the number of secondary sources improves vibration reduction. Also, multiple secondary sources can be useful when vibration reduction over a frequency band is sought. Experimental validation of MAP control was demonstrated in the lab with two primary and two secondary excitations using an aluminum plate as well as a composite panel. For example, we demonstrated 20 dB vibration reduction for the aluminum plate and 12 dB vibration reduction for the composite plate, as measured by a single accelerometer at the plate center.

The feasibility of MAP control approach for reducing airframe vibrations due to the rotorcraft main rotor transmission and the reduction of corresponding sound levels in the passenger cabin was assessed using a more meaningful metric for vibration reduction, the global kinetic energy of the plate structure. MAP feasibility was assessed for multiple primary excitation sources with arbitrary relative phasing and with multiple frequencies controlled by multiple secondary sources. In order to circumvent the problem of placing the secondary actuators symmetrically with respect to the primary sources to satisfy the MAP condition, it was shown that placing the the secondary sources at the intersection of the node lines of the neighboring modes can guarantee that the secondary real power is zero at optimal conditions even when the primary sources have arbitrary phasing. An algorithm to compute the optimal secondary phase and magnitude was developed for resonant and off-resonant excitation frequencies. A stable iterative solution for finding the MAP solution for multiple secondary sources was developed. The stable iterative solution, however, is not feasible for a large number of secondary sources. An alternative feasible approach was developed to find the MAP solution when the secondary sources are large in number. A test rig representative of a rotorcraft interior structure was designed, modeled and built. MAP control was successfully demonstrated with primary excitation using shaker, in addition to PZT, with multiple frequencies and multiple secondary actuators for control. It was shown that MAP control achieved significant vibration reduction with average global vibration reduction of

the order of 15-20 dB for single frequency with one secondary actuator. Also, a single secondary actuator was optimized to control multiple frequencies, in some cases up to 3 with 8-10 dB average global vibration reduction for each frequency.

A fully coupled vibro-acoustic finite element model of a larger, more complex and modally denser box type structure was used as a quick evaluation of the potential of MAP to reduce noise in the passenger cabin due to the main rotor transmission excitation. It was shown that MAP control resulted in 6.1 dB reduction in the total kinetic energy of the structure while the averaged sound pressure levels (SPL) in the acoustic cavity dropped by 13.8 dB at resonant excitation. This preliminary analysis clearly shows the potential of MAP in reducing interior noise in a helicopter cabin.

Chapter 2

Introduction

The objective of the proposed work is to demonstrate active vibration reduction for interior noise reduction through the development of a control methodology that is simpler to implement, more robust and reliable for on-board embedment, and requires less and/or low cost hardware. The focus is on demonstrating significant vibration reduction for mid-frequency (500 - 2000 Hz) cabin noise resulting from the gear-box transmission of structure-borne excitation into helicopter interiors. Active vibration/noise control for multiple tone structural noise reduction conventionally employs a sensor array for monitoring the vibratory or acoustic response, a controller with a computationally expensive algorithm, and multiple excitation actuators. In many cases, applications of active control are hampered by the added system complexity, reduced reliability and weight penalty, especially for rotorcraft applications where weight restrictions and reliability are stringent. The proposed active vibration and noise technology using minimum actuation power can significantly reduce the control hardware requirement and greatly simplifies the control algorithm by using a simple and unified objective control function and actuation self-sensing.

2.1 Motivation

Interior noise is an increasingly important discriminator in the commercial helicopter market, with acceptable noise levels traditionally being achieved passively, albeit with substantial weight penalties. Increasing performance demands (i.e., longer range, higher payloads) have driven the pursuit of lighter-weight and higher-performance solutions, often compromising the acoustic comfort inside the cabin. The main sources of high interior noise levels in a helicopter are the main rotor, tail rotor, and main gearbox. The main and tail rotors generate low frequency airborne noise, while the main gearbox generates mostly structure-borne noise from 500 - 2000 Hz, see Fig. 2.1. This mid-frequency range is the focus of the proposed research.

The main gearbox dynamic excitations, generated by meshing gear pairs, are a significant source of vibration and cabin noise in a helicopter. The gearbox excitations are transmitted through to the fuselage via rigid connections that do not appreciably attenuate vibratory energy. These mid to high frequency vibrations typically include discrete gear-meshing frequencies that excite the frames and skins of the helicopter. Subsequently, the frame and skins of the fuselage transmit the vibrations produced by the main gearbox and radiate sound into the cabin interior. Figure 2.2 illustrates the key components of helicopter interior noise sources, propagation paths, and radiation to the interior. Over the past several years, stiffer and lighter weight composite structures have been replacing helicopter structures previously constructed from metal. Specifically, the aircraft skin which was traditionally aluminum has been replaced by composite sandwich panels which have a high Young's Modulus and high flexural wave speeds that cause the panels to be efficient sound radiators in the frequency range of the main gearbox as shown in Fig. 2.3. For such composite panels, typical constrained layer damping passive noise treatment are not effective, necessitating either a different panel structure or an active control system to reduce the radiated noise.

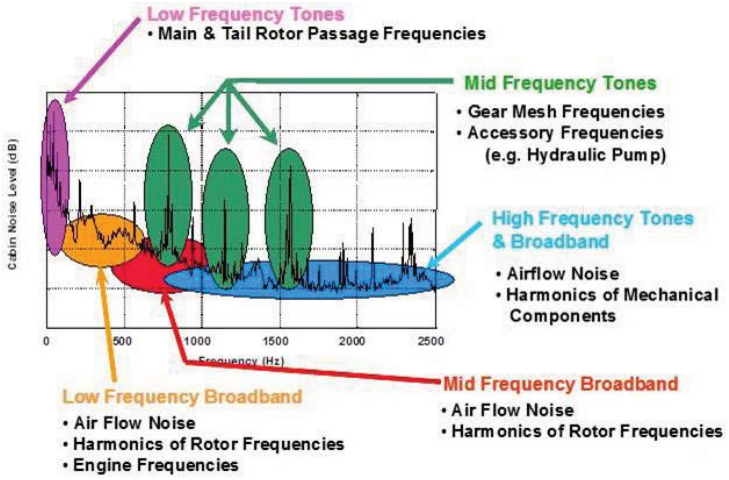

Figure 2.1: Helicopter interior noise profile.

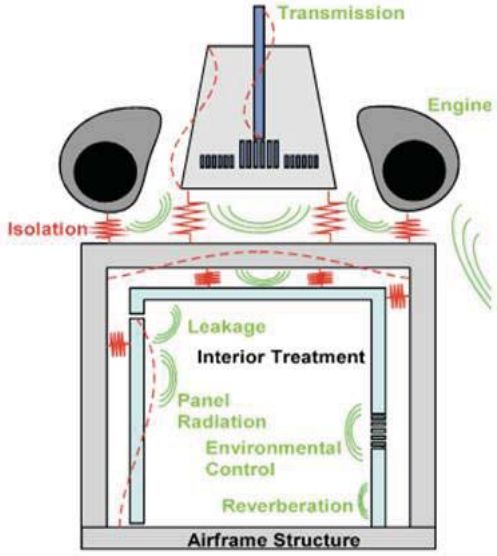

Figure 2.2: Key helicopter interior noise sources, components, and structures.

2.2 Background

Controlling vibration propagation in the airframe is assumed to lead to improvements in passenger comfort and a better environment for on-board electronics. Active Control of

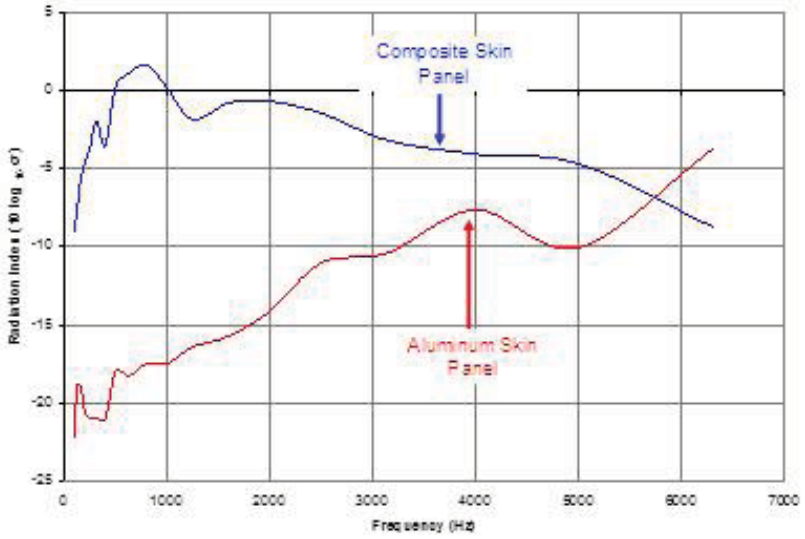

Figure 2.3: Measured radiation index for aircraft skin panels.

Structural Response (ACSR) is a technology developed by Westland Helicopters Ltd., and places its actuation between two hard-points in the fuselage to produce equal and opposite forces between these two hard points. The ACSR approach utilizes these dual-point actuators to minimize the response of the fuselage to the non-propulsion vibratory loads. With a strut-mounted gearbox, and by adding magnetostrictive actuators, Sutton et al. reduced the transmitted kinetic energy to the fuselage of up to 40 dB at frequencies below 1250 [1]. Recently, this control of energy transmission through the strut was revisited with an active and periodic strut design [2] or refined control algorithms [3]. Unlike the Westland helicopters EH101, Sikorsky helicopters, such as the S-92A and UH-60, have the main gearbox bolted directly to the airframe instead of using struts. As a consequence, Sikorsky has developed an Active Vibration Control (AVC) architecture that involves the use of multiple airframe-mounted force actuators to provide canceling vibration, an approach that was successfully demonstrated in-flight on a Sikorsky UH-60L aircraft to cancel 4P vibration [4]. Accelerometers mounted in the cockpit and cabin provided feedback to a controller to determine the actuator commands required to minimize vibration. A schematic of the configuration is presented in Fig. 2.4. A similar AVC system is included as a baseline on all S-92A aircraft [5] and was selected for incorporation into the Army UH-60M, the Navy MH-60R and MH-60S

aircrafts [6, 7]. Finally, AVC is currently being incorporated into the S-76D helicopter and is also one of the enabling technologies for the Sikorsky X2 Technology Demonstrator.

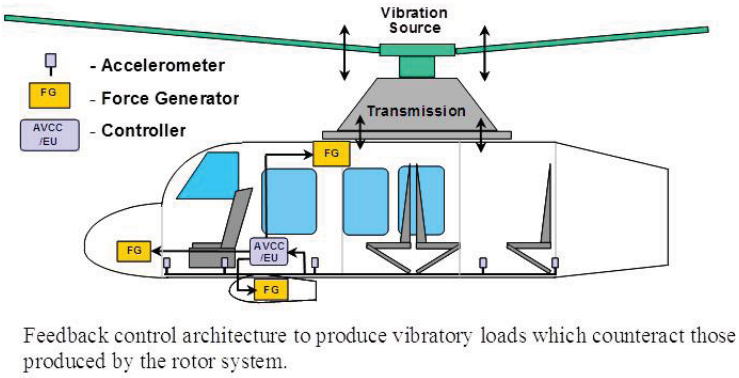

Figure 2.4: Schematic of the AVC architecture developed by Sikorsky.

Active Noise Control (ANC) is an adequate technology to reduce noise in the low- to mid-frequency range [8, 9, 10]. Using this approach in aircraft, many studies reported significant noise reduction, with most of the difference in performance coming from the differences in implementation and control algorithms [11, 12, 13, 14, 15]. Sikorsky Aircraft and the United Technologies Research Center have also been actively engaged in the development and testing of active noise control and active vibration control systems for a number of decades. In the early 1990s, Sikorsky embarked on a multi-year IR & D program to develop a flight-worthy ANC system to actively cancel gear-mesh noise inside the cabin interior. The classical ANC application with speakers as actuators proved inadequate for a typical helicopter cabin due to the high frequencies (> 700Hz) and corresponding large number of participating acoustic modes that would require that the number of speakers be at least equal to the number of relevant acoustic modes. The number of acoustic modes as a function of frequency for a cabin the size of S-76 helicopter is shown in Fig. 2.5

Sikorsky instead pursued the more practical approach of using a pseudo choke-point methodology to prevent the structure-borne gear-mesh vibratory energy from entering the cabin [16]. A schematic of this approach is presented in Fig. 2.6 and involved placing small resonant proof-mass actuators where the main transmission mounts to the airframe, and using micro-

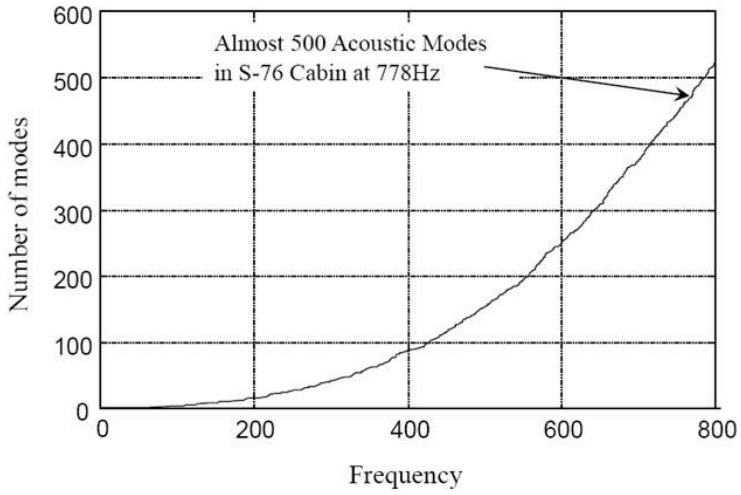

Figure 2.5: Number of acoustic modes for a 5 ft x 6 ft x 9 ft enclosure.

phones inside the cabin as error sensors. Two ANC flight tests were conducted on a Sikorsky S-76B commercial helicopter [17], the first of which is the first known successful flight test of a high frequency gear-mesh ANC system on a helicopter. The development flight tests demonstrated the capability of the gear-mesh ANC system to achieve tonal noise reductions of 18 dB on average and peak reduction by about 23 dB. Based on the success of these flight tests, a follow-on project was conducted to install a production-ready ANC system on a production S-76B helicopter with a VIP Cocoon Interior. The production demonstration flight test was successful in providing significant reductions in the primary gear-mesh tones.

Finally, if the vibration propagation cannot be controlled efficiently or sufficiently, an alternative strategy is to prevent the panels and skin from radiating noise inside the helicopter cabin. Active Structural Acoustic Control (ASAC) [18, 19] alters the noise radiation of the structure through the modification of the vibration pattern. Fuller et. al. [20] mounted piezoceramic actuators directly to an aircraft frame and with only two error microphones inside achieved a noise reduction of over 10dB inside the aircraft fuselage. However, it was shown that the radiated sound could be controlled without having error sensors in the acoustic field, having instead error sensors directly on the structure and a radiation model [21, 22]. As an implementation, the velocity feedback architecture was shown to introduce

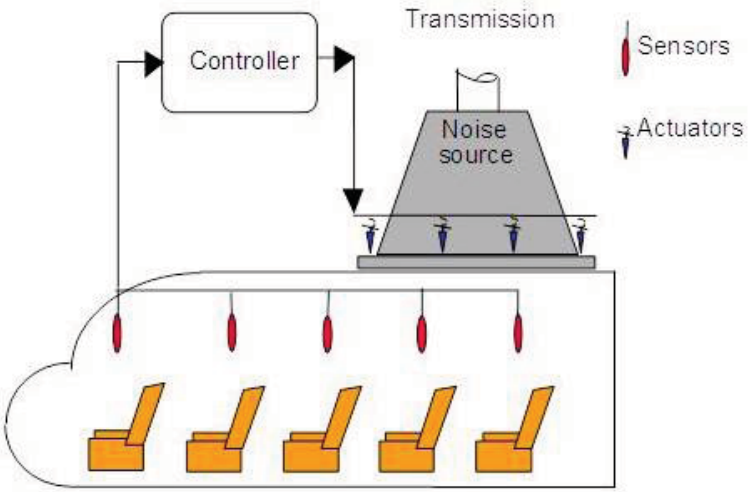

Figure 2.6: Schematic of the Sikosrsky ANC architecture for helicopter interior noise reduction.

active damping by feeding the output of the sensor directly back to the piezoceramic patch actuator via a fixed gain [23]. Furthermore, when the sensor and actuator are collocated, the system is stable. This velocity feedback architecture allows for a decentralized configuration, and actuators of various shapes were successfully tested [23, 24].

With passive noise treatments being too bulky or ineffective to control noise radiation from composite panels, active control of vibration and noise is a viable and attractive alternative. Until now, commercial deployment of active control in rotorcraft has been limited due to high costs, stability issues and overall system complexity. The proposed active control approach, to be described in sections to follow, addresses and avoids these limitations.

2.3 Program goals

The objective of this work is to develop and demonstrate an approach for active vibration reduction on a rotorcraft structure that will ultimately reduce noise in the passenger cabin of the rotorcraft. The active control approach to be developed and demonstrated in this work is based on the concept of actuation power minimization. This is a decentralized control concept, meaning all sensing, control input calculation, and actuation is done local to a specific actuator attached to the structure. This local control approach reduces the need for extensive wiring to connect distributed actuators and sensors and eliminates the need for a centralized control processing unit that coordinates the efforts of many actuators. Although the simplicity of a decentralized control approach is desirable, the approach is not without challenges. These include ensuring that locally optimized control inputs produce a net reduction in a relevant global performance metric, such as sound power in the passenger cabin. A second challenge is to keep the actuator force requirements within realizable limits at the frequencies of interest.

The three-year program is aimed at achieving the following specific overall objectives:

1. Establish a fundamental understanding and expertise of the minimal power control methodology and demonstrate feasibility on a proof-of-concept test in Year 1.
2. Develop modeling capability and a real time control algorithm and demonstrate the technology's effectiveness and ease of implementation on a rotorcraft interior panel structure in Year 2.
3. Demonstrate a technical path toward applying the methodology to the gear meshing noise of rotorcraft main rotor gear box and analytically prove the effectiveness in Year 3.

Specific year-wise goals as stated in the contract Statement of Work (SOW) are:

Phase 1 Theoretical Development and Proof-of-Concept Demonstration

1.1 Develop the theory of minimal actuation power (MAP) vibration control of a single mechanical excitation (the primary excitation) of a structure using a single control actuator (the secondary actuator).
1.2 Develop electromechanical models of the coupling between reactive secondary actuators and a host structure.
1.3 Develop a real-time control algorithm to implement MAP for a single secondary actuator within the frequency range of 500-2000 Hz.
1.4 Experimentally demonstrate MAP for a single primary excitation and single secondary actuator on a simple structure at multiple frequencies.
1.5 Present theoretical and experimental studies of single excitation/single control MAP to quantify control performance using metrics that include, but not be limited to, the reduction of a response variable, the secondary actuator force requirements, and the total input power from the primary and secondary excitations.

Phase 2 Minimal Power Control for Multiple Actuators and Multiple Excitations

2.1 Develop a model of MAP control for multiple primary excitations and multiple secondary actuators. This shall include consideration of system performance as a function of the phasing between primary excitations at a given frequency.
2.2 Develop models of the electromechanical coupling of multiple reactive actuator/sensors to a host structure.
2.3 Develop system simulation models of the MAP control approach with multiple reactive actuators to enable design and optimization of a multiple-actuator MAP control system.
2.4 Experimentally demonstrate MAP vibration control on a rotorcraft interior panel structure with multiple primary excitations and multiple secondary actuators.

Phase 3 Feasibility Assessment of Applying MAP for Vibration Reduction of Airframe Structure

3.1 Assess the feasibility of the MAP control approach for reducing airframe vibrations due to the rotorcraft main rotor transmission and the reduction of corresponding sound levels in the passenger cabin. This assessment shall include, but not be limited to, estimates of system performance versus secondary actuator force and location within the frequency range of 500-2000 Hz.
3.2 Develop a power model of a generic reactive actuator for rigid body excitation.
3.3 Experimentally demonstrate MAP control for vibration reduction on a mock-up of a rotorcraft airframe subject to simulated main rotor transmission excitation.
3.4 Document the technical path to apply MAP control to reduce noise in the passenger cabin due to the main rotor transmission excitation.

2.4 Proposed Active Vibration Control Approach

Our active vibration control approach aims at reducing the interior noise through active vibration control of the helicopter's fuselage and interior structure over the vibration frequencies that are efficient sound radiators. A unique and unconventional concept to perform the structural active vibration and noise control features the following principal characteristics:

- Formulating AVC process as an optimal control strategy that minimizes the total input power into the structure from all the sources of excitation that includes both the primary and secondary sources.
- Minimizing the total input power using the input power in the secondary sources only without any knowledge of the primary sources.
- Eliminating the need for error sensor by using the reactive nature of actuator for self-sensing of vibratory response.

MAP active vibration control has the following advantages:

- *Simple implementation.* A single scalar quantity, the real power in the secondary source, is used to minimize the total input power.
- *Global vibration reduction.* The total input power is an indicator of the global vibration level.
- *Reduced hardware.* Since sensing and actuation is done at the secondary sources, the approach does not need additional sensors.
- *Unconditionally stable.*

A comparison with a conventional configuration is shown in Fig. 2.7. It is envisioned that implementation into a helicopter interior would potentially consistent of active vibration sensing and control on skins and or frames resulting in lowered measured interior noise levels, see illustration in Fig. 2.8. Note that the architecture in Fig. 2.8 tries to reduce interior noise levels by directly attenuating the panel vibration whereas the architecture in Fig. 2.6 reduces interior noise by sensing the interior noise using an array of micro-phones and using that information to suppress the vibration at the source locations.

2.5 Report Outline

In §3, we develop the theory of MAP for a structure excited by a single primary excitation and controlled by a single secondary excitation. We develop an electro-mechanical model of a simply supported plate excited by a single primary PZT actuator and controlled by a single secondary PZT actuator, then extend MAP theory for multi-frequency excitation. Simulation and experimental results are presented to validate the theoretical findings at resonance and off-resonance conditions.

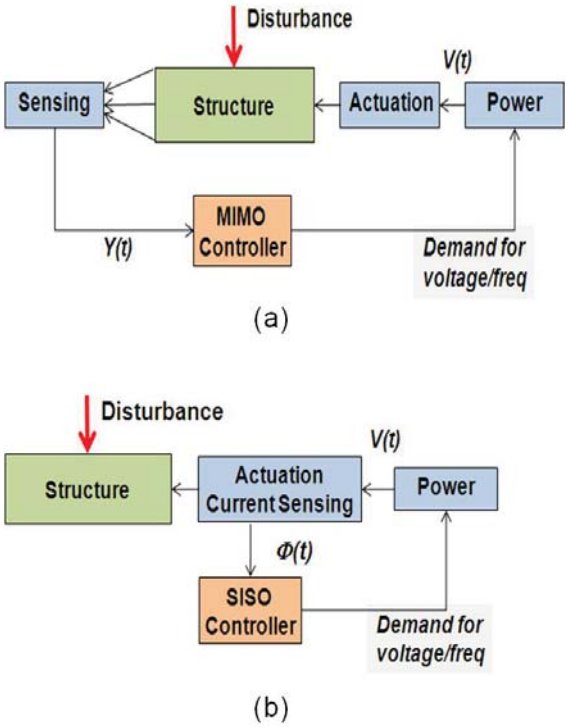

Figure 2.7: Comparison between (a) Conventional feedback control and (b) proposed MAP control.

In §4, we extend the theory of MAP for a structure excited by a multiple primary excitation and controlled by multiple secondary excitations. We develop an electro-mechanical model of a simply supported plate excited by multiple primary and secondary PZT actuators. The effect of relative phasing between the primary sources on MAP condition is analyzed and the performance of MAP control as a function of the number and location of the secondary actuators is studied. Simulation and experimental results are presented to validate the theoretical findings at resonance and off-resonance conditions.

In §5, we assess feasibility of MAP control for rotorcraft vibration reduction with realistic excitation. Specifically, we look at feasibility of MAP for multiple primary sources with arbitrary relative phasing controlled by multiple secondary sources. A test-rig that mimics

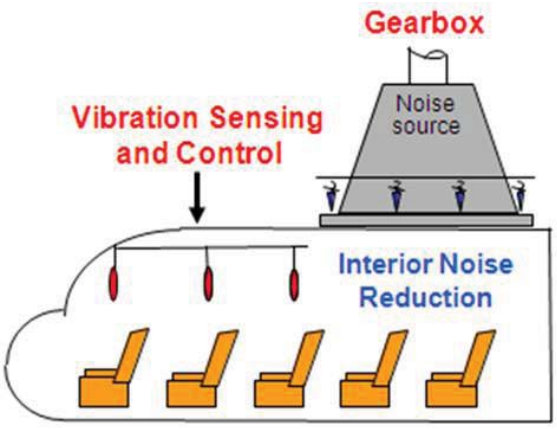

Figure 2.8: Schematic of the potential architecture for gear-mesh structural AVC for interior noise reduction.

rotorcraft construction was designed, modeled and built. Experimental results are presented that validate MAP control with multi-frequency shaker excitation and controlled by multiple secondary actuators for resonance and off-resonance excitations.

In §6, we present a FEM analysis on a simple box type interior structure and demonstrate the potential of MAP in reducing the interior noise by reducing the structural vibration.

In §7, we summarize the key accomplishments and provide next steps.

Chapter 3

MAP Control for Single Primary and Single Secondary

In this chapter, we develop the theory of MAP for a structure excited by a single primary source and controlled by a single secondary source. In §3.1, we review the relevant literature in the areas of structural vibration control using power minimization. In §3.2, we discuss the general theory of input power minimization and present the key idea behind MAP. A model of simply supported plate excited by a primary PZT actuator and controlled by a secondary PZT actuator is developed. The MAP theory is developed for multi-frequency excitation and a special case of commensurate frequencies is considered. Simulations results are presented in §3.3 to validate the theoretical findings. The performance of MAP control is evaluated at resonant and off-resonant frequencies. In §3.4, a simple relation between the net electrical power in the secondary actuator and the net input (mechanical) power is derived that enables implementing MAP by monitoring the net electrical power. Experimental results are presented in §3.5

3.1 Literature Review

This section summarizes the published works specific to our proposed goals of implementing MAP control strategy and using piezoelectric actuators for vibration control of a panel structure.

The concept of power minimization for the sound radiation of multiple acoustic monopoles was presented by Nelson et al. [25] and it was found that in many instances, there exists a unique set of secondary sources of complex source strengths that minimizes the overall acoustic power in the system. Elliott et al. [26] further developed the methodology by introducing two control strategies, i.e. the minimization of total input power by primary and secondary actuators and the maximization of secondary actuator power absorption. For the case of single primary and single secondary acoustic sources, Johnson and Elliott [27] demonstrated that the real power of a secondary source was zero when optimally controlling a primary source in an enclosed field. In addition, these authors noted when the two sources were close to each other, greater global sound reduction could be achieved. As will be shown, the proposed MAP approach follows the same reasoning and expends on it and applies it to vibration control.

Bardou et al. [28] applied a similar strategy of considering the total power that enters a structure to control the flexural vibration of plates. Bardou et al. showed that minimizing the total power in the plate yields greater overall power attenuation than what results from maximizing the secondary power absorption, for both an infinite and finite plate. Furthermore, the greatest attenuation was achieved if the secondary sources were relatively close to the primary source, i.e. when the two excitation sources are close with respect to the wavelength of the flexural wave, and in the case of infinite plate, the primary and secondary sources cannot be too distant if global control is to be achieved. Benassi and Elliott [29] also noted the effect of distance on global control, and used idealized passive treatments with specified impedances as secondary reactive sources to attenuate the vibratory energy in a plate structure.

Another major task in MAP development, the methodology of actuator/sensor interaction with the vibrating host structure and its power consumption has been broadly reviewed

and analyzed. Although an electromagnetic actuator, which is of reactive nature, is capable of performing the collocated sensing and actuation in principle, its low sensitivity, large weight and implementation issues disqualify it as the first choice for the MAP demonstration. The piezoelectric actuator, on the other hand, is considered the most promising device for demonstrating the principle of the MAP AVC because of its intimately close coupling to the structure and its distributed and non-invasive actuation.

A lot of work on piezoelectric power consumption has been reported since the first publication of the piezoelectric collocated sensor actuator by Dosch [30]. Early research of piezoelectric power consumption as actuator consists of two distinct approaches described in Liang et al[31, 32], Zhou et al [33] and Hagood et al [34]. These approaches examined the power consumption of actuators when used to excite the host structure and did not consider the case of active control. Liang developed an equation of the one-dimensional piezoelectric actuator. The response of the actuator was determined by prescribing boundary conditions to the actuator that coupled it with the host structure. The resulting explicit solution of the coupled electromechanical impedance has been widely used for structural health monitoring and actuation efficiency optimization in modal control and modal analysis. The other modeling approach developed by Hagood et al, established a relation of piezoelectric actuator mechanical outputs with the electric voltage and current inputs to the actuator. Both models are proven to be accurate. Another comprehensive study by Warkentin [35] presented a development of piezoelectric power consumption for active vibration control using the analytical models developed by Hagood et al. The conclusions in these papers are that the electrical power of piezoelectric actuators is dependent on the mechanical motion of the structure and the electrical characteristics of the piezoelectric material and geometry. More recent work on the actuator power modeling includes [36, 37, 38]. Brennan et al. [36] developed an ANC model that shows that electric power of a piezoelectric actuator in active vibration control is independent of the mechanical motion of the host structure when the structure is under optimal control. While the work was intended to define the electric power requirement for the amplifier, the conclusion has significant physical implications relative to MAP for AVC. Namely, when complete control is reached, the structure is motionless, therefore the power consumption of the piezoelectric actuator is no longer a function of the mechanical motion but a function of the geometry, material properties of actuators, and the voltage and frequency of the control signal (power baseline). This principle sets the stage for the electric MAP baseline control which simply seeks a blocked boundary condition to

the actuator without the need for knowledge of the primary excitation. The current development will build upon that work and bridge the gap between the global vibration reduction and minimal electric power (baseline). The spatial optimization of the actuators for modal control is another important aspect to consider[39, 40].

3.2 Theory of Minimum Actuation Power (MAP)

In this section, we develop the theory of minimum actuation power. In §3.2.1, we develop the theory of MAP by considering a general structure that is excited by a set of primary sources and controlled by a set of secondary sources. We consider point forces for sake of illustration. However, the sources can be either forces or moments or a combination of both. We derive the optimal secondary sources that minimize the total power input into the structure. For the case with one primary source and one secondary source, we show that at optimal condition the real power in the secondary source is exactly zero. In §3.2.2, we extend the theory of MAP for a simply supported plate excited by a primary PZT patch and controlled by a secondary PZT patch.

3.2.1 Input power minimization

Conside a two-dimensional structure (e.g., simply supported plate) that is excited by N normal point forces

$$\boldsymbol{f}^T(t) = [f_1 \quad f_2 \quad \dots \quad f_N] \tag{3.1}$$

and let

$$\boldsymbol{v}^T(t) = [v_1 \quad v_2 \quad \dots \quad v_N] \tag{3.2}$$

be the the velocity vector consisting of the set of normal velocities at the point of application of the forces. The time averaged total input power due to all the forces is given as[1]

$$\bar{P} = \frac{1}{2}\mathrm{Re}\{\boldsymbol{F}^H \boldsymbol{V}\} \tag{3.3}$$

where $\boldsymbol{F}$ and $\boldsymbol{V}$ represent the complex amplitudes of $\boldsymbol{f}$ and $\boldsymbol{v}$. The total input power can be expressed as

$$\bar{P} = \frac{1}{2}\mathrm{Re}\{\boldsymbol{F}^H \boldsymbol{M}\boldsymbol{F}\} \tag{3.4}$$

where $\boldsymbol{M}$ is the mobility matrix. Using reciprocity, $\boldsymbol{M}$ is symmetric. In this case

$$\bar{P} = \frac{1}{2}\boldsymbol{F}^H \mathrm{Re}\{\boldsymbol{M}\}\boldsymbol{F} = \frac{1}{2}\boldsymbol{F}^H \boldsymbol{R}\boldsymbol{F} \tag{3.5}$$

where $\boldsymbol{R}$ is the real part of $\boldsymbol{M}$. If the force vector consists of primary and secondary sources

$$\boldsymbol{F}^T = \{\boldsymbol{F}_p^T \boldsymbol{F}_s^T\} \tag{3.6}$$

then $\boldsymbol{R}$ can be decomposed as

$$\boldsymbol{R} = \begin{bmatrix} \boldsymbol{R}_{pp} & \boldsymbol{R}_{ps} \\ \boldsymbol{R}_{sp} & \boldsymbol{R}_{ss} \end{bmatrix} \tag{3.7}$$

where $\boldsymbol{R}_{sp} = \boldsymbol{R}_{ps}^T$ Using (4.7) and (3.7), we can express the total input power as

$$\bar{P} = \frac{1}{2}[\boldsymbol{F}_p^H \boldsymbol{R}_{pp}\boldsymbol{F}_p + \boldsymbol{F}_p^H \boldsymbol{R}_{ps}\boldsymbol{F}_s + \boldsymbol{F}_s^H \boldsymbol{R}_{sp}\boldsymbol{F}_p + \boldsymbol{F}_s^H \boldsymbol{R}_{ss}\boldsymbol{F}_s] \tag{3.8}$$

Note that $\bar{P}$ is a quadratic function of $\boldsymbol{F}_s$. Minimizing $\bar{P}$ with respect to $\boldsymbol{F}_s$, we get [41]

$$\boldsymbol{F}_s^{opt} = -\boldsymbol{R}_{ss}^{-1}\boldsymbol{R}_{sp}\boldsymbol{F}_p \tag{3.9}$$

[1]The averaged product of two sinusoidally varying quantities represented in complex form reduces to the real part of the product of their complex amplitudes

$$\overline{u_1(t)u_2(t)} = \frac{1}{2}\mathrm{Re}\{U_1 U_2^*\}$$

Key idea for MAP control

Let us consider the case where there is one primary and one secondary source. In this case, the optimal secondary source is given by

$$F_s^{opt} = -\frac{R_{sp}}{R_{ss}} F_p \tag{3.10}$$

The real power in the secondary source is given by

$$\bar{P}_s = \frac{1}{2}\mathrm{Re}\{F_s^* M_{sp} F_p + F_s^* M_{ss} F_s\} \tag{3.11}$$

Using (3.10), the real power in the secondary source at optimal value is

$$\begin{aligned} \bar{P}_s^{opt} &= \frac{1}{2}\mathrm{Re}\{-\frac{R_{sp}}{R_{ss}} F_p^* M_{sp} F_p + \frac{R_{sp}^2}{R_{ss}^2} F_p^* M_{ss} F_p\} \\ &= \frac{1}{2}(-\frac{R_{sp}}{R_{ss}} F_p^* R_{sp} F_p + \frac{R_{sp}^2}{R_{ss}^2} F_p^* R_{ss} F_p\} \\ &= 0 \end{aligned} \tag{3.12}$$

We make the following important observation:

For one primary force controlled by one secondary force, the real power $\bar{P}_s$ in the secondary source is zero when $F_s = F_s^{opt}$ where F_s^{opt} is the optimal value that minimizes the total input power $\bar{P}$

This suggests a way to control the structure by only tuning the power in the secondary actuator without explicit knowledge about the primary source. The control strategy is to drive the real power in the secondary actuator to zero. This is the underlying principle of MAP control.

3.2.2 MAP theory for a simply supported plate actuated by two piezoelectric patches

We investigate active control of the transverse vibrations of a simply supported plate using the Minimum Actuation Power (MAP) technique. The plate is excited by a primary PZT patch actuator and controlled by a secondary PZT patch actuator. Analytical expressions for the total input power due to the primary and secondary patches in terms of the equivalent patch angular mobilities are presented. The optimal value of the secondary moment that minimizes the total input power is computed. We show that at optimal value of the secondary moment, the total input power due the secondary actuator is zero. This key observation is the basis of MAP control.

System description

Consider a simply supported rectangular plate that is actuated by two identical PZT patch actuators as shown in Fig 4.1(a). Each actuator is driven by a voltage source. The primary patch acts as the disturbance while the secondary patch is the control actuator. Let L_x, L_y and H be the length, width and thickness of the plate respectively. The plate is assumed to be isotropic. The PZT patches are bonded to the plate surface and are assumed to be square with width a and thickness h. When an electric field is applied to the patch in the z direction, the patch expands and contracts in both the x and y directions. The resulting strain field generates a distributed moment along the edges of the patch, labeled 1 to 4, as shown in Fig 4.1(b). We assume that the patch is isotropic. Also, the patch is assumed to be thin and the patch inertia and stiffness are ignored in the analysis.

Total input power from primary and secondary actuators

Let $\bar{M}_p$ and $\bar{M}_s$ be the moments per unit length (complex amplitude) generated by the primary and secondary patch respectively. Let the primary and secondary patch edges be

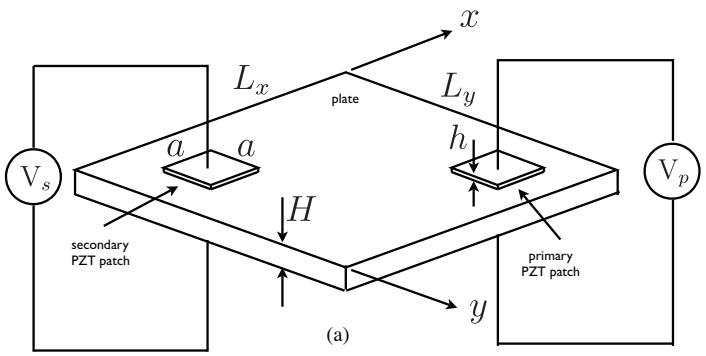

Figure 3.1: (a) Schematic of a simply supported rectangular plate excited by two PZT actuators (b) Distributed moment generated by a patch.

discretized into an equal number of elements and let Δe be the length of the edge element. Then, the primary and secondary moments generated by each element are

$$\begin{aligned} M_p &= \Delta e\, \bar{M}_p \\ M_s &= \Delta e\, \bar{M}_s \end{aligned} \tag{3.13}$$

The total power input from the primary and secondary patches can be written as

$$\bar{P} = \bar{P}_p + \bar{P}_s \tag{3.14}$$

where $\bar{P}_p$ and $\bar{P}_s$ are the total power inputs from the primary and secondary patches respectively.

Let us assume that the primary and secondary patch edges are discretized into an equal number of elements, say q. Let p_i and s_i represent the coordinates of the center of the i^{th}

primary and secondary patch element respectively where $i = 1, \ldots, q$. Let M_p and M_s be the primary and secondary moments acting on each element respectively. Consider the point p_i on the primary patch. The angular velocity at this point is a sum of the angular velocity induced by the primary and secondary patch moments and can be expressed as

$$W_{p_i} = \sum_j W_{p_i p_j} + \sum_j W_{p_i s_j} \tag{3.15}$$

where $W_{p_i p_j}$ is the angular velocity induced at p_i due to the moment M_p at location p_j and $W_{p_i s_j}$ is the angular velocity induced at p_i due to the moment M_s at location s_j. The angular velocities $W_{p_i p_j}$ and $W_{p_i p_j}$ can be expressed as

$$\begin{aligned} W_{p_i p_j} &= P_{p_i p_j} M_p \\ W_{p_i s_j} &= P_{p_i s_j} M_s \end{aligned} \tag{3.16}$$

where $P_{p_i p_j}$ and $P_{p_i s_j}$ are the cross mobility terms given by [28]

$$\begin{aligned} P_{p_i p_j} &= \sum_{n=1}^{\infty} \left(\eta\omega\omega_n^2 + j\omega(\omega_n^2 - \omega^2)\right) \frac{4\,\psi_n^{\delta_{p_i}}(p_i)\,\psi_n^{\delta_{p_j}}(p_j)}{m\left[(\omega_n^2 - \omega^2)^2 + \omega_n^4\eta^2\right]} \\ P_{p_i s_j} &= \sum_{n=1}^{\infty} \left(\eta\omega\omega_n^2 + j\omega(\omega_n^2 - \omega^2)\right) \frac{4\,\psi_n^{\delta_{p_i}}(p_i)\,\psi_n^{\delta_{s_j}}(s_j)}{m\left[(\omega_n^2 - \omega^2)^2 + \omega_n^4\eta^2\right]} \end{aligned} \tag{3.17}$$

where η is the structural damping, m is the plate mass, ω is the excitation frequency (assumed same for primary and secondary excitation) and ω_n is the n^{th} resonant frequency given by

$$\omega_n = \sqrt{\frac{EH^2}{12(1-\mu^2)\rho}} \left(\left(\frac{n_1\pi}{L_x}\right)^2 + \left(\frac{n_2\pi}{L_y}\right)^2 \right) \tag{3.18}$$

where n refers to the mode index (n_1, n_2), E is the modulus of elasticity, μ is the Poison ratio and ρ be the density of the plate material. The function $\psi_n^{\delta_p}(p)$ is given by

$$\psi_n^{\delta_p}(p) = \frac{n_1\pi}{L_x}\cos(\delta_p)\cos\left(\frac{n_1\pi x_p}{L_x}\right)\sin\left(\frac{n_2\pi y_p}{L_y}\right) + \frac{n_2\pi}{L_y}\sin(\delta_p)\sin\left(\frac{n_1\pi x_p}{L_x}\right)\cos\left(\frac{n_2\pi y_p}{L_y}\right) \tag{3.19}$$

where (x, y) are the coordinates of the point p and δ_p is the angle made by the moment axis with the x axis. Note that for the primary (or secondary) patch, $\delta_{p_i}(\text{or}\,\delta_{s_i}) = 0$, $\pi/2$, π and $3\pi/2$ for all elements i along edges 1, 2, 3 and 4 respectively. The total power input due to the primary patch is given by

$$\bar{P}_p = \frac{1}{2}\text{Re}\left(M_p^* \sum_i W_{p_i}\right) \tag{3.20}$$

Using (A.1) and (A.2) in (A.6), the total input power due to the primary patch can be expressed as

$$\bar{P}_p = \frac{1}{2}\text{Re}\left(M_p^* P_{pp} M_p + M_p^* P_{ps} M_s\right) \tag{3.21}$$

where P_{pp} represents the equivalent angular mobility due to the primary patch given by

$$P_{pp} = \sum_i \sum_j P_{p_i p_j} \tag{3.22}$$

and P_{ps} represent the cross angular mobility given by

$$P_{ps} = \sum_i \sum_j P_{p_i s_j} \tag{3.23}$$

Similarly, the total power input due to the secondary patch can be shown to be

$$\bar{P}_s = \frac{1}{2}\text{Re}\left(M_s^* P_{sp} M_p + M_s^* P_{ss} M_s\right) \tag{3.24}$$

where $P_{sp} = P_{ps}$ represents the cross angular mobility and

$$P_{ss} = \sum_i \sum_j P_{s_i s_j} \tag{3.25}$$

represents the equivalent angular mobility due to the secondary patch. It can be shown that

$$\bar{P}_p = \frac{1}{2}\text{Re}\left(M_p^* P_{pp} M_p + M_p^* P_{ps} M_s\right) \tag{3.26}$$

$$\bar{P}_s = \frac{1}{2}\text{Re}\left(M_s^* P_{sp} M_p + M_s^* P_{ss} M_s\right) \tag{3.27}$$

where P_{pp} and P_{ss} are the equivalent angular mobility terms due to the primary and secondary patch respectively while P_{ps} and P_{sp} are the cross angular mobility terms. By reciprocity, we have $P_{ps} = P_{sp}$. In other words, the total input power of a simply supported plate excited by two PZT patches is equivalent to the total input power of a simply supported plate excited by two point moments M_p and M_s with equivalent point and transfer mobilities P_{pp}, P_{ss}, P_{ps} and P_{sp}. The reader is referred to §B for a detailed derivation of the relations in (3.26) and (3.27). From (4.5), (3.26) and (3.27), the total input power from both the primary and secondary patch is given by

$$\bar{P} = \frac{1}{2}\mathrm{Re}\left(M_p^* P_{pp} M_p + M_p^* P_{ps} M_s + M_s^* P_{sp} M_p + M_s^* P_{ss} M_s\right) \tag{3.28}$$

Using reciprocity of the cross mobility terms, (4.6) can be further simplified as

$$\bar{P} = \frac{1}{2}\left(M_p^* S_{pp} M_p + M_p^* S_{ps} M_s + M_s^* S_{sp} M_p + M_s^* S_{ss} M_s\right) \tag{3.29}$$

where S_{pp}, S_{ps}, S_{sp} and S_{ss} are the real parts of P_{pp}, P_{ps}, P_{sp} and P_{ss} respectively. Note that $S_{ps} = S_{sp}$.

Total input power minimization (MAP) control

We seek to find the optimal secondary excitation that will minimize the net input power $\bar{P}$. Equation (3.29) is a quadratic equation of the secondary moment M_s and therefore a unique minimum exists. Minimizing the total input power $\bar{P}$ with respect to M_s, we get the optimal secondary moment as a function of the primary moment and the angular mobility terms

$$M_s^{opt} = -\frac{S_{sp}}{S_{ss}} M_p \tag{3.30}$$

Since S_{sp} and S_{ss} are real, (3.30) shows that M_s^{opt} is either in phase or out of phase with M_p depending on the sign of $-S_{sp}/S_{ss}$. An important implication of the above observation is that one only needs to vary the amplitude of the secondary moment to search for the optimal value. Equations (3.30) show that in order to compute the optimal secondary moment, we need information about the primary excitation. From an experimental point of view, frequency

of the primary excitation can be easily extracted. However, extracting the magnitude of the primary source is difficult. In that case, we cannot calculate the optimal values M_s^{opt}. In what follows, we show how the net power in the secondary actuator can be used as a control variable to implement MAP control without explicit knowledge about the strength of the primary excitation. Using (3.30) in (3.27), the real power in the secondary source at optimal value is given by

$$\begin{aligned} \bar{P}_s^{opt} &= \frac{1}{2}\mathrm{Re}\left(-\frac{S_{sp}}{S_{ss}}M_p^* P_{sp} M_p + \frac{S_{sp}^2}{S_{ss}^2}M_p^* P_{ss} M_p\right) \\ &= \frac{1}{2}\left(-\frac{S_{sp}}{S_{ss}}M_p^* S_{sp} M_p + \frac{S_{sp}^2}{S_{ss}^2}M_p^* S_{ss} M_p\right) \\ &= 0 \end{aligned} \tag{3.31}$$

Thus, for a plate excited by a primary PZT actuator and controlled by a secondary PZT actuator, the real power $\bar{P}_s$ in the secondary actuator is zero when $M_s = M_s^{opt}$ where M_s^{opt} is the optimal value of the secondary actuator moment that minimizes the total input power $\bar{P}$ from both the primary and secondary actuators. This suggests a way to control the structure by only tuning the power in the secondary actuator without explicit knowledge about the magnitude of the primary source. The control strategy is to drive the real power in the secondary actuator to zero.

3.2.3 MAP control for multifrequency excitation

We show that the theory of MAP derived for single frequency excitation also holds when you have multi-frequency excitation provided the frequencies are commensurate, i.e., integer multiples of a fundamental frequency. In section 3.2.3, we develop the theory of MAP for multi-frequency excitation by considering point forces acting on the structure. Though we consider point forces for sake of illustration, the results hold for distributed moment excitation as generated by a PZT patch. In section 3.3.7, we present simulation results for a simply supported plate excited by a primary PZT actuator and controlled by a secondary PZT actuator where the primary and secondary excitations are multi-frequency.

Let

$$f(t) = \sum_{k=1}^{n} f_k(t) \tag{3.32}$$

be a point force excitation acting on the structure where f_k is the k^{th} component with frequency ω_k. Let us assume that ω_k's are commensurate. Using superposition, the response at the excitation location can be expressed as

$$v(t) = \sum_{k=1}^{n} v_k(t) \tag{3.33}$$

where v_k is the response corresponding to the component f_k of the excitation. The time averaged input power due to the excitation is given by

$$\bar{P} = \overline{f(t)v(t)} = \frac{1}{T}\int_0^T \left(\sum_{k=1}^{n} f_k(t)\right)\left(\sum_{k=1}^{n} v_k(t)\right) dt \tag{3.34}$$

where T is the period. Since the frequencies are commensurate, Parseval's lemma [42] gives

$$\bar{P} = \sum_{k=1}^{n} \frac{1}{T}\int_0^T f_k(t)v_k(t)\, dt = \sum_{k=1}^{n} \bar{P}_k \tag{3.35}$$

where

$$\bar{P}_k = \frac{1}{T}\int_0^T f_k(t)v_k(t)\, dt \tag{3.36}$$

is the time-averaged input power corresponding to ω_k. Equation (3.35) will hold even when the system is excited by a primary and secondary force given by[2]

$$\begin{aligned} f_p(t) &= \sum_{k=1}^{n} f_{pk}(t) \\ f_s(t) &= \sum_{k=1}^{n} f_{sk}(t) \end{aligned} \tag{3.37}$$

[2]In general, (3.35) holds if the structure is excited by a set of primary and secondary forces with similar harmonic components

where f_{pk} and f_{sk} are harmonic with frequency ω_k. Note that in this case, $\bar{P}_k$ denotes the total input power due to f_{pk} and f_{sk}. It follows from (3.35) that

$$\min \bar{P} \equiv \{\min \bar{P}_1, \min \bar{P}_2, \ldots, \min \bar{P}_n\} \tag{3.38}$$

That is, the total input power can be minimized by minimizing the input powers corresponding to each frequency. The optimal value of the secondary force that minimizes the total input power $\bar{P}$ is given by

$$f_s^{opt}(t) = \sum_{k=1}^{n} f_{sk}^{opt}(t). \tag{3.39}$$

where the optimal complex amplitude F_{sk}^{opt} of $f_{sk}^{opt}(t)$ is given by

$$F_{sk}^{opt} = -R_{ss}^{-1}(\omega_k) R_{sp}(\omega_k)\, F_{pk}^{opt} \quad \forall \quad k \tag{3.40}$$

where F_{pk}^{opt} is the complex amplitude of $f_{pk}(t)$. Equation (3.40) follows from the MAP results for single frequency excitation. Thus, the MAP theory can be extended to multi-frequency excitation.

Next, we show that minimization of total input power is equivalent to minimization of the net vibrational energy in the case of multi-frequency excitation. For example, consider a rectangular plate that is excited by primary and secondary forces as given by (3.37). By superposition, the velocity at any point (x, y) on the plate can be expressed as

$$v(x, y, t) = \sum_{k=1}^{n} v_k(x, y, t) \tag{3.41}$$

where $v_k(x, y, t)$ has frequency ω_k and is a contribution of both $f_{pk}(t)$ and $f_{sk}(t)$. The global vibrational energy of the plate is given by

$$E_{kin}(t) = \frac{1}{2}\bar{m} \int_0^{L_x} \int_0^{L_y} v(x, y, t)^2 \, dx \, dy \tag{3.42}$$

where $\bar{m}$ is the mass per unit area. The average vibrational energy is given by

$$\overline{E}_{kin} = \frac{1}{2T}\bar{m} \int_0^{L_x} \int_0^{L_y} \int_0^{T} \left(\sum_{k=1}^{n} v_k(x, y, t) \right) \left(\sum_{k=1}^{n} v_k(x, y, t) \right) dt \, dx \, dy \tag{3.43}$$

Using Parseval's lemma gives

$$\overline{E}_{kin} = \sum_{k=1}^{n} \frac{1}{2T} \bar{m} \int_0^{L_x} \int_0^{L_y} \int_0^{T} v_k(x,y,t)^2 \, dt \, dx \, dy = \sum_{k=1}^{n} \overline{E}_{kin}^k \tag{3.44}$$

where

$$\overline{E}_{kin}^k = \frac{1}{2T} \bar{m} \int_0^{L_x} \int_0^{L_y} \int_0^{T} v_k(x,y,t)^2 \, dt \, dx \, dy \tag{3.45}$$

is the average vibrational energy corresponding to ω_k. Using the theory of MAP for single frequency, we have

$$\min \bar{P}_k \equiv \min \overline{E}_{kin}^k \tag{3.46}$$

Using (3.38), (3.44) and (3.46), we get

$$\min \bar{P} \equiv \min \overline{E}_{kin} \tag{3.47}$$

Equation (3.47) shows that minimizing the average input power is equivalent to minimizing the average vibrational energy even when the excitation is multi-frequency provided that the frequencies are commensurate.

3.3 Simulations

We present simulation results to validate the analytical findings. The effectiveness of the control depends not only on the position of the secondary patch with respect to the mode shapes but also whether the excitation frequency is close to a resonant frequency or away from resonance. We present simulation results that help quantify the control effectiveness as a function of the secondary position and the excitation frequency.

3.3.1 Simulation parameters

A schematic of plate system for simulation studies is shown in Fig. 4.2. Note that (x_p, y_p) and (x_s, y_s) represent the coordinates of the centers of the primary and secondary patch

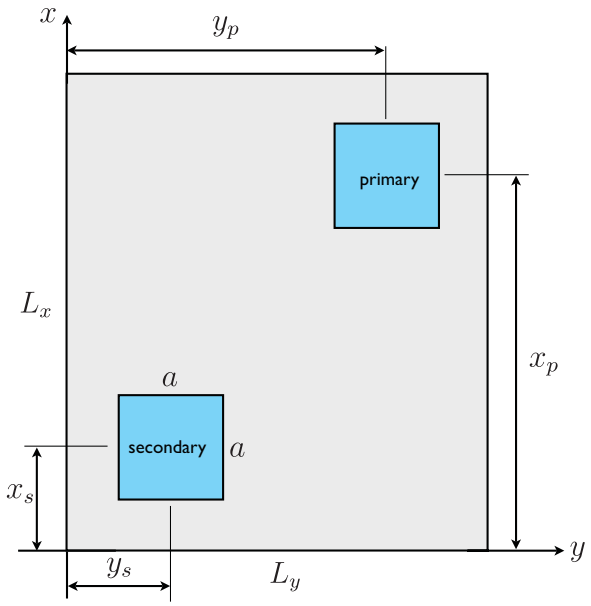

Figure 3.2: Schematic of the plate system for simulation.

respectively. The location of the primary patch is fixed. We assume that the plate is made of aluminum. Table 4.1 lists geometrical and material properties for the plate and PZT patches.

3.3.2 Vibration response under primary excitation

We first study the response of the plate under primary excitation only. The secondary actuator does not apply any control. The coordinates of the center of the primary actuator are $(x_p, y_p) = (0.275, 0.225)$. The frequency range for the excitation frequency is chosen to be 100-2000 Hz. We assume that the voltage applied to the primary actuator is such that it generates a unit moment at each element, that is, $M_p = 1$ Nm. There are 13 resonant frequencies in this frequency range: ω_n(Hz) = 620, 724, 826, 976, 1039, 1222, 1395, 1413, 1474, 1626, 1862, 1893 and 1982. Figure 3.3 shows the average vibrational energy of the

Table 3.1: Simulation Parameters

Variable	Value
L_x	0.38 m
L_y	0.35 m
H	4.2e-3 m
E	70e9 Pa
η	0.01
ρ	2700 kg/m^3
μ	0.33
a	0.05 m
h	0.13e-3 m
Y_{11}	6.6e10 Pa
d_{31}	-190e-12 m/V
$\bar{\varepsilon}_{33}$	1.53e-8 F/m
ν_p	0.35
δ	0.02

plate when the primary excitation is applied. Interestingly, it can be seen from Fig. 3.3 that the resonances at 1395 Hz and 1893 Hz are not excited. This is due to the fact that the location of the primary patch is close to the nodal lines of the mode shapes at 1395 Hz and 1893 Hz. Figure 3.4 shows the modes shapes at 1395 Hz and 1893 Hz. The position of the primary patch is also shown and it can be clearly seen that in both cases, the primary patch is located at the intersection of two nodal lines. Therefore, the primary excitation is not effective in exciting the modes at 1395 Hz and 1893 Hz.

3.3.3 Vibration response with MAP control

The center of the secondary actuator is located at $(x_s, y_s) = (0.075, 0.075)$. Note that this location is not optimized for any frequency range. Figure 3.5 shows the average vibrational energy of the plate with and without MAP control. As seen, the control is most effective close to each resonance (the greatest difference in vibrational energy between control off and

control on). Note that the modes at $\omega_n = 1413$ Hz and $\omega_n = 1862$ Hz are not controlled. This is because the location of the secondary actuator is not optimal for controlling these resonant modes. This is evident from Fig. 3.6 which shows the mode shapes for 1413 Hz and 1862 Hz, and at both resonances the secondary actuator is on the node lines and away from the mode shape peaks.

3.3.4 MAP control at resonant and off-resonant frequencies

The simulations show that the real part of the secondary power is zero when the total input power is minimum at both resonant and off-resonant frequencies. The key difference is that at resonant frequencies, the vibrational energy is also minimum when the total input power is minimum. However, at off-resonant frequencies, the vibrational energy is not truly minimum when the total input power is minimum (see Eq. B.11). A more detailed analysis of the global vibrational energy and its relation to the total power input is presented in § B.

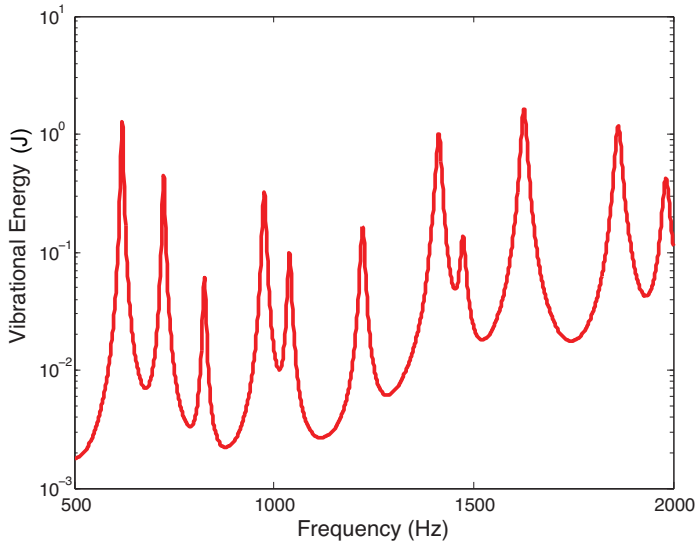

Figure 3.3: Vibrational energy of the plate under unit primary excitation.

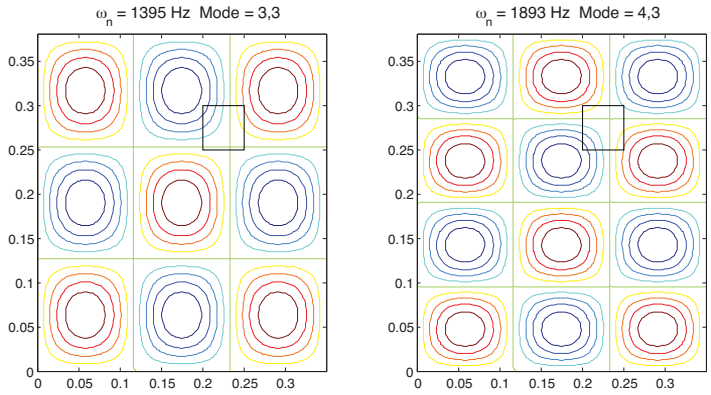

Figure 3.4: Resonance modes for ω_n=1395 Hz and ω_n=1893 Hz. The primary actuator location is shown by the black box.

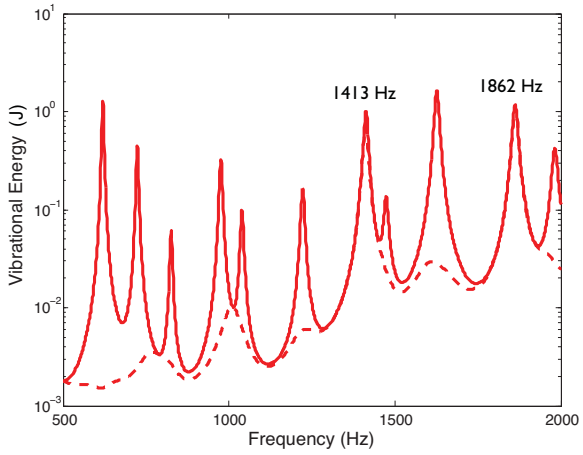

Figure 3.5: Vibrational energy of the plate with MAP control (dashed line) and without MAP control (solid line).

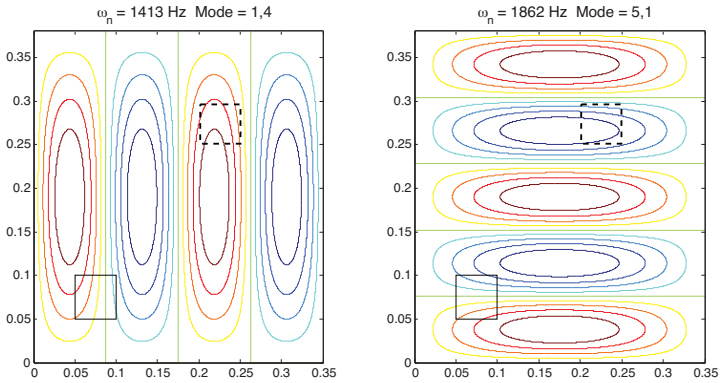

Figure 3.6: Resonance modes for ω_n=1413 Hz and ω_n=1861 Hz. The secondary actuator location is shown by the black box. The primary actuator location is shown by the dashed box.

For the sake of illustration, we focus on two frequency ranges: 550-750 Hz and 1500-1800 Hz. Fig 3.7 shows a zoomed-in view of the vibration response with and without control for the frequency range 550-750 Hz. Two resonant frequencies (620 Hz and 724 Hz) and one off-resonant frequency (680 Hz) were chosen to study the relation between vibrational energy, total input power and real power in secondary actuator. At each frequency, we vary the secondary moment M_s around the optimal value M_s^{opt} by defining

$$M_s = \alpha M_s^{opt} \tag{3.48}$$

where α is a real scalar. Note that $\alpha = 0$ implies zero control and $\alpha = 1$ implies optimal control.

Figures 3.8 and 3.9 show the variation of vibrational energy, total input power and real power in secondary actuator for the resonant frequencies 620 Hz and 724 Hz respectively. As α is varied from zero (no control), the vibrational energy and the total input power (primary plus secondary) decrease till $\alpha = 1$ and then increase. The real secondary power decreases

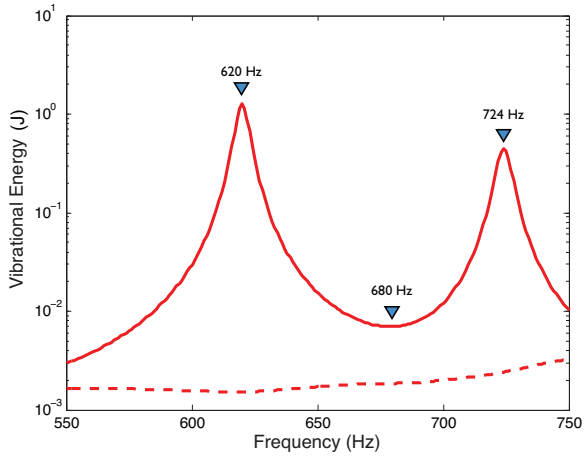

Figure 3.7: Vibrational energy of the plate with MAP control (dashed line) and without MAP control (solid line) for the frequency range 550-750 Hz. Two resonant frequencies (620 Hz and 724 Hz) and one off-resonant frequency (680 Hz) are marked by the blue triangles.

and crosses zero at $\alpha = 1$. In other words, at $\alpha = 1$, both the vibrational energy and the net input power are minimum while the real power in the secondary is zero. On the other hand, Fig. 3.10 shows that when the excitation frequency is away from resonance, the total input power is minimum and the real power in the secondary actuator is zero when $\alpha = 1$ but the vibrational energy is not necessarily minimum at $\alpha = 1$ though it is close to the true minimum.

Similar conclusions can be drawn when we consider the frequency range of 1500-1800 Hz. Figure 3.11 show the vibration response with and without control for the above frequency range. We choose one resonant frequency (1626 Hz) and two off-resonant frequencies (1525 Hz and 1750 Hz) for examining the variation of vibrational energy, total input power and the real secondary power as α is varied.

Figures 3.12-3.14 show that at resonant frequencies, the real power in the secondary is zero when the total input power is minimum. Also, the vibrational energy is a minimum at $\alpha = 1$. However, at off-resonant frequencies, the real power in the secondary is zero when the total input power is minimum but the vibrational energy is not necessarily minimum at $\alpha = 1$.

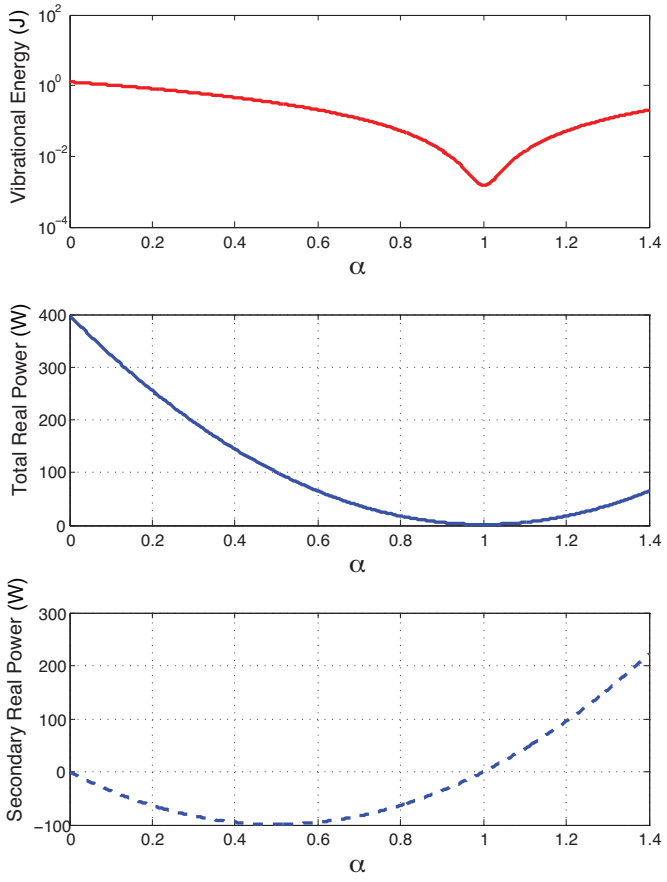

Figure 3.8: Variation of the vibrational energy (top), the total input power (middle) and the real power in secondary actuator (bottom) with α for $\omega = 620$ Hz.

At off-resonance frequencies, setting the real power in the secondary actuator to zero will not necessarily produce the greatest attenuation in vibrational energy.

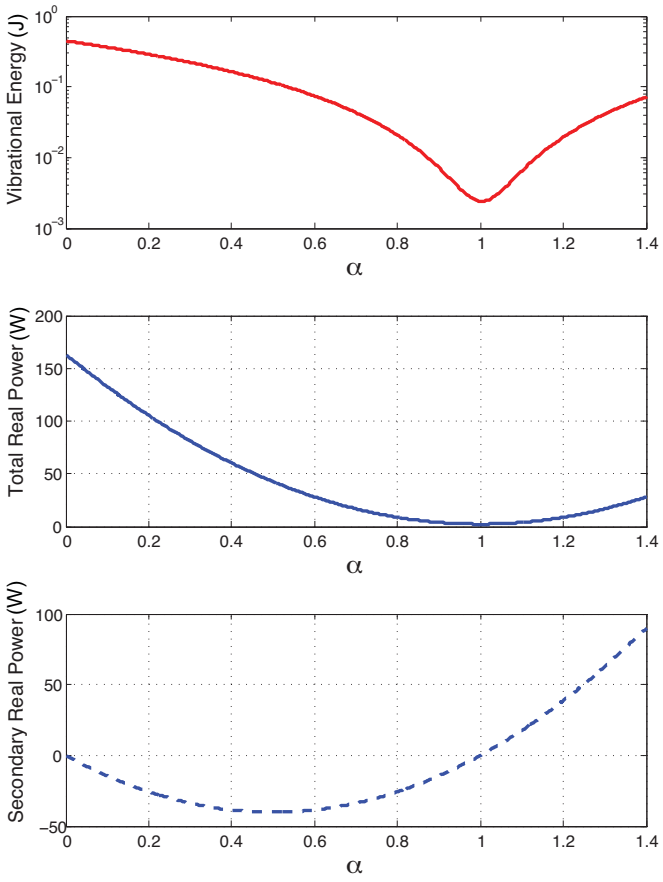

Figure 3.9: Variation of the vibrational energy (top), the total input power (middle) and the real power in secondary actuator (bottom) with α for $\omega = 724$ Hz.

3.3.5 Optimal secondary location for a frequency band

Figure 3.5 shows that the secondary actuator position $(x_s, y_s) = (0.075, 0.075)$ is not optimal for the resonant modes at $\omega_n = 1413$ Hz and $\omega_n = 1862$ Hz. If the secondary actuator location is chosen carefully, we can expect to control the above modes. We consider the frequency band 1300-1900 Hz to demonstrate optimization of the secondary actuator position. First,

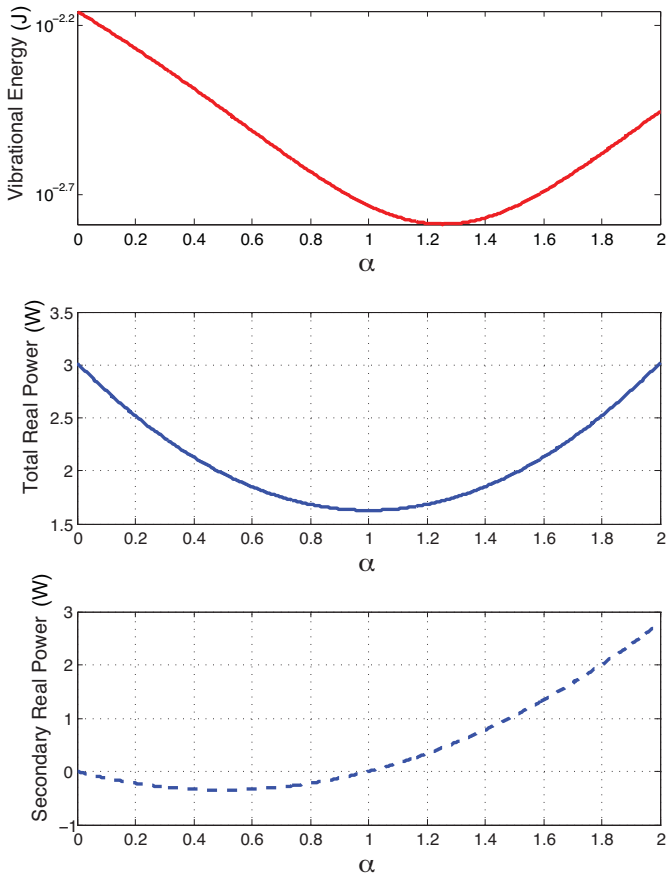

Figure 3.10: Variation of the vibrational energy (top), the total input power (middle) and the real power in secondary actuator (bottom) with α for $\omega = 680$ Hz.

we note that the peaks and valleys of the mode shape for a given resonance mode are optimal locations for controlling that mode. Let $\phi_i(x, y)$ denoted the mode shape for the resonant frequency ω_i in the frequency band 1300-1900 Hz. We define the following optimization function that is a weighted sum of the mode shapes:

$$\Phi = -\sum_i \beta_i \, \mathrm{abs}(\phi_i(x, y)) \tag{3.49}$$

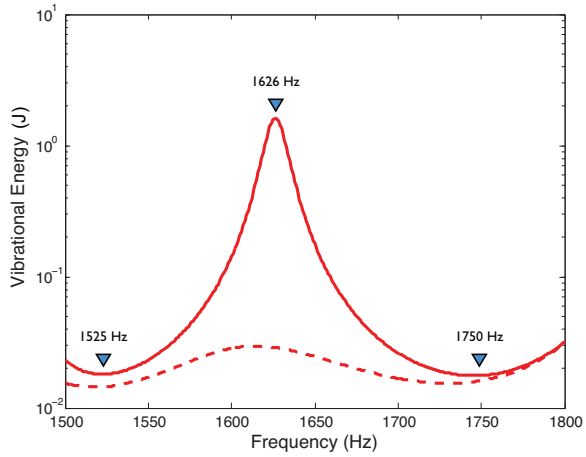

Figure 3.11: Vibrational energy of the plate with MAP control (dashed line) and without MAP control (solid line) for the frequency range 1500-1800 Hz. One resonant frequency (1626 Hz) and two off-resonant frequencies (1525 Hz and 1750 Hz) are marked by the blue triangles.

where β_i is some weight. The optimal locations for controlling the resonant modes in the frequency band are given by the minima of the function Φ. For the frequency band of interest, that is 1300-1900 Hz, there are resonances at $\omega_i = 1413$ Hz, 1474 Hz, 1626 Hz and 1862 Hz. Figure 3.15 shows the plot for Φ where the minima are given by the dark blue areas. For this example, we weight the mode shapes equally, that is, $\beta_i = 1$ for $i = 1, \ldots, 4$. Two locations of the secondary actuator are shown. One of the locations, shown by the dashed box, is the non-optimal location given by $(x_s, y_s) = (0.075, 0.075)$. The other location, shown by the solid box, is chosen to be one of the four minima and is given by $(x_s, y_s) = (0.125, 0.135)$. Note that this optimal location is farthest from the primary location $(x_p, y_p) = (0.25, 0.20)$. Figure 3.16 compares the vibration response when the secondary actuator is located at $(x_s, y_s) = (0.075, 0.075)$ and $(x_s, y_s) = (0.125, 0.135)$. Figure 3.16 clearly shows that by optimizing the location of the secondary actuator, we are able to control all the modes in the given frequency band.

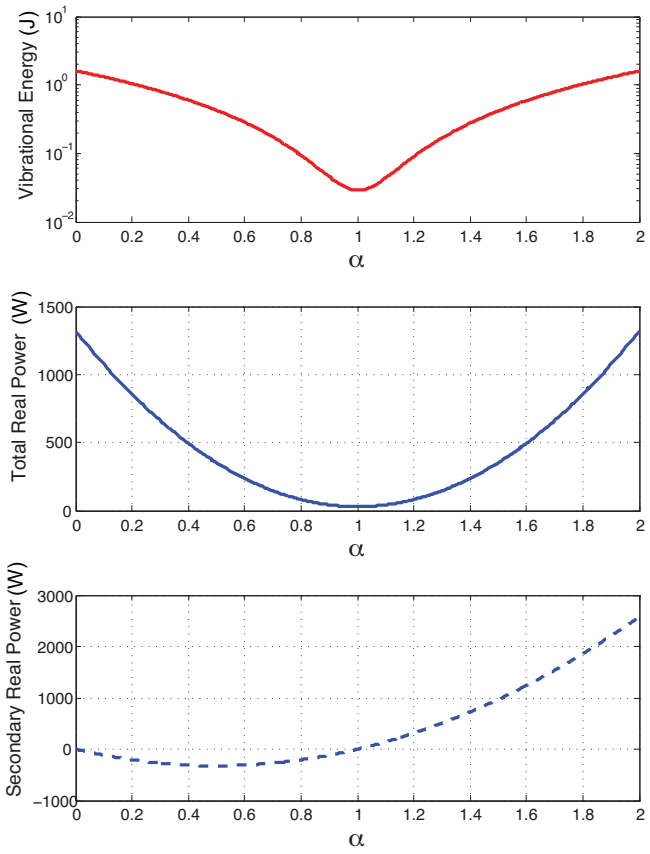

Figure 3.12: Variation of the vibrational energy (top), the total input power (middle) and the real power in secondary actuator (bottom) with α for $\omega = 1626$ Hz.

3.3.6 MAP control as a function of separation between primary and secondary patch

The effectiveness of MAP control not only depends upon the location of the secondary actuator with respect to mode shapes, as we saw in the last section, but also on the distance

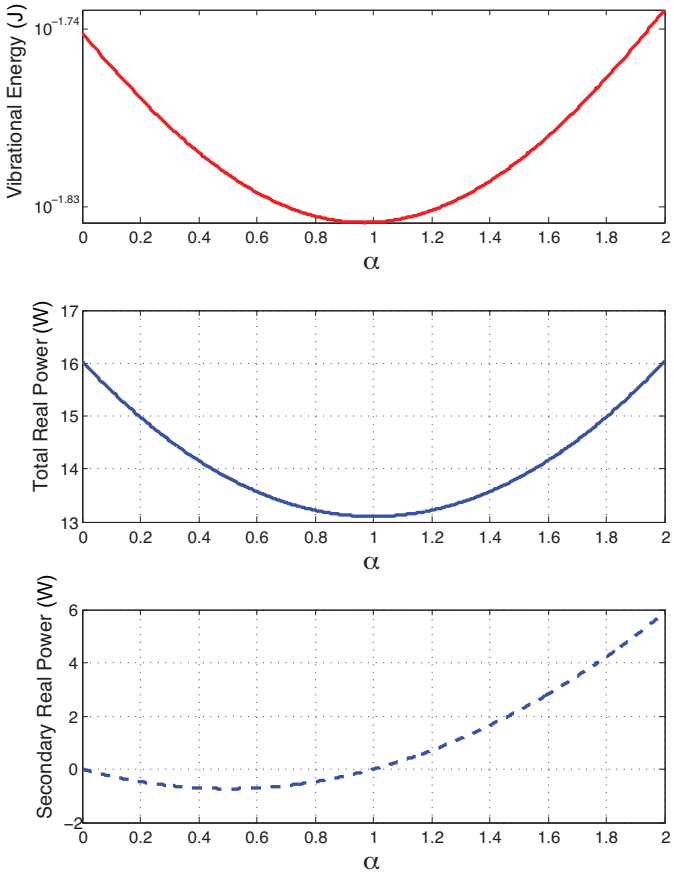

Figure 3.13: Variation of the vibrational energy (top), the total input power (middle) and the real power in secondary actuator (bottom) with α for $\omega = 1525$ Hz.

from the primary actuator. Let the reduction in vibrational energy be defined as:

$$\overline{E}_{kin}^{red} = \frac{\overline{E}_{kin} - \overline{E}_{kin}^{opt}}{\overline{E}_{kin}} \tag{3.50}$$

where $\overline{E}_{kin}^{red}$ is the normalized reduction in the vibrational energy. $\overline{E}_{kin}^{opt}$ and $\overline{E}_{kin}$ are the vibrational energies of the plate with and without MAP control respectively. Note that $\overline{E}_{kin}^{red}$ is a measure of the effectiveness of MAP control. Let the excitation frequency be 800

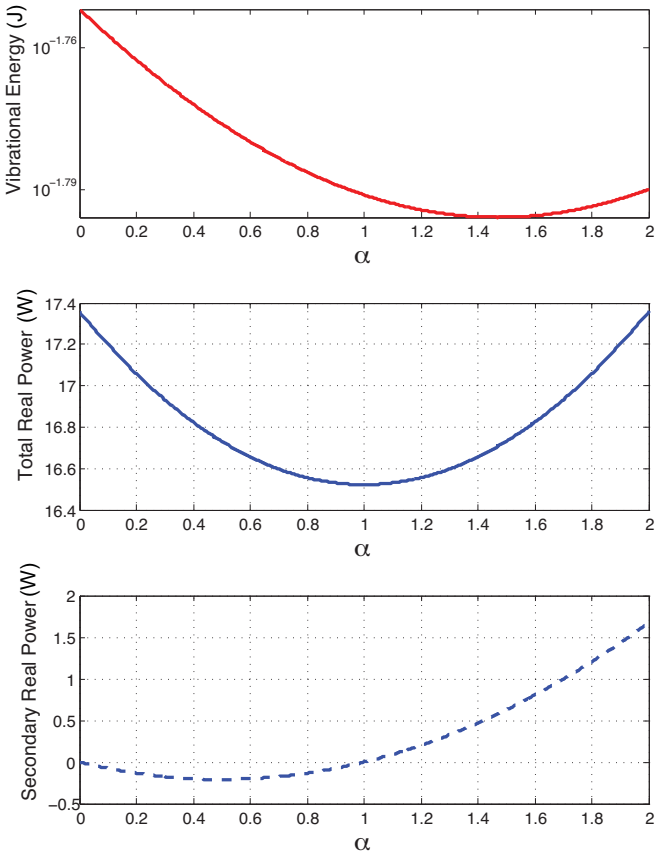

Figure 3.14: Variation of the vibrational energy (top), the total input power (middle) and the real power in secondary actuator (bottom) with α for $\omega = 1750$ Hz.

Hz (off-resonant). Figure 3.17 shows the general trend of $\overline{E}_{kin}^{red}$ with distance between the primary and secondary actuator. In general, the effectiveness of MAP control decreases as the distance between the primary and secondary actuator increases. The control is most effective when the actuators are collocated. However, this is not feasible in practice and the best one can get is sub-optimal performance. Note that at nodal lines, the effectiveness of any control is zero as seen by the dips in Fig. 3.17.

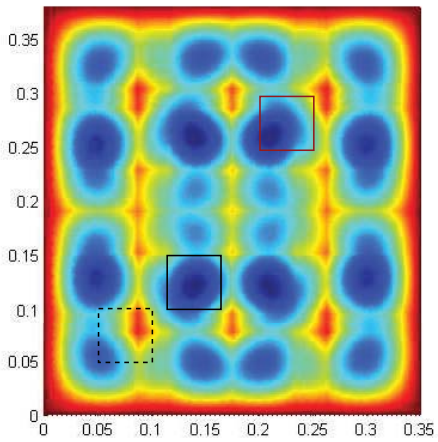

Figure 3.15: Contour plot of the optimization function Φ. Dark blue areas indicate where the function is a minimum. The dashed black box shows the original secondary patch location $(x_s, y_s) = (0.075, 0.075)$ while the solid black box shows the optimized location $(x_s, y_s) = (0.125, 0.135)$. The primary actuator is shown by the solid brown box (top right).

3.3.7 Multifrequency excitation

We present results for MAP control when the primary excitation is multi-frequency. The primary patch location is given by $(x_p, y_p) = (0.275, 0.225)$ while the secondary patch is located at $(x_s, y_s) = (0.075, 0.075)$. Without loss of generality, assume that the primary excitation has two frequencies component $\omega_1 = 1000$ Hz and $\omega_2 = 1500$ Hz. Note that ω_1 and ω_2 are commensurate (integer multiples of some base frequency). Let $M_{p1} = M_{p2} = 1$ where M_{p1} and M_{p2} are the complex amplitudes of the primary moment corresponding to ω_1 and ω_2 respectively. Let the components of the secondary moments be defined as a fraction of the corresponding optimal moments as:

$$\begin{aligned} M_{s1} &= \alpha M_{s1}^{opt} \\ M_{s2} &= \alpha M_{s2}^{opt} \end{aligned} \tag{3.51}$$

where M_{s1}^{opt} and M_{s2}^{opt} are given by (3.30) with ω replaced by ω_1 and ω_2 respectively. Recall that α is a real scalar where $\alpha = 0$ implies no control while $\alpha = 1$ implies optimal control.

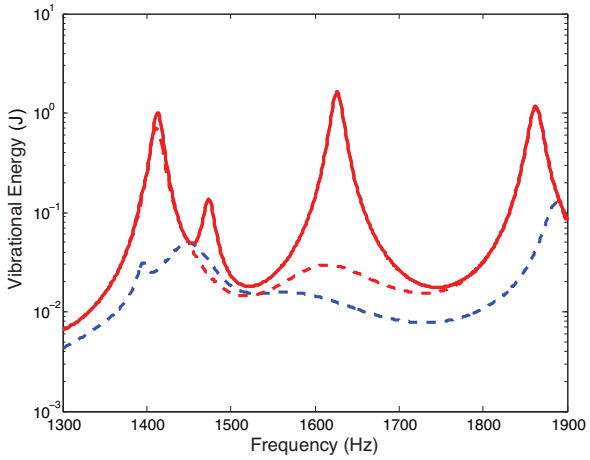

Figure 3.16: Vibrational energy of the plate. No Control (solid); Secondary actuator at $(x_s, y_s) = (0.075, 0.075)$ (red dashed line); Secondary actuator at $(x_s, y_s) = (0.125, 0.135)$ (blue dashed line).

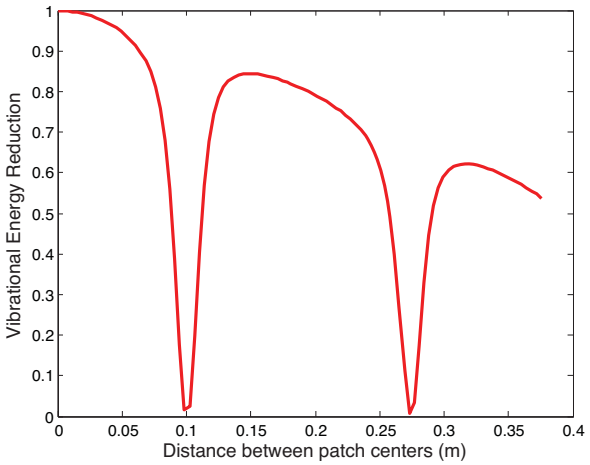

Figure 3.17: Vibrational energy reduction as function of the distance between the primary and secondary patch for $\omega = 800$ Hz.

The top plot in Figure 3.18 shows the variation of the total vibrational energy $\overline{E}$ with α.

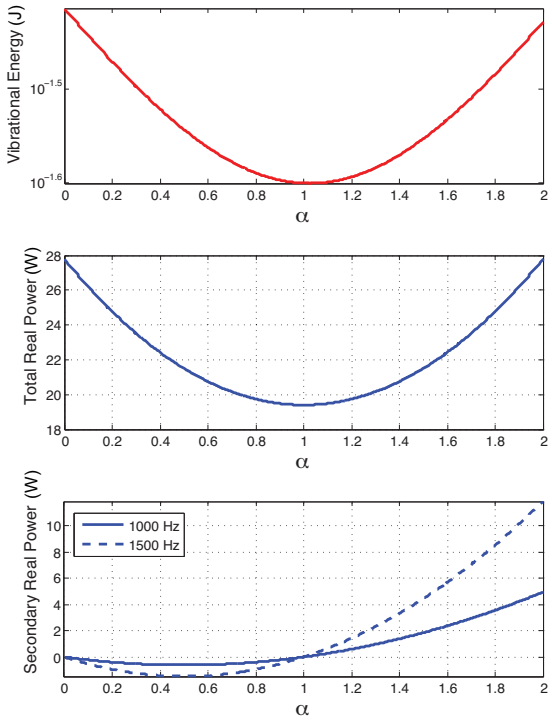

Figure 3.18: Variation of the vibrational energy (top), the total input power (middle) and the real power in secondary actuator (bottom) for multi-frequency excitation with $\omega_1 = 1000$ Hz and $\omega_2 = 1500$ Hz. The bottom plot shows the components of the real power in the secondary actuator for $\omega_1 = 1000$ Hz (solid) and $\omega_2 = 1500$ (dashed).

Note that $\overline{E} = \overline{E}_1 + \overline{E}_2$. The middle plot shows the variation of the total input power $\bar{P} = \bar{P}_1 + \bar{P}_2$ while the bottom plot shows the variation of $\bar{P}_{s1}$ and $\bar{P}_{s2}$, components of the real power in the secondary actuator corresponding to ω_1 and ω_2 respectively. The plots in Fig. 3.18 clearly show that when the total input power is minimum, the real power in the secondary actuator corresponding to each frequency is zero. Also, it can be seen that the total vibrational energy is minimum when the total input power is minimum.

3.4 MAP Implementation with Electric Actuator

In an actual experiment, the net input power from the secondary actuator is hard to measure. Rather, one can easily measure the electrical power by monitoring the voltage and current in the patch. We develop the model for electromechanical coupling between the secondary actuator and the host structure. We relate the real electrical power in the secondary actuator to the net input power through the dielectric loss. We show how the real electrical power in the secondary actuator can be used to implement a real-time MAP control algorithm.

3.4.1 Electromechanical coupling between the PZT actuator and the structure

The two dimensional strain field developed in the PZT patch actuator is commonly expressed by the following constitutive equation governing the electromechanical interaction of piezoelectric material:

$$\begin{bmatrix} \varepsilon_x \\ \varepsilon_y \end{bmatrix} = \frac{1}{Y_{11}} \begin{bmatrix} 1 & -\nu_p \\ \nu_p & 1 \end{bmatrix} \begin{bmatrix} \sigma_x \\ \sigma_y \end{bmatrix} + \begin{bmatrix} d_{31} \\ d_{32} \end{bmatrix} E_3 \tag{3.52}$$

where ε_x and ε_x are the strains in the x and y directions respectively, σ_x and σ_x are the stresses in the x and y directions respectively, E_3 is the electric field applied to the patch in the z direction, d_{31} and d_{32} are piezoelectric coupling coefficients, Y_{11} is the elastic modulus and ν_p is the Poisson ratio of the piezoelectric material. Equation (3.53) can be expressed in terms of the stress field as

$$\begin{bmatrix} \sigma_x \\ \sigma_y \end{bmatrix} = \frac{Y_{11}}{1-\nu_p^2} \left(\begin{bmatrix} 1 & \nu_p \\ \nu_p & 1 \end{bmatrix} \begin{bmatrix} \varepsilon_x \\ \varepsilon_y \end{bmatrix} - \begin{bmatrix} d_{31} \\ d_{32} \end{bmatrix} E_3 \right) \tag{3.53}$$

The electric displacement in the z direction is expressed as [43]

$$D_3 = \varepsilon_{33} E_3 + d_{31}\sigma_x + d_{32}\sigma_y \tag{3.54}$$

where ε_{33} is the complex dielectric constant of the piezoelectric material. Assuming the PZT is isotropic, that is $d_{31} = d_{32}$, we get

$$D_3 = \left(\varepsilon_{33} - \frac{2d_{31}^2 Y_{11}}{1-\nu_p}\right) E_3 + \frac{d_{31} Y_{11}}{1-\nu_p} (\varepsilon_x + \varepsilon_y) \tag{3.55}$$

If V is the voltage applied to the PZT patch, we have

$$E_3 = \frac{\mathrm{V}}{h} \tag{3.56}$$

where h is the thickness of the PZT patch. Using (3.56) in (3.55), we get

$$D_3 = \left(\varepsilon_{33} - \frac{2d_{31}^2 Y_{11}}{1-\nu_p}\right) \frac{\mathrm{V}}{h} + \frac{d_{31} Y_{11}}{1-\nu_p} (\varepsilon_x + \varepsilon_y) \tag{3.57}$$

The electric current in the PZT is given by

$$\mathrm{I} = j\omega \int_{x_1}^{x_2} \int_{y_1}^{y_2} D_3 \, dx \, dy \tag{3.58}$$

where $x_1,\ x_2,\ y_1$ and y_2 are the patch coordinates. Using (3.57) in (3.58), we get

$$\mathrm{I} = j\omega \left(\varepsilon_{33} - \frac{2d_{31}^2 Y_{11}}{1-\nu_p}\right) \frac{a^2 \mathrm{V}}{h} + \frac{d_{31} Y_{11}}{1-\nu_p} \int_{x_1}^{x_2} \int_{y_1}^{y_2} j\omega (\varepsilon_x + \varepsilon_y) \, dx \, dy \tag{3.59}$$

where a is the width of the patch. The strain rates can be written as

$$\begin{aligned} j\omega\varepsilon_x &= \frac{H+h}{2} \frac{\partial^2 v}{\partial x^2} \\ j\omega\varepsilon_y &= \frac{H+h}{2} \frac{\partial^2 v}{\partial y^2} \end{aligned} \tag{3.60}$$

where v is the transverse velocity of the plate. Using (3.60) in (3.59), we get

$$\mathrm{I} = j\omega \left(\varepsilon_{33} - \frac{2d_{31}^2 Y_{11}}{1-\nu_p}\right) \frac{a^2 \mathrm{V}}{h} + \frac{d_{31} Y_{11}}{1-\nu_p} \frac{H+h}{2} \int_{x_1}^{x_2} \int_{y_1}^{y_2} \left(\frac{\partial^2 v}{\partial x^2} + \frac{\partial^2 v}{\partial y^2}\right) dx \, dy \tag{3.61}$$

Consider the first term in the integral in (3.61):

$$\begin{aligned}\int_{x_1}^{x_2}\int_{y_1}^{y_2}\frac{\partial^2 v}{\partial x^2}\,dx\,dy &= \int_{y_1}^{y_2}\left(\left.\frac{\partial v}{\partial x}\right|_{(x_2,y)} - \left.\frac{\partial v}{\partial x}\right|_{(x_1,y)}\right)\,dy \\ &= \int_{y_1}^{y_2}\left(w_{(x_2,y)} - w_{(x_1,y)}\right)\,dy \end{aligned} \tag{3.62}$$

where w is represents the angular velocity. If the patch is discretized along the edge, then we get the following approximation:

$$\int_{y_1}^{y_2}\left(w_{(x_2,y)} - w_{(x_1,y)}\right)\,dy = \Delta e\sum_{1+3} w_i \tag{3.63}$$

where Δe is the length of the patch element and the summation is along edges 1 and 3 of the patch. Thus, from (3.62) and (3.63), we get

$$\int_{x_1}^{x_2}\int_{y_1}^{y_2}\frac{\partial^2 v}{\partial x^2}\,dx\,dy = \Delta e\sum_{1+3} w_i \tag{3.64}$$

Similarly, we can show

$$\int_{x_1}^{x_2}\int_{y_1}^{y_2}\frac{\partial^2 v}{\partial y^2}\,dx\,dy = \Delta e\sum_{2+4} w_i \tag{3.65}$$

Using (3.64) and (3.65) in (3.61) gives

$$\begin{aligned}\mathrm{I} &= j\omega\left(\varepsilon_{33} - \frac{2d_{31}^2 Y_{11}}{1-\nu_p}\right)\frac{a^2\mathrm{V}}{h} + \frac{d_{31}Y_{11}}{1-\nu_p}\frac{(H+h)\Delta e}{2}\left(\sum_{1+3} w_i + \sum_{2+4} w_i\right) \\ &= j\omega\left(\varepsilon_{33} - \frac{2d_{31}^2 Y_{11}}{1-\nu_p}\right)\frac{a^2\mathrm{V}}{h} + \frac{d_{31}Y_{11}}{1-\nu_p}\frac{(H+h)\Delta e}{2}\sum_{\text{pzt}} w_i \end{aligned} \tag{3.66}$$

where $\sum_{\text{pzt}}$ denotes summation along all the edges of the patch. Equation (3.66) can be expressed in terms of complex amplitudes as

$$\bar{\mathrm{I}} = j\omega\left(\varepsilon_{33} - \frac{2d_{31}^2 Y_{11}}{1-\nu_p}\right)\frac{a^2\bar{\mathrm{V}}}{h} + \frac{d_{31}Y_{11}}{1-\nu_p}\frac{(H+h)\Delta e}{2}\sum_{\text{pzt}} W_i \tag{3.67}$$

where $\bar{\mathrm{I}}$ and $\bar{\mathrm{V}}$ denote the complex amplitudes of the PZT current and voltage respectively while W_i denotes the complex amplitude of the angular velocity at the i^{th} element along the patch edge. The real part of the electric power is given by

$$\bar{P}_e = \frac{1}{2}\mathrm{Re}(\bar{\mathrm{V}}^*\bar{\mathrm{I}}) \tag{3.68}$$

where $*$ denotes the complex conjugate. Using (3.67) and (3.69), we get

$$\bar{P}_e = \frac{1}{2}\mathrm{Re}\left[j\omega\left(\varepsilon_{33} - \frac{2d_{31}^2 Y_{11}}{1-\nu_p}\right)\frac{a^2\bar{\mathrm{V}}^*\bar{\mathrm{V}}}{h} + \frac{d_{31}Y_{11}}{1-\nu_p}\frac{(H+h)\Delta e}{2}\bar{\mathrm{V}}^*\sum_{\text{pzt}} W_i\right] \tag{3.69}$$

Note that for a thin patch, the moment per unit length (complex amplitude) can be expressed as a function of the applied voltage (complex amplitude) as

$$\bar{M} = \frac{d_{31}Y_{11}}{1-\nu_p}\frac{(H+h)}{2}\bar{\mathrm{V}} \tag{3.70}$$

The net moment applied to the patch element is, therefore,

$$M = \Delta e\bar{M} = \Delta e\,\frac{d_{31}Y_{11}}{1-\nu_p}\frac{(H+h)}{2}\,\bar{\mathrm{V}} \tag{3.71}$$

Using (3.71) in (3.69), we get

$$\bar{P}_e = \frac{1}{2}\mathrm{Re}\left[j\omega\left(\varepsilon_{33} - \frac{2d_{31}^2 Y_{11}}{1-\nu_p}\right)\frac{a^2\bar{\mathrm{V}}^*\bar{\mathrm{V}}}{h} + M^*\sum_{\text{pzt}} W_i\right]. \tag{3.72}$$

Let

$$\varepsilon_{33} = \bar{\varepsilon}_{33}\,(1 - j\delta) \tag{3.73}$$

where $\bar{\varepsilon}_{33}$ is the real part of the complex dielectric constant and δ is the dielectric loss factor. Using (3.73) in (3.72), we get which simplifies to

$$\bar{P}_e = \frac{1}{2}\frac{\omega\,a^2}{h}|\bar{\mathrm{V}}|^2\,\bar{\varepsilon}_{33}\delta + \frac{1}{2}\mathrm{Re}\left(M^*\sum_{\text{pzt}} W_i\right) \tag{3.74}$$

Recall that the net input power (mechanical) due to the patch is given by

$$\bar{P} = \frac{1}{2}\mathrm{Re}\left(M^* \sum_{\mathrm{pzt}} W_i\right) \tag{3.75}$$

Using (3.75) in (3.74), we get

$$\begin{aligned} \bar{P}_e &= \frac{1}{2}\frac{\omega\, a^2}{h}|\bar{\mathrm{V}}|^2\, \bar{\varepsilon}_{33}\delta + \bar{P} \\ \bar{P}_e &= \bar{P}_\ell + \bar{P} \end{aligned} \tag{3.76}$$

where $\bar{P}_\ell$ is the dielectric loss. Equation (5.51) gives the relation between the net input electrical power and net input mechanical power.

3.4.2 Real-time control algorithm to implement MAP for a single secondary actuator

From Eq. (5.51), the real power in the secondary actuator can be expressed as

$$\bar{P}_{se} = \bar{P}_{s\ell} + \bar{P}_s \tag{3.77}$$

where

$$\bar{P}_{s\ell} = \frac{1}{2}\frac{\omega\, a^2}{h}|\bar{\mathrm{V}}_s|^2\, \bar{\varepsilon}_{33}\delta \tag{3.78}$$

is the dielectric loss, $\bar{P}_{se}$ is the net electrical power in the secondary actuator, $\bar{P}_s$ is the net mechanical input power from the secondary actuator and $\bar{\mathrm{V}}_s$ is the complex amplitude of the voltage applied to the secondary actuator. Since $\bar{P}_s = 0$ at optimal control, equation (3.77) shows that at optimal value of control, the net electrical power in the secondary actuator is given by the following *baseline* value:

$$\bar{P}_{se} = \bar{P}_{s\ell} \tag{3.79}$$

Equation (4.31) shows that setting $\bar{P}_{se} - \bar{P}_{s\ell} = 0$ (with $\bar{\mathrm{V}}_s$ non-zero) provides a novel way to implement MAP control.

Next, we present simulations to illustrate the implementation of MAP control. The primary and secondary actuators are symmetrical with respect to the center of the plate. Specifically, $(x_p, y_p) = (0.305, 0.275)$ and $(x_s, y_s) = (0.075, 0.075)$. The voltage applied to the primary actuator is V_p =10 volts. Figure 3.19 shows the real electrical power in the primary actuator, $\bar{P}_{pe}$, with and without MAP control as a function of frequency. In case of perfect control, that is, $\bar{P}_p = 0$, the real electric power in the primary actuator is simply the dielectric loss. The top plot in Fig. 3.20 shows the variation of the total vibrational energy with the secondary voltage at the resonant frequency $\omega_n = 620$ Hz while the bottom plot shows the variation of real electric power in the primary and secondary actuators and the secondary loss. Because of symmetry in actuator location, the optimal secondary voltage is $V_s = 10$ V. It can be seen clearly that the secondary voltage is optimal at the intersection of the secondary real electric power and the secondary loss as given by Eq. 4.31.

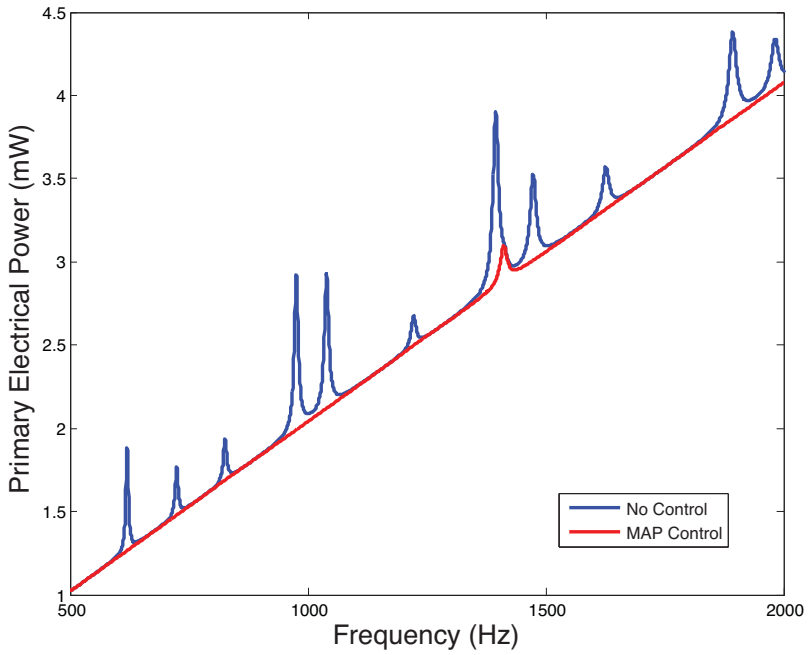

Figure 3.19: Real electric power in the primary actuator with and without MAP control.

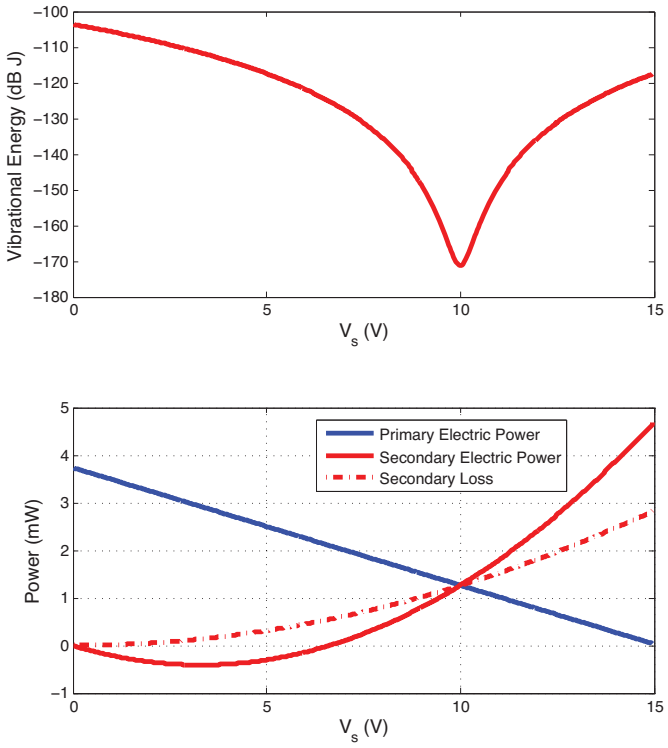

Figure 3.20: (top) Vibrational energy as a function of the secondary voltage at $\omega_n = 620$ Hz. (bottom) Real electric power in the primary and secondary actuators and the secondary loss as a function of the secondary voltage.

3.5 Experimental Demonstration of MAP

The theoretical findings just described provide the groundwork and guide an experimental validation. A test setup that closely mimics simply supported boundary conditions was built. One primary and one secondary patch actuator was symmetrically bonded to the plate structure. The symmetrical location of the actuators helps validation as the optimal secondary voltage is expected to be equal in magnitude to the primary voltage. The theoretical findings show that at optimal control, the net input power from the secondary actuator is identically zero. The net input power from the secondary actuator can be indirectly computed by

measuring the real electric power supplied to the secondary actuator and calculating the dielectric loss. If the dielectric loss is accurately characterized, then MAP control can be implemented by solely monitoring the real electric power supplied to the secondary actuator.

3.5.1 Overview of experimental verification

We have shown that for a structure excited by a single primary actuator and controlled by a single secondary actuator, MAP control for vibration minimization of a single harmonic excitation can be practically implemented by monitoring, regulating and matching the real electric power of the secondary actuator to a predetermined value. Recall that at optimal control, the net input mechanical power from the secondary actuator into the structure diminishes. The net input power is related to the real electric power by the following simple relation:

$$\bar{P}_s = \bar{P}_{se} - \bar{P}_{s\ell}$$

where $\bar{P}_s$ is the net input power, $\bar{P}_{se}$ is the real electric power and $\bar{P}_{s\ell}$ is the electric loss. Thus, at optimal control, the real electric power in the secondary actuator ideally reduces to its electric resistive loss, or the dielectric loss for a piezoelectric actuator. The process of MAP control then simply reduces to the measurement and regulation of electric power , which is far easier than that of its mechanical counterparts, the vibratory angular velocity and bending moment. It is important to note that the dielectric loss is a known function of the piezoelectric material properties, excitation frequency, and the electric field applied (voltage). The dissipative power of the actuator is a quadratic function of the driving voltage. As the secondary actuator voltage increases, both the real power consumption and the electrical loss increase, although at different rates. Therefore, the optimal control voltage V_s could be determined by the interception of the real time power measurement with the electrical loss, as illustrated in Fig. 3.20. For a given primary voltage $V_p = 10$ volts, it shows variation of the power as the secondary voltage is increased from 0 to 15 volts. The optimal secondary voltage for the minimum vibrational energy is determined by the intersection of $\bar{P}_{se}$ and $\bar{P}_{sl}$. The experimental implementation of the MAP control for each single frequency consists of two steps: 1) determining the actuator electrical loss as the control baseline and 2) varying the secondary voltage with respect to the primary voltage until the measurement of the real power matches a predetermined resistive power loss. The MAP control of multiple

frequencies is obtained by matching the total electric power of all the sinusoidal excitations to the sum of the electric losses for all the frequencies.

3.5.2 Test instrumentation

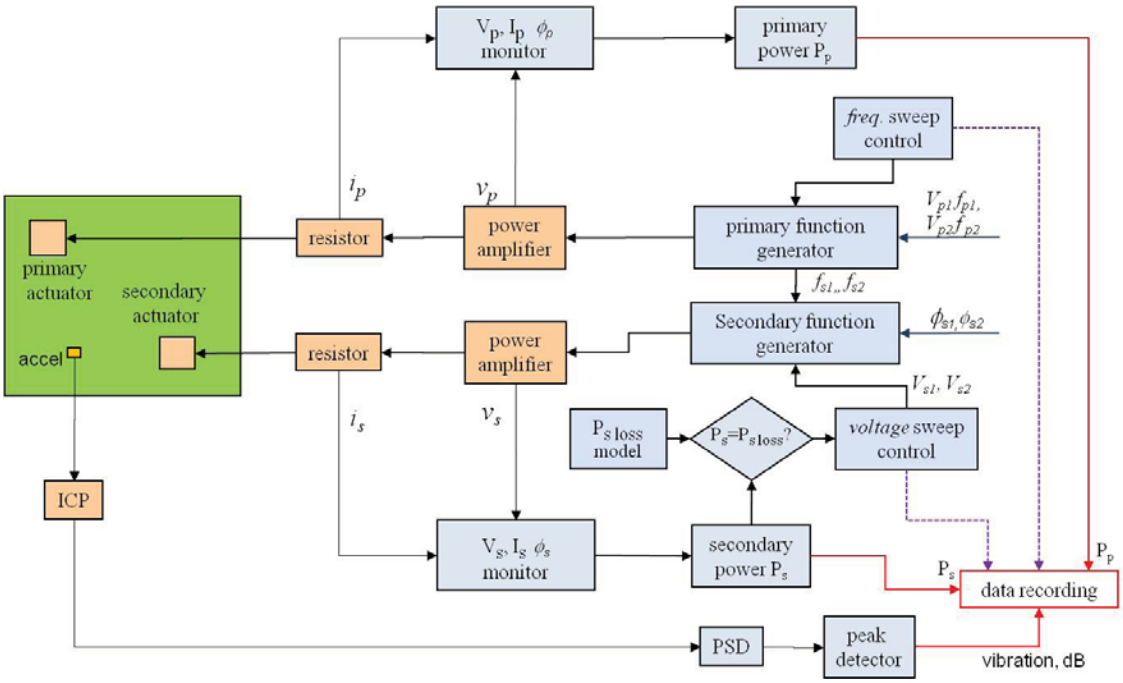

Figure 3.21: Instrumentation of MAP experimental verification.

The experimental process for MAP verification consists of multiple channel frequency signal generating, voltage and frequency sweep, complex power measurement, and vibration monitoring, as shown in Fig. 3.21. The two audio power amplifiers with line transformers are used to drive the primary and secondary actuators having a common electric grounding. The real electric power in the secondary actuator is calculated from the secondary voltage and the current sampled by a precision resistor on the drive circuit. The real power of each actuator is monitored and recorded as function of drive frequency, voltage, and phase inputs. The vibration level of the plate structure is monitored by an accelerometer mounted on the

plate at a location away from most of the node lines of the modes (frequencies) being analyzed. The secondary power is then compared against the baseline electric loss prediction while the vibration level is monitored. The measurement system is programmed in Labview. The power consumption of the piezoelectric actuators as function of frequency is also independently characterized with an HP 4194 electric impedance analyzer.

3.5.3 Structural test apparatus

The experiment test apparatus is made of a simply supported thin aluminum plate. The plate is sandwiched between two steel plate frames, as shown in Fig. 3.22. The aluminum plate is V-notched around its four clamped edges to emulate flexible hinges with minimal rotational stiffness. The two steel frames are bolted together to create highly rigid mass blocks providing a nearly clamped boundary condition to the aluminum plate edges beyond the notch, as shown in Fig. 3.23. Two thin piezoelectric patches are bonded to the plate as the primary and secondary actuators.

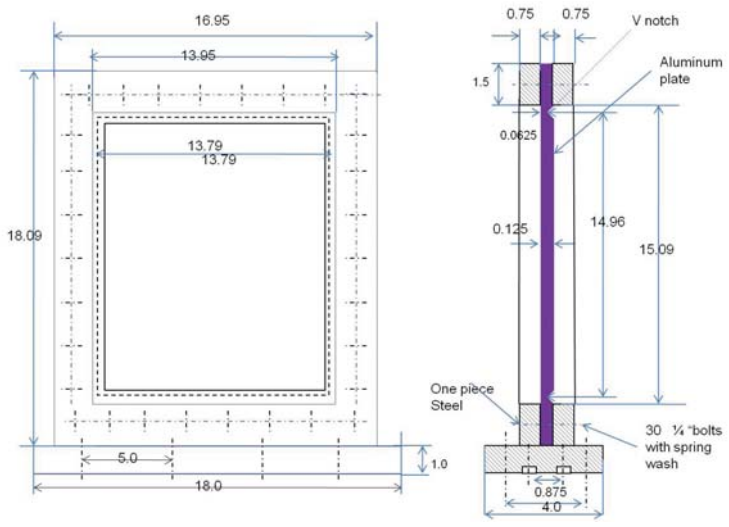

Figure 3.22: Test apparatus of simply supported plate for map validation.

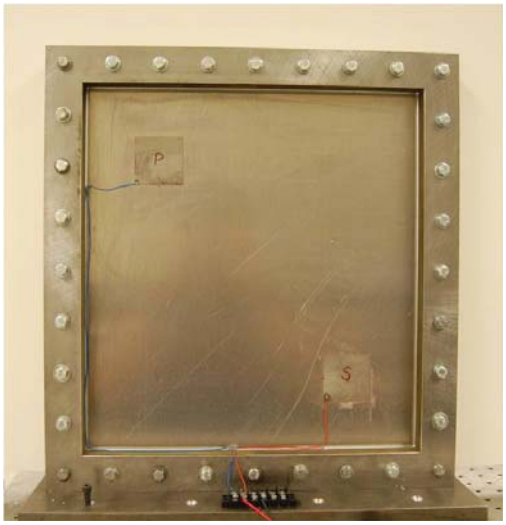

Figure 3.23: The aluminum plate test apparatus with a primary actuator and a secondary actuator.

The piezoelectric patch actuators are made of PZT 5H material with nickel plating on both side as electrodes. They are directly bonded to the aluminum plate with low viscosity adhesive Loctite 495. A uniform pressure is applied to the actuators by vacuum bag during the adhesive curing to minimize the thickness of the adhesive layer and minimize the electric and dielectric losses. Since the adhesive is semi-conductive, the two actuators therefore use the aluminum plate as a common electrode to complete their drive circuit. The dimensions and material properties for the plate and PZT patch are provided in Table 4.2.

3.5.4 Implementation of MAP control

A critical step for MAP validation is to establish the control baseline, which is to be derived from the electric power loss of the secondary actuator. We have surveyed the actuator power consumption characteristics in the frequency range of interest by an electric impedance analyzer. The HP 4194 electric impedance analyzer measures complex impedance as a function of frequency for low voltages (2.8 Vp-p). Figure 3.24 shows a frequency sweep of

Table 3.2: Geometry and material properties for plate and PZT patch.

Variable	Value
L_x	0.38 m
L_y	0.35 m
H	4.2e-3 m
E	70e9 Pa
η	0.01
ρ	2700 kg/m^3
μ	0.33
a	0.05 m
h	0.13e-3 m
Y_{11}	6.6e10 Pa
d_{31}	-190e-12 m/V
$\bar{\varepsilon}_{33}$	1.53e-8 F/m
ν_p	0.35

the real electric power deduced from the complex impedance measurement of both actuators mounted on the plate.

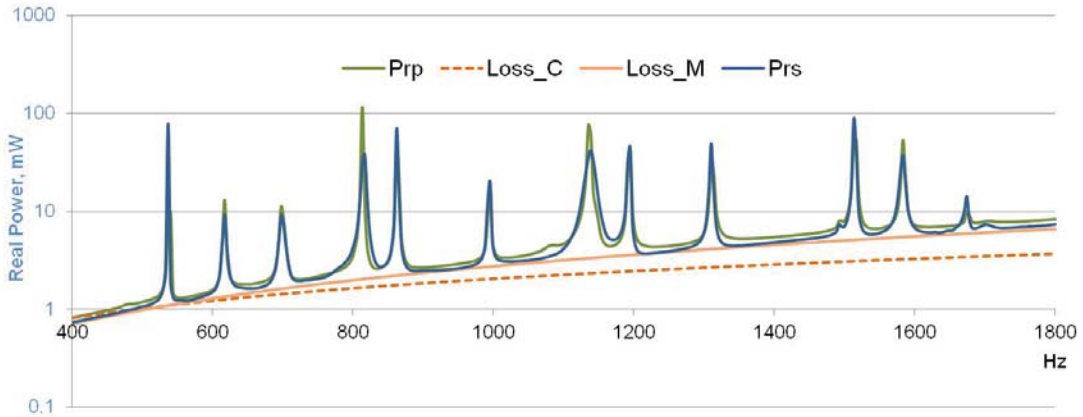

Figure 3.24: Real electric power of the primary ($\bar{P}_{rp}$) and secondary ($\bar{P}_{rs}$) actuators, their dielectric losses at 10 V excitation.

As a result of the electromechanical coupling of the piezoelectric actuators to the plate, the real electric power plots of both actuators $\bar{P}_p$ and $\bar{P}_s$ reveal not only the electric power loss of the actuators themselves but also the structural dynamics and power coupling variation with frequency. A few observations can be made by this survey. The real electric power, linearly proportional to the mechanical power of the actuator, maps the plate vibration amplitude well. The actuator power increases substantially when the plate is resonance and collapses to a small baseline level when off-resonance. The actuator power off-resonance shows a general linear dependence with frequency. Although the primary and secondary actuators are symmetrical relative to the center of the plate and possess an identical geometry, their power consumption differs noticeably at resonance frequencies. This implies variation in their control authority when one is used as a primary and the other is the secondary.

Figure 3.24 also compares the electric loss of the actuators as potential control baselines. One of them (Loss_C) is predicted by an analytical model (Equation 5.51) assuming a constant piezoelectric material loss tangent and the other (Loss_M) predicted by curve fitting the power measurement $\bar{P}_{rs}$ and $\bar{P}_{rp}$ at their off-resonance frequencies, respectively. The significant difference between these two loss estimates as control baseline candidates leads us to believe that a more comprehensive actuator characterization is necessary in order to validate the MAP control algorithm by the power interception approach mentioned early. The red dots indicate resonant frequencies and purple dots indicate the off-resonant frequencies selected for MAP validation later. The results are discussed in sections to follow.

3.5.5 Actuator electric loss characterization

We considered three methods to estimate the MAP control baseline from the actuator electric loss.

1. Analytical linear relation in Equation 5.51 taking piezoelectric material loss tangent as constant (orange dash line in Fig. 3.24. This model, although simple and easy to follow, lacks sufficient fidelity when used in the power interception algorithm for MAP control. Measurement of the piezoelectric material by the electric impedance analyzer

reveals a variation of 250% in the loss tangent of PZT 5H piezoelectric in frequencies between 100 Hz and 2000 Hz, in constract to the nominal constants of 0.02 published by the material manufactures and academia as shown in Fig. 3.25. The loss tangent also largely depends on the electric field even at the low field intensity (0.2∼2V/mil) and varies by more than 50% when the voltage changes by one order of magnitude (1∼10V).

2. Empirically curve fitting to the power measurement of the on-line actuator (mounted on the plate) at its off-resonance frequencies (orange solid line in Fig. 3.24). The baseline thus obtained is a direct measurement and a system calibration of the actuator on the structure represents the true power characteristics at all frequencies.

3. Empirically curve fitting to an off-line or null actuator. The off-line actuator has the same size as the on-line but is mounted to a solid and thick aluminum block with very high flexural stiffness. When actuated, it induces nearly zero strain in the block so the patch actuator essentially behaves like a pure electric capacitor with only dielectric loss. Therefore, curve fitting to its power measurement represents a good control baseline of the optimal control condition, that is, when the vibration completely diminishes.

The observed strong dependence on the material property and mismatch of the power in the initial MAP testing suggests that we may not be able to use the simple dielectric loss model for the control power estimate and would need to map out experimentally the actuator's power loss in the entire frequency range of interest as a function of the applied electric field. We have constructed a null actuator, characterized its loss as a function of frequency and voltage, for comparison to the actuator on the plate. Figures 3.26 and 3.27 show the electric power survey of the plate-mounted actuator and null actuator, respectively. The power is measured between resonance frequencies of the plate, from 400 Hz to 2000 Hz, for drive voltages of 1V-10V. A large difference can be seen between the loss estimates for the two actuators. The null actuator consumes less power since its measurement was taken at nearly zero residual vibration and will likely represent the lower boundary of MAP control baseline. Comparatively, the plate-mounted actuator consumes more power for the same frequency and drive voltage, and therefore constitutes a poor estimate for control baseline as the vibration at the optimal control never truly becomes zero.

3.5.6 MAP control validation

The MAP control of plate vibrations is performed using the instrument setup described previously in Fig. 3.21. The MAP validation is done by sweeping the secondary voltage while monitoring the plate vibration at various frequencies, both resonant and non-resonant, between 400 Hz and 2000 Hz. The secondary voltage at which the measured $\bar{P}_s$ equals the control baseline $\bar{P}_s$-*opt* is then considered as the optimal voltage. For this study, the power loss measured with the actuator mounted on the aluminum plate was used. For the MAP control testing to follow, the baseline loss values at each resonance are calculated by linear interpolation between loss values computed at two adjacent non-resonance frequencies. The MAP control criterion was tested for validation on both single sinusoidal excitation and dual sinusoidal excitation. For most of the frequencies selected for testing, the MAP control criterion holds whether they are on-resonance or off-resonance. The degree of control authority demonstrated very much depends on the placement of the control actuator (secondary) relative to the source (or primary actuator).

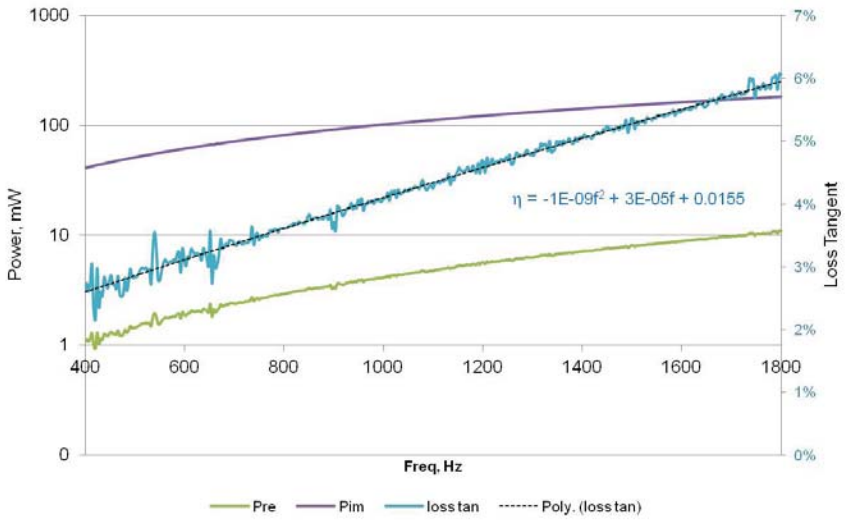

Figure 3.25: Material dielectric loss of a null actuator mounted on a solid aluminum block.

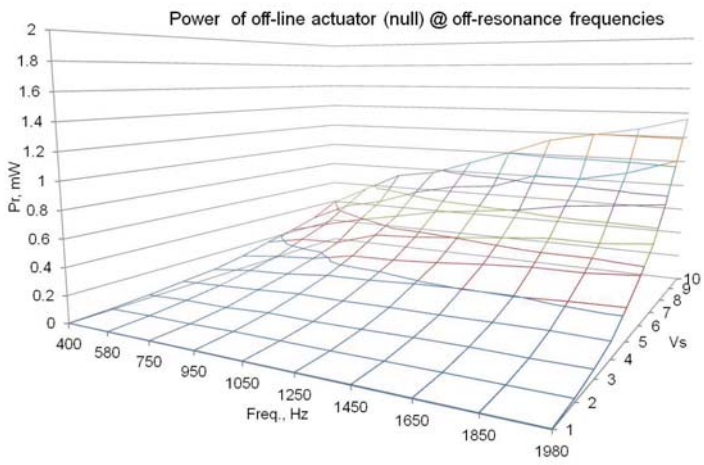

Figure 3.26: The power loss of null actuator mounted on aluminum block as MAP control baseline metric.

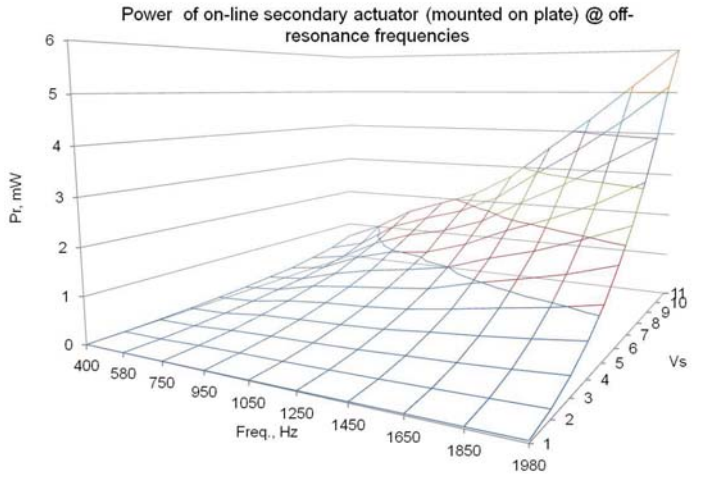

Figure 3.27: The power loss of the on-line actuator mounted on aluminum plate as MAP control baseline metric.

Single frequency: on-resonance and off-resonance

Figure 3.28 presents the results of MAP control at four of the plate's resonance frequencies; 539, 816, 1136 and 1514 Hz, respectively, as illustrated by the red dots in Fig. 3.24. Each

plot shows the primary, secondary power, the control baseline and vibration in dB as function of secondary voltage V_s while the primary voltage V_p is fixed to 10 V. The interception of the $\bar{P}_s$ with the control baseline is defined as the optimal control voltage V_s-opt predicted by MAP. The secondary voltage that minimizes the plate vibration is V_s-min dB. The difference between the two voltages represents a deviation of the MAP prediction from the measurement. The case of 1136 Hz shows nearly perfect agreement between the prediction and the measurement. The primary and secondary power also meet at the optimal secondary voltage, reflecting the fact that the boundary conditions and actuator placement are nearly symmetric. The results at 539 Hz illustrate a good match between optimal and minimum plate vibration. However, the MAP result under-predicts the optimal control voltage at both 812 Hz and 1514 Hz. While the vibration minimum occurs at 10 V and 9 V respectively, the secondary power intercepts the baseline at 8.6 V and 8.2 V, respectively.

Figure 3.29 presents the results of MAP control at three frequencies between the plate resonance frequencies: 580, 1050 and 1450 Hz, as illustrated by the purple dots in Fig. 3.24. Each plot shows the primary, secondary power, the control baseline and vibration in dB as function of secondary voltage V_s while the primary voltage V_p is fixed to 10 V. As can be seen, the MAP optimal control voltage is a fair match to the voltage at minimum vibration for 589 and 1050 Hz. The prediction off-resonance overshoots the target, which is in contrast to the case on-resonance at1450 Hz, the MAP criterion fails as the secondary power does not intercept the baseline at all.

The performance of MAP control is summarized in Fig. 3.30 which compares the measured control voltage (intersection of real electric power with the control baseline) to the measured minimum vibration voltage. As observed, the control error varies with frequency up to 15% of the targeted values. The MAP prediction at resonance frequencies appears to under-estimate the minimum vibration voltage, while the opposite happens between resonances. The overall deviation between the MAP optimal voltage and the voltage at minimum vibration averages at 4%.

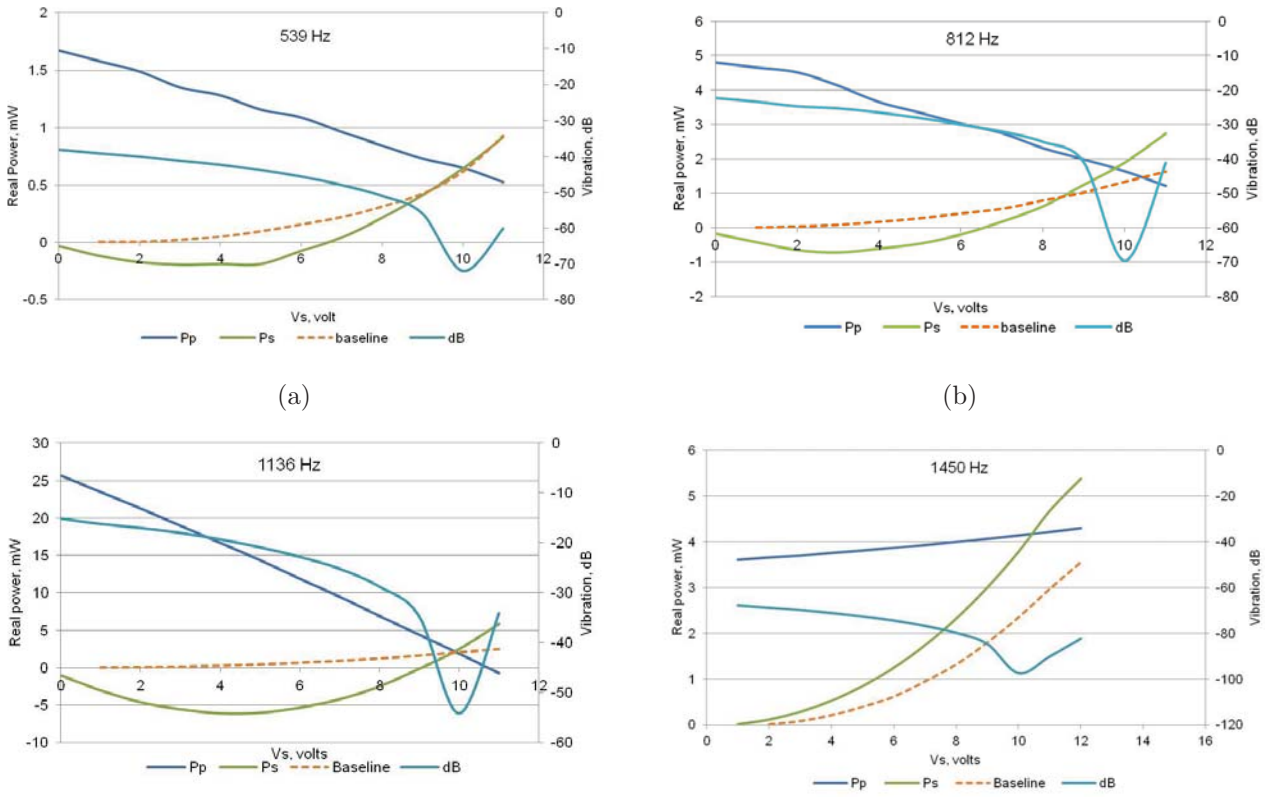

Figure 3.28: Actuator power at four on-resonance frequencies of the plate.

Multiple frequency excitation

To validate the effectiveness of MAP control on a multiple frequency excitation, we have simultaneously applied two frequencies, 539 Hz and 812 Hz to the primary and secondary actuators. The analytical model of the multiple frequency excitation case shows that the total power and total loss (and therefore the control baseline) are the sums of that of each frequency components when the two frequencies are commensurate. Figure 3.31 shows summation of the primary power, secondary power, the control baselines by each frequency component.

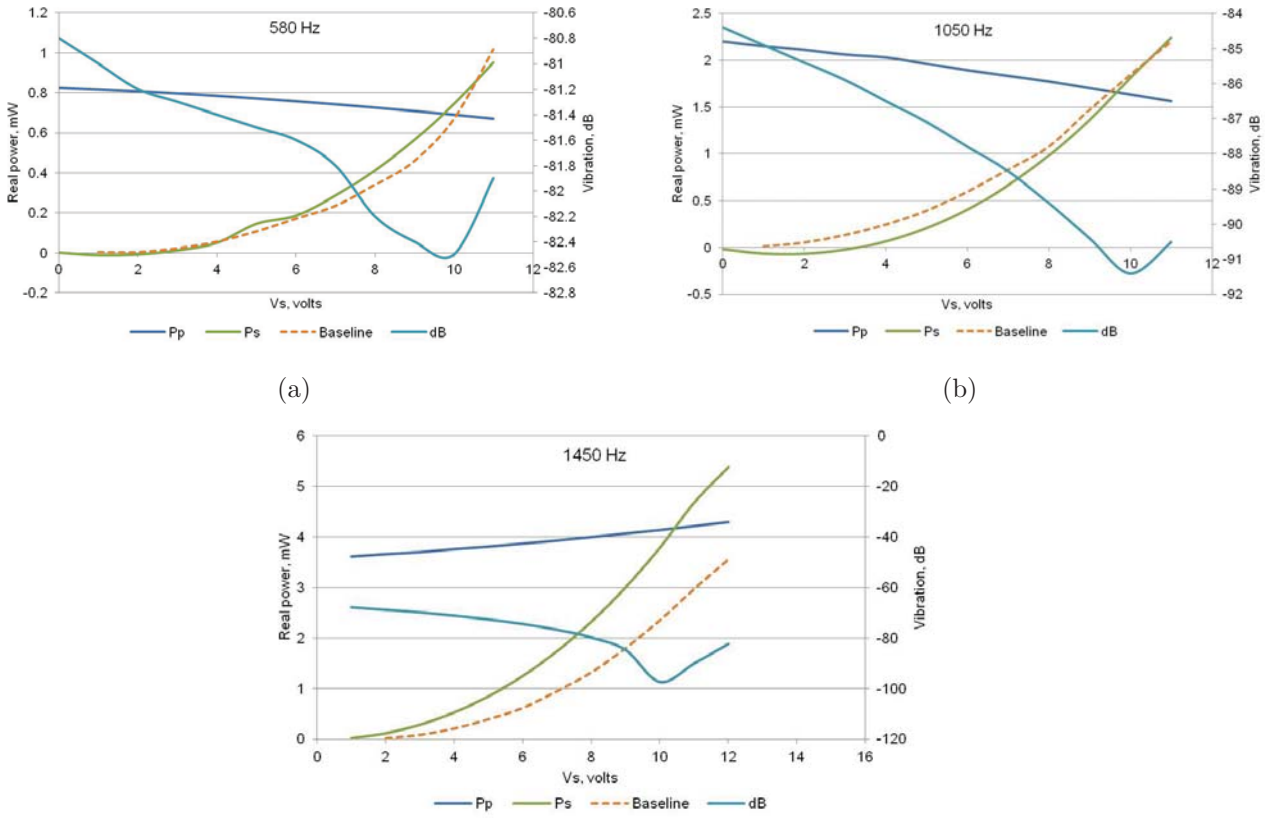

Figure 3.29: Actuator power at three off-resonance frequencies of the plate.

Two resonances of the plate are chosen for this verification. The vibration reduction in this case is calculated by the change in total energy at both frequencies. The primary voltage is fixed to 5V while the secondary is swept from 1 V to 5 V for both frequencies. The MAP optimal control voltage is V_s-opt=4.2 V for both frequencies while the vibration minimum occurs at 4.5 V, as shown by Fig. 3.31. A total vibration reduction of 15 dB is observed at MAP optimal voltage. Consistent with the trend seen earlier at individual frequencies, the MAP voltage is below the minimum vibration voltage by 4.5%.

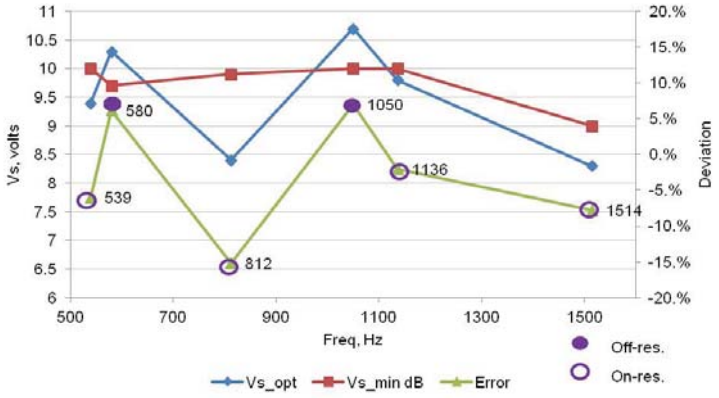

Figure 3.30: MAP prediction error analysis at on-resonance and off-resonance frequencies. V_s-*opt*: predicted by MAP (interception), V_s-*min* dB: actual corresponding to the minimum vibration.

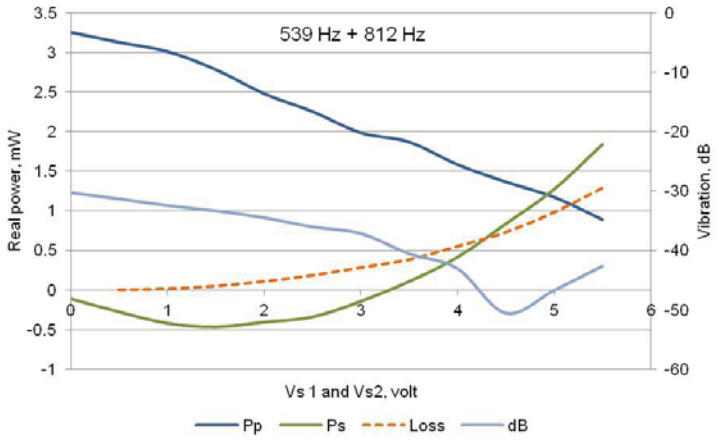

Figure 3.31: The power and loss of primary and secondary actuators under two resonance frequency excitation, 539 Hz and 812 Hz, simultaneously.

Table 3.3 summarizes the control effectiveness of MAP control at resonance and off-resonance frequencies.

Table 3.3: MAP control effectiveness at resonance, off-resonance and multi-frequency excitations.

Mode	On-Resonance				Off-Resonance			Dual Frequency
Freq, Hz	539	816	1136	1514	580	1050	1450	539 + 816
MAP Prediction Error %	-6	-15	-2	-8	6	7	n/a	-4.5
dB in reduction	-33.7	-47.2	-39.1	-42.2	-1.7	-7	n/a	-20

The experimental investigation of the simply supported plate with a single primary and single secondary actuator has demonstrated the effectiveness of the proposed MAP control algorithm for active structural vibration control. It has also identified some of the potential challenges with the implementation. Using an empirically derived actuator electric loss model as the control baseline, the MAP control approach produces good vibration reduction in a broad frequency range of the structure except at one tested frequency. The difference between accuracy of the MAP optimal voltage and the voltage corresponding to minimum vibration varies by frequency and modal status (resonance or non-resonance) of the structure with observed average difference below 10%. The difference between the MAP voltage and the minimum vibration voltage depended on whether the excitation frequency was between resonances or at a resonance.

Vibration reduction produced by the secondary actuator is very effective at structural resonance mode for both single frequency and dual frequency vibration ($>$ 20dB). However, it is much less effective between resonances off-resonances ($>$ 1.7 dB). This does not necessarily suggest that MAP control is not effective at off-resonance frequencies. The effectiveness of MAP control depends on the location of the secondary actuator with respect to the primary actuator. Optimizing the location of the secondary actuator can substantially improve the performance of MAP control between resonances (see §3.3.6).

The most critical step in experimental implementation of the MAP is identified as the estimate of the control baseline with the specific piezoelectric actuator on the structure. It is essential that the electric loss metric be based on or calibrated against an actual measurement of the actuator being used for control.

3.6 Summary

We summarize this chapter by stating the key accomplishments

- The theory of MAP was developed for a structure excited by a single primary excitation and controlled by a single secondary excitation.
- An analytical model for a simply supported plate excited and controlled by piezoelectric actuator was developed.
- An electromechanical coupling model of a piezoelectric patch actuator on a structure is developed and integrated with the MAP model.
- MAP AVC was demonstrated on a simply supported plate experimentally at discrete excitation frequencies, both resonant and off-resonant.

Chapter 4

MAP Control for Multiple Primary and Multiple Secondary

In chapter §3, we laid the foundations of MAP control and developed the theory for single primary and single secondary actuator. Simulations and experimental results were presented to validate the theory. In this chapter, we focus on extending the theory of MAP control to multiple primary excitations and multiple secondary actuators with an emphasis on developing modeling capability and a real time control algorithm to demonstrate the technology's effectiveness and ease of implementation on a rotorcraft interior panel structure. In §4.1, we develop the system model for MAP control of a simply supported plate that is excited by multiple primary piezo-electric (PZT) patch actuators and controlled by multiple secondary PZT patch actuators. In §4.2, we present numerical simulations for a simply supported plate excited by two primary patches and controlled by two secondary patches and evaluate MAP control performance as a function of the number and location of secondary patch actuators. In §4.3, we report experimental results that demonstrate MAP control of multiple primary excitations with multiple secondary actuators and quantify MAP performance and effectiveness in terms of vibration reduction and secondary power requirements.

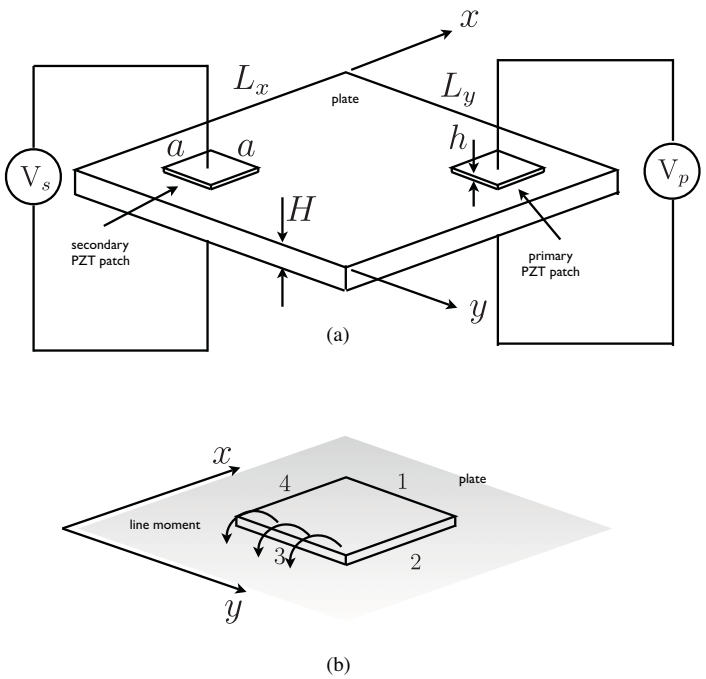

Figure 4.1: (a) Schematic of a simply supported rectangular plate excited by PZT actuators (b) Distributed moment generated by a patch.

4.1 System Model For Theoretical Simulations

4.1.1 System description

We consider a simply supported rectangular plate that is excited by N_p primary PZT patch actuators and controlled by N_s secondary PZT patch actuators. For sake of illustration, Fig 4.1(a) shows the plate excited by one primary PZT patch and one secondary PZT patch. Each actuator is driven by a voltage source. The primary patch acts as the disturbance while the secondary patch is the control actuator. Let L_x, L_y and H be the length, width and thickness of the plate respectively. The PZT patches are bonded to the plate surface and are

assumed to be square with width a and thickness h. When an electric field is applied to the patch in the z direction, the patch expands and contracts in both the x and y directions. The resulting strain field generates a distributed moment along the edges of the patch, labeled 1 to 4, as shown in Fig 4.1(b).

We make the following assumptions:

- The plate is isotropic.
- The patch is thin and the patch inertia and stiffness are ignored.
- The primary and secondary patches are identical.
- No losses are added due to the patch bond to plate
- The boundary conditions are simply supported.

4.1.2 Total input power minimization for multiple primary and secondary patch excitation

In the Multi-Actuator Data package submitted previously this year, we developed the theory of MAP for multiple primary sources controlled by multiple secondary sources. For simplicity, we assumed the primary and secondary sources to be point forces. However, the experimental setup uses PZT patches as actuators that generate line moments along the patch edges instead of a point force. For completeness, we present the theory of MAP for multiple primary and multiple secondary patch actuators to match the experiments. It should be noted that the analysis and some key observations are similar to the point forces previously reported but it is important to close the loop on the theory and experiments. The point forces are replaced by moments and the linear mobilities replaced by equivalent angular mobilities.

The theoretical development of input power minimization for multiple primary and multiple secondary actuators follows closely the analysis for a single primary actuator controlled by

single secondary actuator. Let $\hat{M}_{pi}$ and $\hat{M}_{si}$ be the moments per unit length (complex amplitude) generated by the i^{th} primary and i^{th} secondary patch respectively. Let the primary and secondary patch edges be discretized into an equal number of elements and let Δe be the length of the edge element. Then, the moments generated by each element of the i^{th} primary and i^{th} secondary patch, respectively, are

$$\begin{aligned} M_{pi} &= \Delta e\, \hat{M}_{pi} \\ M_{si} &= \Delta e\, \hat{M}_{si} \end{aligned} \tag{4.1}$$

Let

$$\boldsymbol{M}_p^T = [M_{p1} \quad M_{p2} \quad \dots \quad M_{pN_p}] \tag{4.2}$$

represent the moment vector due to N_p primary patches and

$$\boldsymbol{M}_s^T = [M_{s1} \quad M_{s2} \quad \dots \quad M_{sN_s}] \tag{4.3}$$

represent the moment vector due to N_s secondary patches. We assume that the primary and the secondary patch moments are harmonic with frequency ω. Let

$$\boldsymbol{M}^T = [\boldsymbol{M}_p^T \quad \boldsymbol{M}_s^T] \tag{4.4}$$

be the total moment vector. The total power input $\bar{P}$ is simply the sum of the power inputs from all the primary and secondary patches. That is,

$$\bar{P} = \bar{P}_p + \bar{P}_s \tag{4.5}$$

where $\bar{P}_p$ and $\bar{P}_s$ are the total power inputs from all the primary and secondary patches respectively. The total input power can be expressed as

$$\bar{P} = \frac{1}{2}\text{Re}\{\boldsymbol{M}^H \boldsymbol{P} \boldsymbol{M}\} \tag{4.6}$$

where $\boldsymbol{P}$ is the equivalent rotational mobility matrix. The reader is referred to §B for a detailed derivation of (4.6) and the analytical expression for $\boldsymbol{P}$. $\boldsymbol{P}$ is symmetric due to reciprocity. In this case

$$\bar{P} = \frac{1}{2}\boldsymbol{M}^H \text{Re}\{\boldsymbol{P}\}\boldsymbol{M} = \frac{1}{2}\boldsymbol{M}^H \boldsymbol{S} \boldsymbol{M} \tag{4.7}$$

where $\boldsymbol{S}$ is the real part of $\boldsymbol{P}$. Decomposing into primary and secondary patch components, we get

$$\boldsymbol{M}^T = \{\boldsymbol{M}_p^T \, \boldsymbol{M}_s^T\} \tag{4.8}$$

where $\boldsymbol{M}_p$ and $\boldsymbol{M}_s$ are the complex amplitudes of the primary and secondary patches respectively. Similarly, $\boldsymbol{S}$ can be decomposed as

$$\boldsymbol{S} = \begin{bmatrix} \boldsymbol{S}_{pp} & \boldsymbol{S}_{ps} \\ \boldsymbol{S}_{sp} & \boldsymbol{S}_{ss} \end{bmatrix} \tag{4.9}$$

where $\boldsymbol{S}_{sp} = \boldsymbol{S}_{ps}^T$. Using (4.7), (4.8) and (4.9), we can express the total input power as

$$\bar{P} = \frac{1}{2}[\boldsymbol{M}_p^H \boldsymbol{S}_{pp} \boldsymbol{M}_p + \boldsymbol{M}_p^H \boldsymbol{S}_{ps} \boldsymbol{M}_s + \boldsymbol{M}_s^H \boldsymbol{S}_{sp} \boldsymbol{M}_p + \boldsymbol{M}_s^H \boldsymbol{S}_{ss} \boldsymbol{M}_s] \tag{4.10}$$

Note that $\bar{P}$ is a quadratic function of $\boldsymbol{M}_s$. Minimizing $\bar{P}$ with respect to $\boldsymbol{M}_s$, we get the optimal secondary patch moments are [41]

$$\boldsymbol{M}_s^* = -\boldsymbol{S}_{ss}^{-1} \boldsymbol{S}_{sp} \boldsymbol{M}_p \tag{4.11}$$

The optimal secondary patch moments depend not only on the magnitude and phase of the primary patch moments but also on location of the primary patches with respect to the secondary patches. In general, the primary patch moments are unknown. In what follows, we assume that we know the location of the primary patches. However, we do not know the magnitude and phase of the primary patch moments.

The net input power from the secondary patches is

$$\bar{P}_s = \frac{1}{2}\mathrm{Re}\{\boldsymbol{M}_s^H \boldsymbol{P}_{sp} \boldsymbol{M}_p + \boldsymbol{M}_s^H \boldsymbol{P}_{ss} \boldsymbol{M}_s\} \tag{4.12}$$

Since $\boldsymbol{P}_{ss}$ is symmetric, we get

$$\mathrm{Re}(\boldsymbol{M}_s^H \boldsymbol{P}_{ss} \boldsymbol{M}_s) = \boldsymbol{M}_s^H \mathrm{Re}(\boldsymbol{P}_{ss}) \boldsymbol{M}_s = \boldsymbol{M}_s^H \boldsymbol{S}_{ss} \boldsymbol{M}_s \tag{4.13}$$

Using (4.13) in (4.12), we get

$$\bar{P}_s = \frac{1}{2}\mathrm{Re}\{\boldsymbol{M}_s^H \boldsymbol{P}_{sp} \boldsymbol{M}_p\} + \frac{1}{2} \boldsymbol{M}_s^H \boldsymbol{S}_{ss} \boldsymbol{M}_s \tag{4.14}$$

We consider the following two cases.

Primary patch moments in-phase or 180^o out-of-phase

If the primary moments are in phase (or 180^o out-of-phase), then

$$\boldsymbol{M}_p = \bar{\boldsymbol{M}}_p e^{i\phi} \Rightarrow \boldsymbol{M}_p^H = \bar{\boldsymbol{M}}_p^T e^{-i\phi} \tag{4.15}$$

The real input power from the secondary patches at optimal condition is

$$\begin{aligned}
\bar{P}_s^* &= \frac{1}{2}\mathrm{Re}\{-\boldsymbol{M}_p^H \boldsymbol{S}_{ps}\boldsymbol{S}_{ss}^{-1}\boldsymbol{P}_{sp}\boldsymbol{M}_p\} + \frac{1}{2}\boldsymbol{M}_p^H \boldsymbol{S}_{ps}\boldsymbol{S}_{ss}^{-1}\boldsymbol{S}_{ss}\boldsymbol{S}_{ss}^{-1}\boldsymbol{S}_{sp}\boldsymbol{M}_p \\
&= -\frac{1}{2}\mathrm{Re}\{\bar{\boldsymbol{M}}_p^T \boldsymbol{S}_{ps}\boldsymbol{S}_{ss}^{-1}\boldsymbol{P}_{sp}\bar{\boldsymbol{M}}_p\} + \frac{1}{2}\bar{\boldsymbol{M}}_p^T \boldsymbol{S}_{ps}\boldsymbol{S}_{ss}^{-1}\boldsymbol{S}_{sp}\bar{\boldsymbol{M}}_p \\
&= -\frac{1}{2}\bar{\boldsymbol{M}}_p^T \boldsymbol{S}_{ps}\boldsymbol{S}_{ss}^{-1}\boldsymbol{S}_{sp}\bar{\boldsymbol{M}}_p + \frac{1}{2}\bar{\boldsymbol{M}}_p^T \boldsymbol{S}_{ps}\boldsymbol{S}_{ss}^{-1}\boldsymbol{S}_{sp}\bar{\boldsymbol{M}}_p \\
&= 0
\end{aligned} \tag{4.16}$$

Thus, the real secondary power is zero when the the primary moments are either in-phase or 180^o out-of-phase.

Primary patch moments with arbitrary phases

In this case, the net input power from the secondary patches at optimal condition is

$$\bar{P}_s^* = -\frac{1}{2}\mathrm{Re}\{\boldsymbol{M}_p^H \boldsymbol{S}_{ps}\boldsymbol{S}_{ss}^{-1}\boldsymbol{P}_{sp}\boldsymbol{M}_p\} + \frac{1}{2}\boldsymbol{M}_p^H \boldsymbol{S}_{ps}\boldsymbol{S}_{ss}^{-1}\boldsymbol{S}_{sp}\boldsymbol{M}_p \tag{4.17}$$

Note that $\bar{P}_s^* = 0$ when $\boldsymbol{S}_{ps}\boldsymbol{S}_{ss}^{-1}\boldsymbol{P}_{sp}$ is symmetric. If $\boldsymbol{S}_{ps}\boldsymbol{S}_{ss}^{-1}\boldsymbol{P}_{sp}$ is symmetric, then we have

$$\mathrm{Re}\{\boldsymbol{M}_p^H \boldsymbol{S}_{ps}\boldsymbol{S}_{ss}^{-1}\boldsymbol{P}_{sp}\boldsymbol{M}_p\} = \boldsymbol{M}_p^H \mathrm{Re}\{\boldsymbol{S}_{ps}\boldsymbol{S}_{ss}^{-1}\boldsymbol{P}_{sp}\}\boldsymbol{M}_p$$

which gives

$$\bar{P}_s^* = -\frac{1}{2}\boldsymbol{M}_p^H \mathrm{Re}\{\boldsymbol{S}_{ps}\boldsymbol{S}_{ss}^{-1}\boldsymbol{P}_{sp}\}\boldsymbol{M}_p + \frac{1}{2}\boldsymbol{M}_p^H \boldsymbol{S}_{ps}\boldsymbol{S}_{ss}^{-1}\boldsymbol{S}_{sp}\boldsymbol{M}_p \tag{4.18}$$

$$= -\frac{1}{2}\boldsymbol{M}_p^H \boldsymbol{S}_{ps}\boldsymbol{S}_{ss}^{-1}\boldsymbol{S}_{sp}\boldsymbol{M}_p + \frac{1}{2}\boldsymbol{M}_p^H \boldsymbol{S}_{ps}\boldsymbol{S}_{ss}^{-1}\boldsymbol{S}_{sp}\boldsymbol{M}_p \tag{4.19}$$

$$= 0 \tag{4.20}$$

Now, for $\boldsymbol{S}_{ps}\boldsymbol{S}_{ss}^{-1}\boldsymbol{P}_{sp}$ to be symmetric we need

$$\boldsymbol{S}_{ps}\boldsymbol{S}_{ss}^{-1}\boldsymbol{P}_{sp} = \boldsymbol{P}_{ps}\boldsymbol{S}_{ss}^{-1}\boldsymbol{S}_{sp} \tag{4.21}$$

Using $\boldsymbol{P}_{sp} = \boldsymbol{S}_{sp} + j\boldsymbol{X}_{sp}$, we get

$$\boldsymbol{S}_{ps}\boldsymbol{S}_{ss}^{-1}(\boldsymbol{S}_{sp} + j\boldsymbol{X}_{sp}) = (\boldsymbol{S}_{ps} + j\boldsymbol{X}_{ps})\boldsymbol{S}_{ss}^{-1}\boldsymbol{S}_{sp} \tag{4.22}$$

which gives

$$\boldsymbol{S}_{ps}\boldsymbol{S}_{ss}^{-1}\boldsymbol{X}_{sp} = \boldsymbol{X}_{ps}\boldsymbol{S}_{ss}^{-1}\boldsymbol{S}_{sp} \tag{4.23}$$

Equation (4.23) holds if

$$\boldsymbol{S}_{sp} = \beta\boldsymbol{X}_{sp} \tag{4.24}$$

In order to better understand the above result, consider the case where there are two primary patches and one secondary patch. In this case,

$$\boldsymbol{P}_{sp} = [S_{sp_1} + jX_{sp_1} \quad S_{sp_2} + jX_{sp_2}] \tag{4.25}$$

We get

$$\begin{aligned}
\boldsymbol{S}_{ps}\boldsymbol{S}_{ss}^{-1}\boldsymbol{P}_{sp} &= \frac{1}{S_{ss}}\begin{bmatrix} S_{sp_1} \\ S_{sp_2} \end{bmatrix}[S_{sp_1} + jX_{sp_1} \quad S_{sp_2} + jX_{sp_2}] \\
&= \frac{1}{S_{ss}}\begin{bmatrix} S_{sp_1}^2 + jS_{sp_1}X_{sp_1} & S_{sp_1}S_{sp_2} + jS_{sp_1}X_{sp_2} \\ S_{sp_1}S_{sp_2} + jS_{sp_2}X_{sp_1} & S_{sp_2}^2 + jS_{sp_2}X_{sp_2} \end{bmatrix}
\end{aligned} \tag{4.26}$$

From (4.26), for $\boldsymbol{S}_{ps}\boldsymbol{S}_{ss}^{-1}\boldsymbol{M}_{sp}$ to be symmetric, we get

$$S_{sp_1}X_{sp_2} = S_{sp_2}X_{sp_1} \Rightarrow \frac{S_{sp_1}}{X_{sp_1}} = \frac{S_{sp_2}}{X_{sp_2}} = \beta(\text{say}) \tag{4.27}$$

Equivalently,

$$\begin{aligned}
\boldsymbol{S}_{sp} &= \begin{bmatrix} S_{sp_1} & S_{sp_2} \end{bmatrix} \\
&= \begin{bmatrix} \beta X_{sp_1} & \beta X_{sp_2} \end{bmatrix} \\
&= \beta\boldsymbol{X}_{sp}
\end{aligned} \tag{4.28}$$

Equation (4.28) puts a constraint on the location of the secondary patch with respect to the primary patches in order to have the real secondary power equal to zero. It implies that

$$\psi_{11} = \psi_{12} \tag{4.29}$$

where $\psi_{11} = \arg(P_{sp_1})$ and $\psi_{12} = \arg(P_{sp_2})$. That is, the phase introduced due to the equivalent rotational cross-mobility is the same for both the primary-secondary pairs, $(p_1 - s)$ and $(p_2 - s)$.

4.1.3 Net electrical power in secondary actuator at optimal control

In an actual experiment, the net input (mechanical) power from the secondary patch actuators is hard to measure. Rather, one can easily measure the electrical power by monitoring the voltage and current in the patches. The relation between the net electrical power and the net input power for the i^{th} secondary is given

$$\bar{P}^e_{si} = \frac{1}{2}\frac{\omega\, a^2}{h}|V_{si}|^2\, \bar{\varepsilon}_{33}\delta + \bar{P}_{si} \tag{4.30}$$

where $\bar{P}^e_{si}$ is the net electrical power in the i^{th} secondary patch, $\bar{\mathrm{V}}_{si}$ is the complex amplitude of the voltage applied to the secondary actuator, $\bar{\varepsilon}_{33}$ is the real part of the complex dielectric constant and δ is the loss factor. See §3.4 for detailed derivation of the relation between net input power and net electrical power for a generic PZT patch. Since $\bar{P}_{si} = 0$ at optimal control, equation (4.30) shows that at optimal control, the net electrical power is equal to the dielectric loss in the patch:

$$\bar{P}^e_{si} = \frac{1}{2}\frac{\omega\, a^2}{h}|V_{si}|^2\, \bar{\varepsilon}_{33}\delta \tag{4.31}$$

4.2 Numerical Simulations

Here, we present simulation results for a simply supported plate that is excited by two primary patch actuators and controlled by one or more secondary patch actuators. The effectiveness of MAP control depends not only on the position of the secondary patches with respect to the primary patch actuators but also on the number of secondary patch actuators.

4.2.1 Simulation parameters

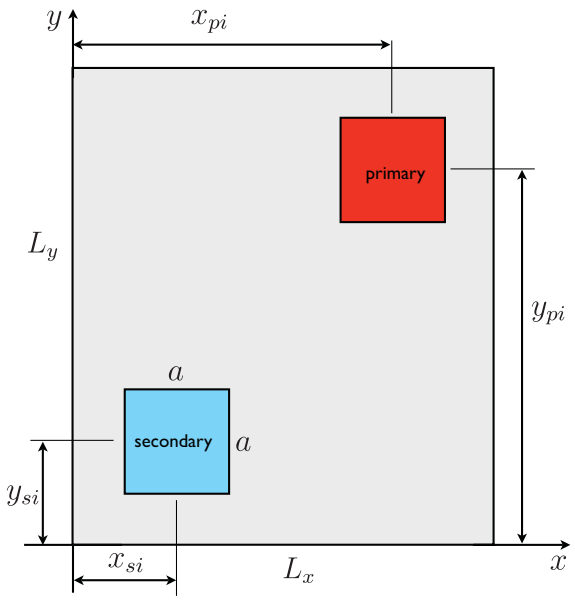

Figure 4.2: Schematic of the plate system for simulation.

A schematic of a simply supported plate system for the simulation studies is shown in Fig. 4.2. For sake of illustration here, one primary and one secondary patch actuators are shown. The coordinates of the i^{th} primary and secondary patch centers are (x_{pi}, y_{pi}) and (x_{si}, y_{si})

respectively. We assume that the plate is made of aluminum. Table 4.1 lists geometrical and material properties for the plate and PZT patches.

Table 4.1: Simulation Parameters.

Variable	Value
L_x	0.38 m
L_y	0.35 m
H	4.2e-3 m
E	70e9 Pa
η	0.01
ρ	2700 kg/m^3
μ	0.33
a	0.05 m
h	0.13e-3 m
Y_{11}	6.6e10 Pa
d_{31}	-190e-12 m/V
$\bar{\varepsilon}_{33}$	1.53e-8 F/m
ν_p	0.35
δ	0.022

4.2.2 MAP Performance as a Function of Location of Secondary Actuators

The primary focus of this study is to evaluate MAP performance as a function of the number and location of secondary actuators for a given set of primary actuators. We assume that the primary patch voltages are either in phase or 180 degrees out of phase. We first consider the plate being excited by two primary patches and controlled by a single secondary patch. Figure 4.3 shows the total power input with and without MAP control for a particular configuration of the primary and secondary actuators. At resonance frequencies, the total power input is proportional to the global vibrational energy. Therefore, minimizing the total power input is equivalent to minimizing the global vibrational energy. The

locations of the primary and secondary actuators are arbitrarily chosen. In this example, $(x_{p1}, y_{p1}) = (0.5L_x/4, 0.5L_y/4)$, $(x_{p2}, y_{p2}) = (3.5L_x/4, 3.5L_y/4)$ and $(x_{s1}, y_{s1}) = (L_x/2, L_y/2)$. The primary patch voltages are $V_{p1} = 10$ V and $V_{p2} = 10$ V. It can be seen that while some of the resonance peaks are attenuated, some are not. This depends on the position of the secondary actuator with respect to the primary actuators. Consider two more cases as shown in Figures 4.4 and 4.5. In Fig. 4.4, $(x_{p1}, y_{p1}) = (2L_x/4, 0.5L_y/4)$, $(x_{p2}, y_{p2}) = (2L_x/4, 3.5L_y/4)$ and $(x_{s1}, y_{s1}) = (L_x/2, L_y/2)$ while in Fig. 4.5, $(x_{p1}, y_{p1}) = (0.5L_x/4, 0.5L_y/4)$, $(x_{p2}, y_{p2}) = (3.5L_x/4, 0.5L_y/4)$ and $(x_{s1}, y_{s1}) = (L_x/2, L_y/2)$. In both cases, $V_{p1} = 10$ V and $V_{p2} = 10$ V. From Fig. 4.4, it can be seen that given the location of the primary actuators, the secondary actuator location is optimal for suppressing all the resonance peaks in the 500-2000 Hz frequency range. However, for the primary actuator locations shown in Fig. 4.5, the location of the secondary actuator is not optimal. Some of the resonance frequencies are attenuated while some are uncontrolled. In general, one may need more than one secondary actuator for improved MAP performance over a broad range of frequencies.

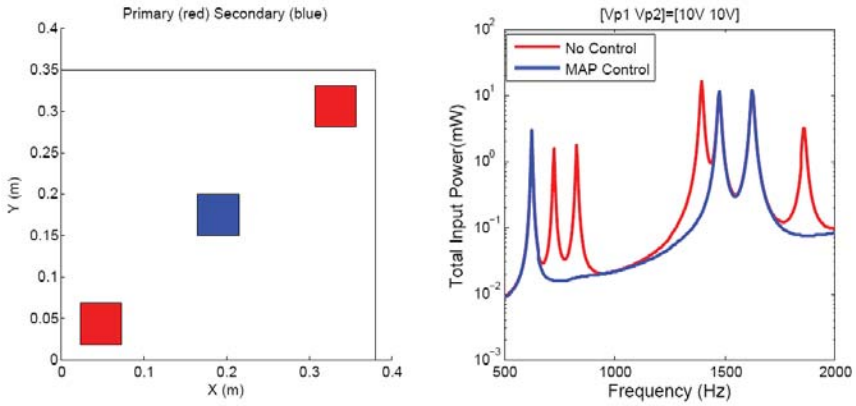

Figure 4.3: Plate excited by two primary (red) actuators and controlled by a single secondary (blue) actuator. Total power input with and without MAP control shown on right.

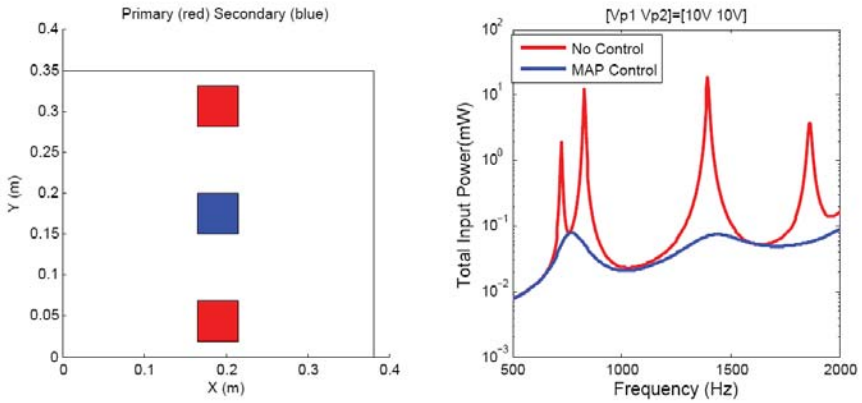

Figure 4.4: Effect of primary actuator locations on MAP control. The secondary actuator location is optimal for suppressing resonance peaks in the 500-2000 Hz frequency range

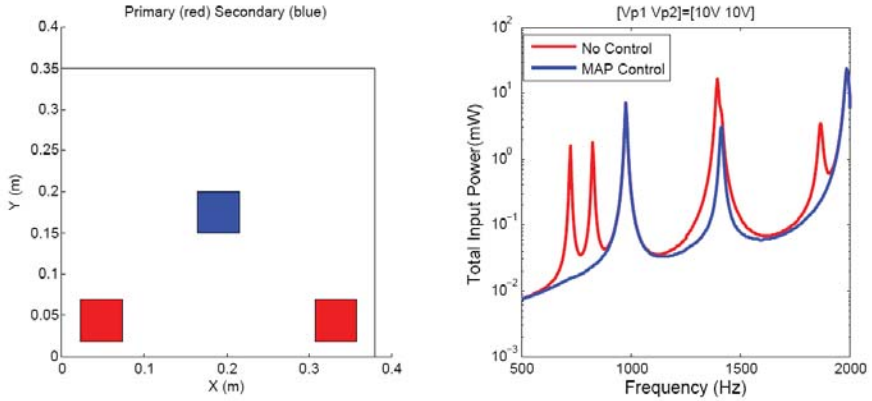

Figure 4.5: Effect of primary actuator locations on MAP control. As the primary actuator locations are varied, the given secondary location is not optimal for suppressing all the resonance peaks in the 500-2000 Hz range.

4.2.3 MAP Performance as a Function of Number of Secondary Actuators

It is expected that MAP performance will improve as the number of secondary actuators is increased. We fix the location of the primary actuators as shown in Fig. 4.5. We start with

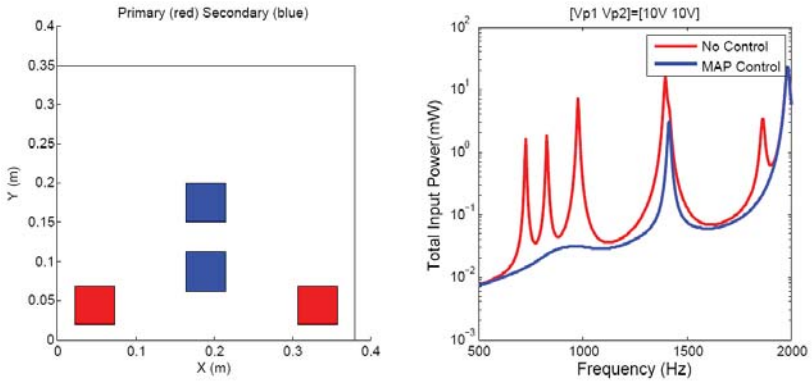

Figure 4.6: MAP control with two secondary patch actuator.

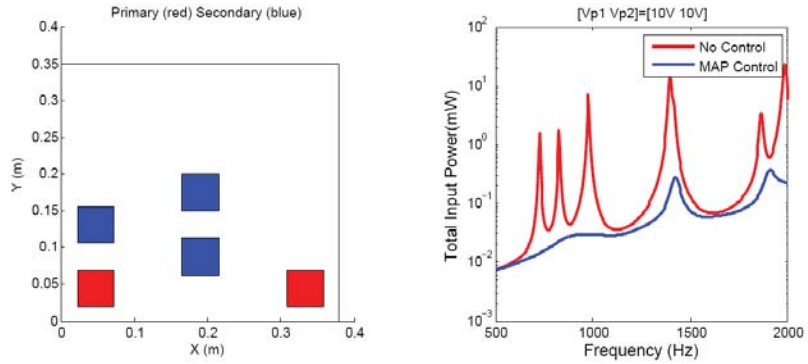

Figure 4.7: MAP control with three secondary patch actuators. Adding one additional secondary actuator improved MAP performance at a given frequency while reducing vibration at other frequencies too.

one secondary actuator and add one extra secondary actuator each time. Figures 4.5-4.7 show the configuration with one, two and three secondary actuators respectively. It can be clearly seen from figures 4.5-4.7 that MAP performance significantly improves as more secondary actuators are added. The resonance frequencies that were not controlled by one secondary actuator, as shown in Fig. 4.5, are effectively controlled by adding more secondary actuators.

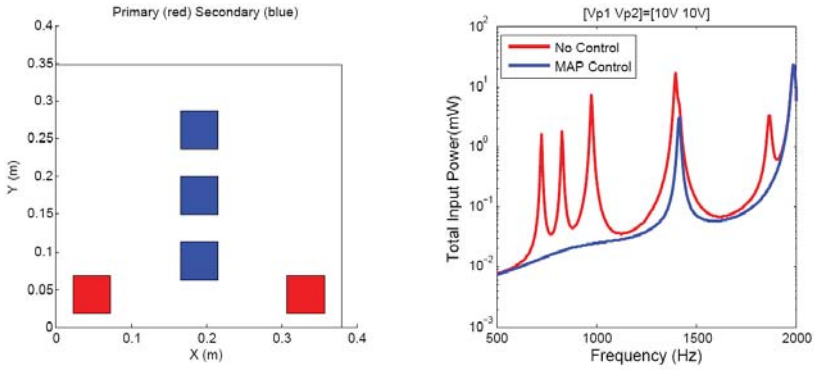

Figure 4.8: MAP control with three secondary patch actuators with a different secondary actuator configuration.

Given a fixed number of secondary actuators, MAP performance will depend on the location of the secondary actuators. Optimal location of the secondary actuators may also depend upon the location of the primary actuators and the frequencies that need to be controlled. This can be seen from Eq. 4.11 that shows the dependence of the optimal secondary moment on the cross angular mobility $\boldsymbol{S}_{sp}$ which depends on the location of the secondary actuators with respect to the primary actuators. This is illustrated by comparing the MAP performance for two different secondary actuator configurations, as shown in Figures 4.7 and 4.8. One of the secondary actuators is moved to a different location. It can be seen that changing the location of one of the secondary actuators in blue made some of the resonance peaks, otherwise controlled, uncontrollable and deteriorated MAP performance. The location of the secondary actuators can be optimized by maximizing the sum of the mode shapes of the frequencies to be controlled.

4.2.4 Secondary Input Power at Optimal Control

When the primary actuators are in phase or 180 degrees out of phase, the total secondary input power is zero at optimal control regardless of location of the secondary actuators. If the primary actuators have arbitrary phase, then the secondary location has to satisfy a

constraint, as given by Eq. 4.29, for the secondary power to be zero at optimal control. Moreover, if there are more than one secondary actuators, then the input power from each secondary actuator is zero at optimal control. This important observation is key to developing a stable iterative algorithm to find the optimal secondary voltages. Note that the stable iterative algorithm can be developed even when the primary actuators have arbitrary phasing. Figure 4.9 shows the input powers from the primary and secondary sources for the actuator configuration shown in Fig. 4.5 at two different excitation frequencies $\omega = 826$ Hz and $\omega =$724 Hz. It can be seen that the total secondary input power (in this case, there is only one secondary actuator) is identically zero when the total input power is minimum. Note that α is a scaling factor defined as $\alpha = V_{si}/V_{si}^*$ for all i where V_{si} is the voltage applied to the i^{th} secondary actuator and V_{si}^* is the optimal value of the i^{th} actuator. Thus, $\alpha = 0$ implies no control whereas $\alpha = 1$ implies optimal control. In this case, $V_{p1} = V_{p2} = 10$ V. $V_{s1}^* = 7.058$ V and $V_{s1}^* = 7.06$ for $\omega = 826$ Hz and $\omega = 724$ Hz respectively.

Figure 4.10 shows the input powers from the primary and secondary sources for the actuator configuration shown in Fig. 4.6 at two different frequencies: $\omega = 800$ Hz (off-resonance) and $\omega =$724 Hz (resonance). Since there are two secondary actuators, we plot the input powers from either actuator along with the total input power and the primary input power. It can be seen that the secondary input power from either actuators is identically zero when the total input power is minimum. In this case, $V_{p1} = 10$ V and $V_{p2} = 5$ V. $(V_{s1}^*, V_{s2}^*) =$ (5.4395, 0.7616) V and $(V_{s1}^*, V_{s2}^*) =$ (4.0181, 1.8153) V for $\omega = 800$ Hz and $\omega = 724$ Hz respectively.

4.2.5 Effect of High Damping on MAP Control

For simplicity, we consider one primary excitation controlled by one secondary patch actuator. We first consider low structural damping with $\eta = 0.01$. Figure 4.11 shows the secondary electrical power, the secondary loss and the total input power as a function of the secondary voltage. The primary voltage is $V_p = 10$ volts and the excitation frequency is $\omega = 620$ Hz. It can be seen that for this case of low damping, the intersection between the secondary electrical power and loss curves is clear and easy to detect.

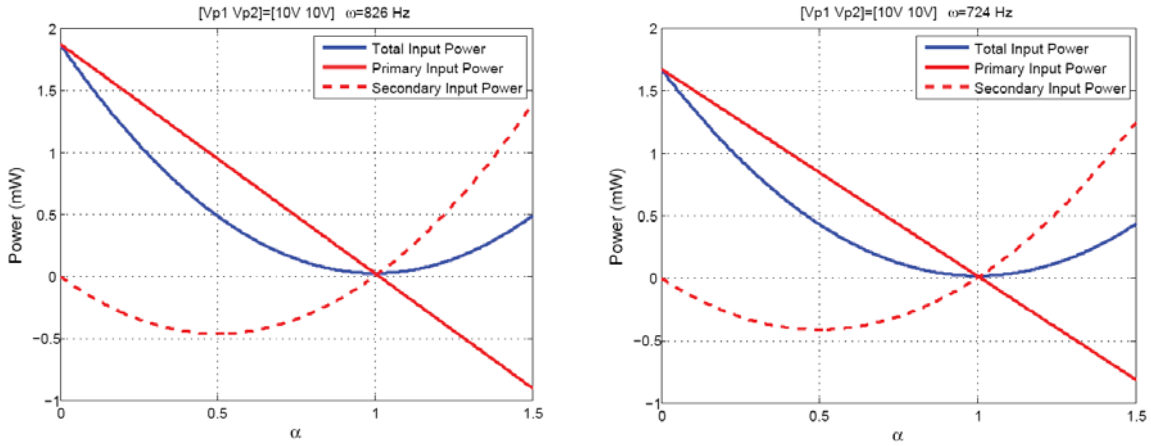

(a) (b)

Figure 4.9: Total, Primary and Secondary Input Powers for the configuration shown in Fig. 4.5. (a) ω = 826 Hz (b) ω=724 Hz.

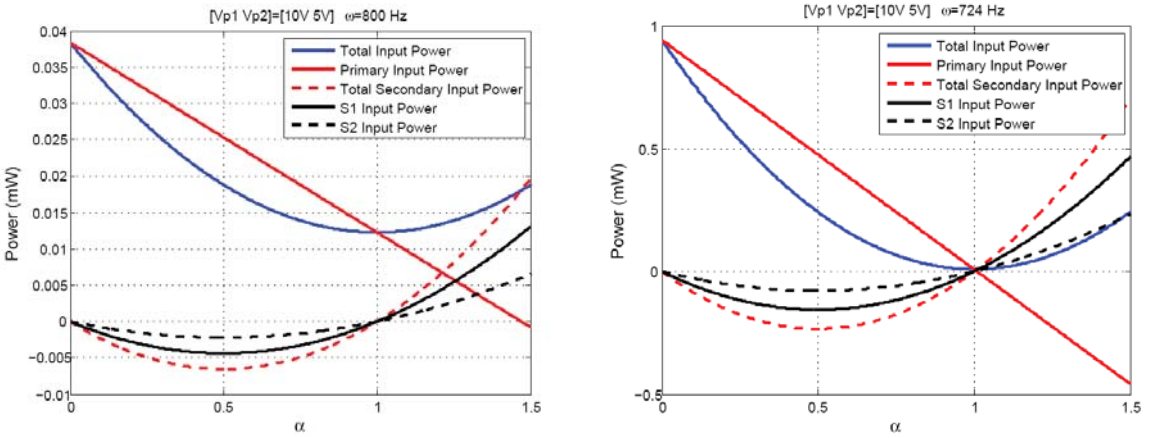

(a) (b)

Figure 4.10: Total, Primary and Secondary Input Powers for the configuration shown in Fig. 4.6. (a) ω = 800 Hz (b) ω=724 Hz.

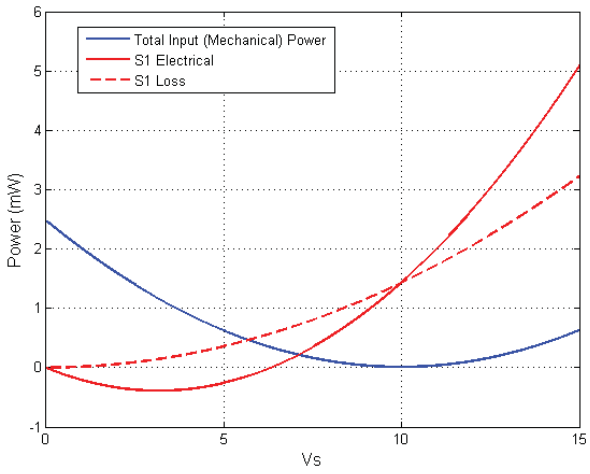

Figure 4.11: Intersection of secondary electrical power and loss with damping equal to 1%. The primary voltage is $V_p = 10$ volts and the excitation frequency $\omega = 620$ Hz.

As damping is increased without increasing the primary excitation level, the secondary electrical power approaches the loss curve. This makes determination of the intersection point difficult. This is illustrated in Fig. 4.12(a) where the damping is artificially increased to 8 %. The primary excitation level was kept at $V_p = 10$ volts. In this case, the primary source is not strong enough to induce the excitation level sensed by the secondary actuator for implementing MAP control. However, if the primary excitation level is increased, enough excitation will be sensed by the secondary actuator. The separation between the secondary electrical and loss curves will increase resulting in a clean intersection. This is illustrated in Fig. 4.12(b) where the primary excitation voltage is increased from 10 volts to 30 volts for the same high damping value of 8%.

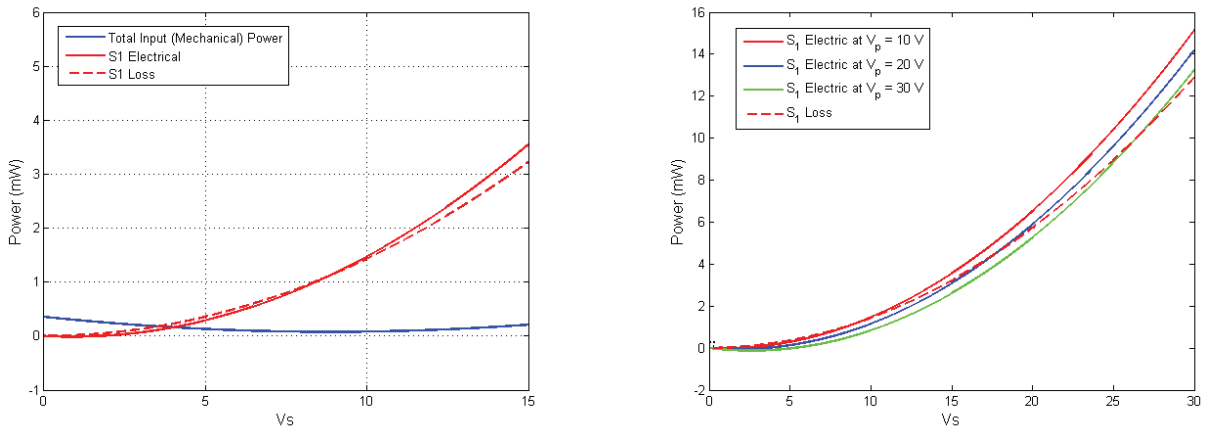

(a) (b)

Figure 4.12: Intersection of secondary electrical power and loss with damping equal to 8%. (a) $V_p = 10$ volts and (b) Increasing values of V_p.

4.3 Experimental Demonstration of MAP Control

This section describes experimental validation of MAP control for multiple primary and secondary actuators. In §4.3.1, we first describe MAP validation using impedance head measurements to demonstrate how the secondary input power is zero when the total input power is minimized. Impedance head measurements allow us to calculate input powers directly. In §4.3.2, the testbed for real-time MAP implementation is described. Finally in §4.3.3, experimental results for MAP control with two primary and two secondary PZT actuators are presented.

4.3.1 MAP verification with Impedance Head Measurements

Minimum actuation power is verified by measuring the actual mechanical powers that are injected into the vibrating structure by primary and secondary sources. This verification

step demonstrates the foundations of MAP without considering piezoelectric actuators or how the mechanical power in the secondary sources is sensed. The mechanical power injected into a structure is easily computed using an impedance head that measures simultaneously acceleration (or velocity) and force according to

$$\Pi = \frac{1}{2}\mathrm{Re}\left(f\dot{x}^*\right) = \frac{1}{2}\mathrm{Re}\left(\frac{fx^*}{j\omega}\right) \tag{4.32}$$

The impedance head at both primary and secondary sources allows for the estimation of the total mechanical power injected into the structure by simple summation of the individual mechanical powers at each source. This assumes most if not all the mechanical power is contained in flexural waves as measured by the impedance heads.

Impedance Head Experimental Setup

Verification of MAP using impedance head was performed on a freely suspended aluminum plate. The plates dimensions were 15.1 inches x 14.9 inches x 0.125 inches. Impedance heads (PCB model 288D01) were mounted onto the structure at both primary and secondary sources. A picture of the test setup is presented in Fig. 4.13. Free-floating shakers injected mechanical power through the impedance heads, and normal to the plate surface. A LabVIEW code measured acceleration and force at all impedance heads and calculated the respective mechanical power. Single frequency excitations were generated and fed to the sources. With a set amplitude and phase of the primary source(s), the phase and amplitude of the secondary source were varied until MAP was achieved. Total mechanical power in the structure was calculated by simple summation of the individual powers of all sources.

Figure 4.13: Plate Instrumented with Impedance Head (shakers not shown).

Results

The measured mechanical power for a single primary and single secondary sources when the secondary phase and amplitude are varied are presented in Fig. 4.14. The primary excitation was at 843Hz, a plate resonant frequency. Locations of the primary and secondary sources ensured both sources coupled well with this structural mode. The global structural power is also presented. Due to the aluminum plates very low damping, the phase of the secondary source is approximately either 0 or 180 degrees out of phase compared to the primary source. In the figure, phase information is contained in the sign of the amplitude voltage, with a negative value representing a 180 phase angle. For this particular source configuration, at MAP, the secondary has is 180 degrees out of phase compared to the primary. As expected, as gain is increased (becomes more negative in this case), the secondary's real power becomes negative before increasing again, becomes 0 where the global power is minimized, and then becomes positive where the total power in the structure increases. This verifies analytical calculations as presented in §4.1.2.

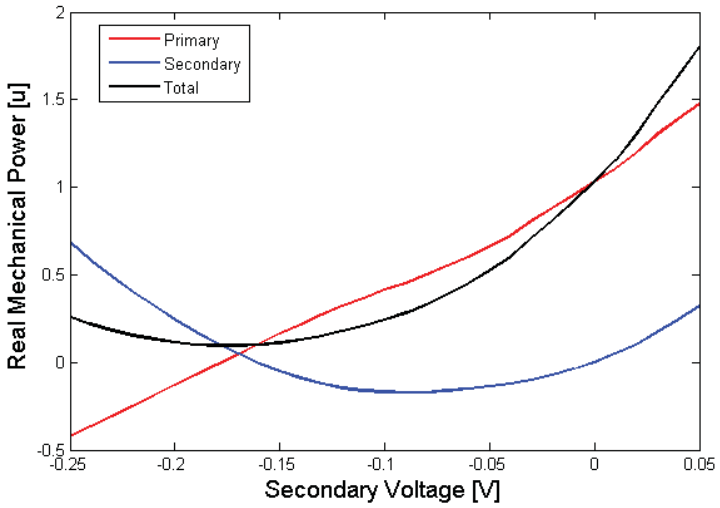

Figure 4.14: Impedance Head Measurements of Real Mechanical Powers.

While impedance heads measured point force and acceleration,the theory also holds for moment excitations. This test setup provides a platform for the simultaneous development of MAP using piezoelectric actuators, a methodology that uses electrical quantities to estimate mechanical power without any impedance heads, and the development of control strategies with multiple primary and secondary sources and using MAP as a control objective.

4.3.2 MAP Testbed and Real-Time Implementation

We have developed control software and an instrument system that enables semiautomatic MAP implementation and allows for testing of various primary and secondary excitation and sensing. In order to implement MAP control to real structures without knowledge of the primary excitation and to facilitate more efficient tests with different configurations, it was considered important to establish a flexible hardware setup and to develop comprehensive software modules that automate the entire procedure. The control software and test system was upgraded to control four actuators simultaneously. Sections 4.3.2 and 4.3.2 contain de-

tailed descriptiosn of two important software modules, a control objective function estimator and a frequency detector. In §4.3.2, integration of the newly developed software modules with the main MAP control software is described in detail.

Determination of Actuator Aggregated Loss

A software module was created to estimate aggregated loss of the secondary actuator including dielectric loss of the PZT and loss due to the residual vibration of the structure left from the control. The software module is shown in Fig. 4.15. This module was developed in LabVIEW and allows users to select voltage and frequency ranges before actuator excitation. The software has two loops, one for voltage sweep and the other for frequency sweep. First, the excitation voltage is fixed to a starting voltage, and the frequency is swept within the specified range. As frequency increases, the real power at each frequency is calculated directly from voltage at a power amplifier and current at a resister connected to the actuator. After this step, voltage is increased and the frequency sweep is repeated. Finally, a raw power loss map is generated and stored as an array variable and sent to a two dimensional regression module for the aggregated loss estimation.

The two dimensional regression module provides curve fitting to the power measurement of the actuator. The embedded algorithm searches for local minima in the measurement which are induced by off-resonance frequencies. Then, interpolation between the fitting points is performed to create a complete control objective function with respect to frequency and voltage. A heavy dependence of material properties and power mismatch were observed in the initial MAP testing. This stimulated the need for mapping out actuator power loss experimentally over the entire range of frequencies and electric field instead of using a simple dielectric loss model. The 2D map is stored as a spread sheet and read when the MAP control is performed.

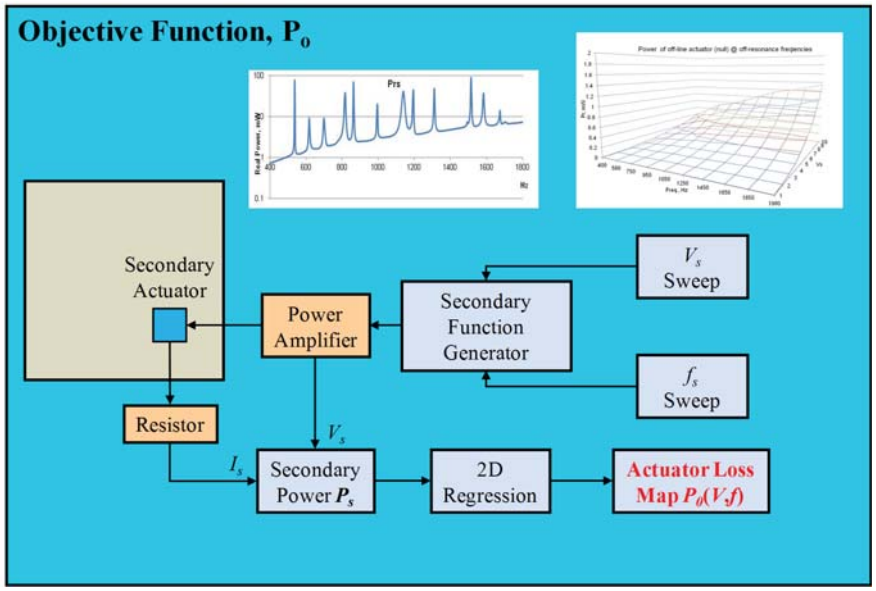

Figure 4.15: Actuator electric loss characterization.

Detection of Frequency and Structural Mobility Phase

A software module was created to use the secondary actuator (control actuator) as a passive sensor to determine frequencies to suppress. In the experimental setup, a primary function generator creates a continuous sinusoidal waveform function with respect to f_p, V_p, and ϕ_p specified by a user. Then, the current through a resistor connected to the PZT is read by a digitizer. A built-in LabVIEW function then computes the Fast Fourier Transform of the current signal to determine dominant frequency components in the signal. The FFT and peak frequency detection thus allow the primary frequency f_p to be determined without using primary actuator information. The frequency of the secondary actuator, f_s, is then set equal to f_p.

The cross mobility phase between the primary and secondary actuators is determined by comparing the phase between V_p and I_s. This is done in the off-line plate characterization prior to the MAP control. It can also be extracted from plate's analytical models. The

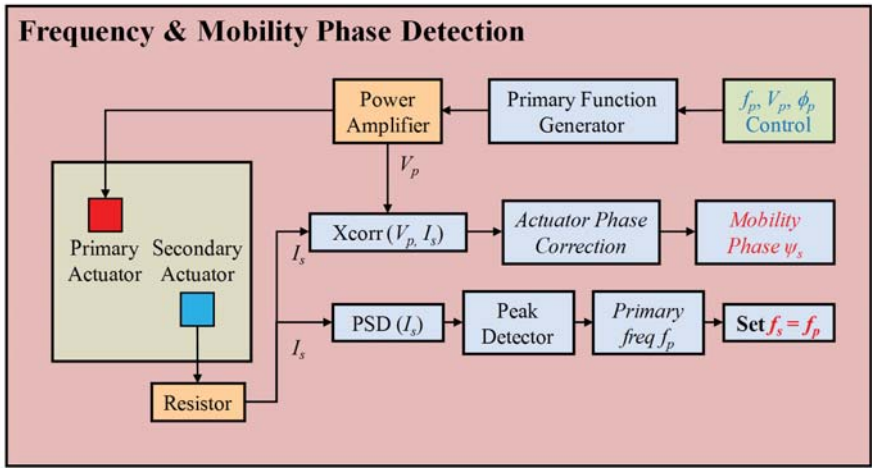

Figure 4.16: Frequency and mobility phase detection for mMAP control.

mobility phase detection technique is empirical and relies on experiments. Note that the cross-correlation function in Fig. 4.16 is also a built-in LabVIEW function that provides the phase at a select frequency between two time domain signals. When piezoelectric transducers are used, the phase of I_s can be changed by $\pi/2$ due to capacitance of the transducers. In this case, an actuator phase correction is needed. f_s and mobility between the primary and the secondary sources are the output of this module to be used for the final MAP control.

MAP control independent of the primary excitation

The experimental process for MAP verification consists of multiple channel signal generation, acquisition and vibration monitoring as shown in Fig. 4.17. The updates to the test setup include: 1) hardware update to enable multi-actuator excitation and sensing, and 2) the development of a software module that incorporates objective function acquisition and frequency detection to real-time MAP control. The overall measurement system has been developed based on LabVIEW 8.6 software that controls an NI PXI chassis. The chassis contains analog to digital converters and waveform generators connected to four audio power amplifiers with line transformers. The real power of each actuator is monitored and recorded

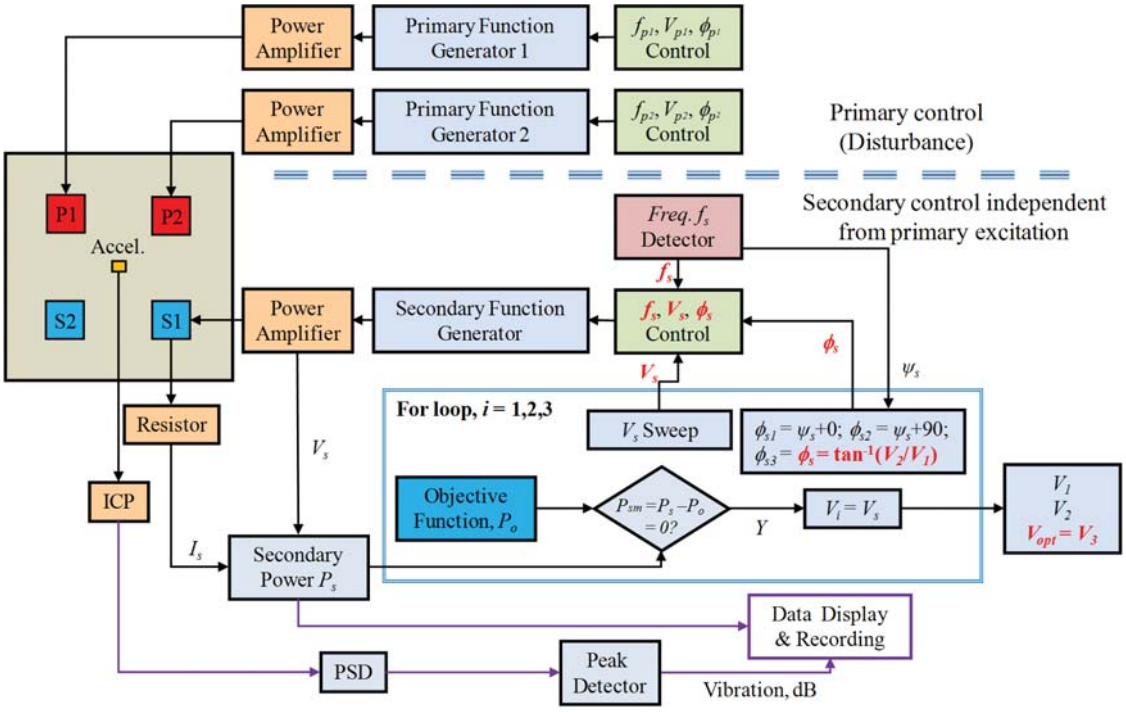

Figure 4.17: Frequency and mobility phase detection for MAP control.

as a function of drive frequency, voltage, and phase with respect to phase reference defined by the primary actuator. The real electric power in the secondary actuator is calculated from the secondary voltage and the current sampled by a precision resistor on the drive circuit. The vibration level of the plate structure is monitored simultaneously by an accelerometer mounted on the plate at a location away from most of the node lines of the modes being analyzed (see Fig. 4.18).

Figure 4.17 illustrates how a secondary actuator is controlled to track the optimal control frequency, phase, and voltage. The objective function for the secondary actuator is the sum of electrical loss and mechanical loss (aggregated loss) as a function of frequency and voltage and is predetermined. A frequency detector analyzes signals measured by the secondary actuator and determines frequency contents of the disturbance in the structure f_s. Then, the software determines optimal phase (ϕ_s) for the secondary actuator. The optimal secondary

voltage is determined at two different secondary phases, ψ_s and $\psi_s + 90$ degrees. The ratio of the two voltage values is used to estimate ϕ_s. Once ϕ_s is determined, the secondary voltage is swept again to find the optimal control voltage. The developed software is designed to conduct frequency, phase and optimal control voltage estimation with a few clicks by users in pursuit of fully automated real-time MAP control.

4.3.3 Experimental Validation of MAP Control with Multiple Excitations

The principle of MAP for single primary (excitation) and single secondary (control) has been experimentally validated and demonstrated via piezoelectric collocated sensor and actuator on a simple metal plate. This year, we have extended MAP control theory to multiple primary excitations and multiple secondary actuators (mMAP) and validated it through the enhanced control software and hardware platform with emphasis on the phase control and optimization. We have also initiated MAP demonstration on a more realistic helicopter structure and with high damping.

Theoretical investigations conducted early in Year 2 identified that: 1) principle of MAP is valid for mMAP and vibration suppression is equally effective if the primary and secondary actuation configuration can meet certain symmetry conditions, 2) MAP control implementation algorithm through gain control (magnitude optimization) on single excitation is also applicable to the multiple excitation, and 3) for a more realistic excitation where arbitrary phasing of the primaries is dominant, the secondary phase optimization becomes an essential and necessary part of mMAP control.

Description of mMAP validation

The experimental setup described in $ 3.5 was used for the mMAP investigation and develop fundamental understanding. To accommodate the mMAP test, two piezoelectric patch actuators are added and the four actuators are now symmetrically located on four corners

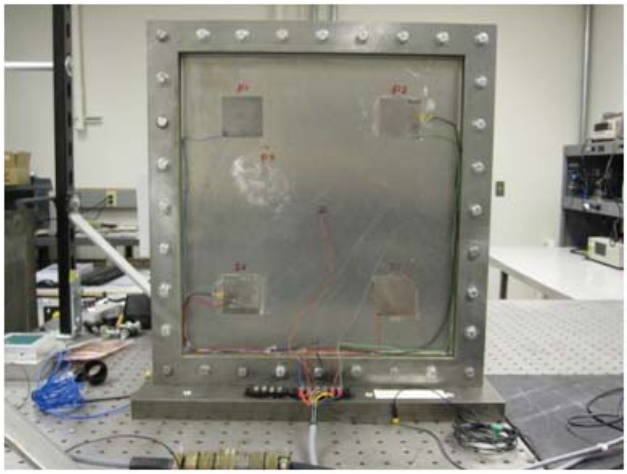

Figure 4.18: The aluminum plate test apparatus with two primary and two secondary actuators.

respectively to meet the nominal symmetry requirement of mMAP control. This placement also facilities flexibility in pairing actuators to form various symmetric and asymmetric configurations, see Fig. 4.18. Also depicted in this figure is the accelerometer used to sense local vibration. The two new actuators (P_2 and S_2) are bonded to the aluminum plate with direct electrodes in back as the common grounding to minimize the impact of the adhesive between the actuators and the plate on the actuator aggregated power loss. This is critical to determining optimal control of the secondary actuators. The dimensions and material properties of the plate and PZT patch are provided in Table 4.2.

The process of mMAP control (with gain only) is similar to the single MAP except that only one variable is swept at a time while the others are kept constant in magnitude and phase. The control objective is the actuator aggregated loss for the two control actuators. These losses are predetermined in the form of a 2D matrix of power loss as a function of frequency and voltage.

In searching for the optimal control voltage of the secondary actuators, the two primary actuators excite the plate with a constant voltage V_p at select frequencies. The voltage of the first secondary actuator, V_{s1}, is swept at a constant frequency while comparing its power

Table 4.2: Geometry and material properties for plate and PZT patch.

Variable	Value
L_x	0.38 m
L_y	0.35 m
H	4.2e-3 m
E	70e9 Pa
η	0.01
ρ	2700 kg/m^3
μ	0.33
a	0.05 m
h	0.13e-3 m
Y_{11}	6.6e10 Pa
d_{31}	-190e-12 m/V
$\bar{\varepsilon}_{33}$	1.53e-8 F/m
ν_p	0.35

to its actuator aggregated loss until P_{s1}, the power in secondary actuator, equals the loss power, at which point vibration should be a minimum. The corresponding voltage V_{s1}^* is the estimated optimal MAP control voltage for the first control actuator. The next step is to excite this secondary actuator at a constant V_{s1}^* while sweeping the voltage input to the second control actuator voltage V_{s2} until P_{s2} equals its aggregated loss at V_{s2}=V_{s2}^*. The vibration of the plate is monitored by an accelerometer in the center of the plate. Applying V_{s1}^* and V_{s2}^* to the control actuators S_1 and S_2, respectively, further reduces the vibration to a new minimum. A few iterations between the two control actuators may be required to converge the control inputs to their global optimal values and further reduce the vibration.

Multiple Primary Excitation with Simple Phases

As the first example, we demonstrate performance of MAP with two primary excitations and two secondary controls on the lightly damped aluminum plate. Figure 4.19 shows the optimum search of the second control actuator with both primary actuators P_1 and P_2 on

and the first control actuator S_1 excited at a fixed V_{s2}^*. With both control actuators at the optimal control, the vibration is reduced by 20 dB.

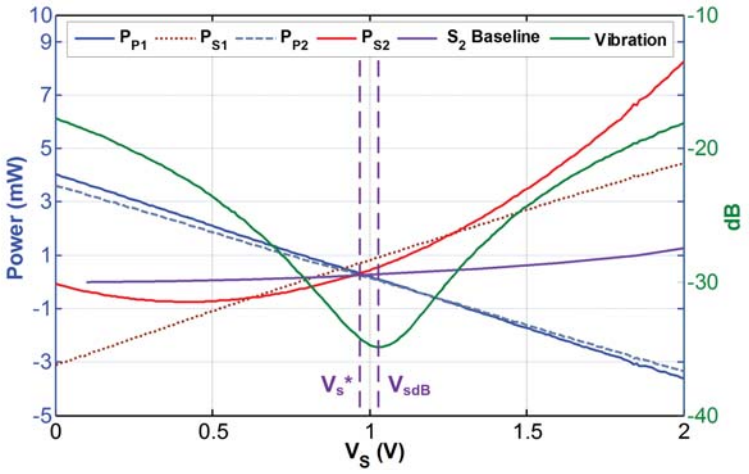

Figure 4.19: Optimum search of mMAP at 1100 Hz mode. The purple vertical dashed lines show MAP control voltage V_s^* (left) and the actual vibration V_{sdB} (right).

In this test, MAP control criterion meets the actual vibration measurement with reasonable agreement, that is, the minimal vibration occurs near the secondary voltage value where secondary power equals the actuator aggregated loss (intersection) and the net power input to the plate is minimum. The phase relation of the excitations is kept very simple. Both secondary actuators are set to 0^o and the phase of the primaries are 180^o. As predicted by the model for low damping and single excitation, mMAP control has demonstrated small sensitivity to the phase of secondary actuation

Multi Excitation with Primary Arbitrary Phases

Unique and distinctive characteristics of mMAP control are fully revealed when arbitrary phasing is imposed on the primary sources. The determination of the optional control now relies on optimizing both the magnitude and phase. The phenomenon of phase dependency

is fully observed in the experimental results shown in Figures 4.20–4.21.

The aluminum plate is excited by both primaries and only one secondary performs the control to illustrate the complex phasing challenge. The MAP optimal control is again indicated by the intersection of the secondary power to its aggregated power loss (zero net power) and the total input power is indicated by the sum of all actuator power. The input to the secondary actuator is swept while the inputs to the two primaries are kept constant. The vibration level is monitored by the accelerometer at the plate center. Several observations can be made from these test results.

Figure 4.20(a) shows that the mMAP computes the optimal control voltage less accurately with two secondary actuators than with a single secondary actuator. In Figure 4.20(a), V_s^* nearly equals V_{sdB} while in Figure 4.19, these two voltages are slightly separated, although in both cases the primary phasings are simply set to zero. Figures 4.20(a)–(b) and 4.21(a) show the radical change of the MAP optimal control with respect to the minimal vibration measurement and the total power input as the primary phasing varies from 0^o to 90^o and the secondary phase is fixed to 180^o. In addition, the vibration level dip near the optimal control is very sharp for zero primary phasing. It gradually flattens out as the primary phasing shifts to 90^o. Similarly, the alignment of minimal input power to the minimal vibration also shifts but at a milder rate.

It is interesting to note that the optimal control V_s^* and the minimal vibration V_{sdb} flips back to a near perfect alignment if 45^o additional phase is imposed to the secondary actuator, as seen in Fig. 4.21(b). Meanwhile, the vibration measurement dip also returns to this original sharpness as the secondary phase is optimal. Note the optimal phase 45^o is half the primary phasing of 90^o.

The phase dependency of mMAP control is quantitatively summarized in Fig. 4.22. We use the ratio of the actual minimal vibration voltage V_{sdb} over the MAP control voltage V_s^* as an indicator of the MAP convergence and plot it as a function of the primary phasing, with unity indicating perfect agreement between the two voltages. The indicator climbs to 2.5 when the primaries are out of phase by 90^o. Setting the phase to 45^o brings the convergence indicator back to 1. These results illustrate that for mMAP control with arbitrary phasing, the secondary phase must be controlled and optimized while for near zero primary phasing,

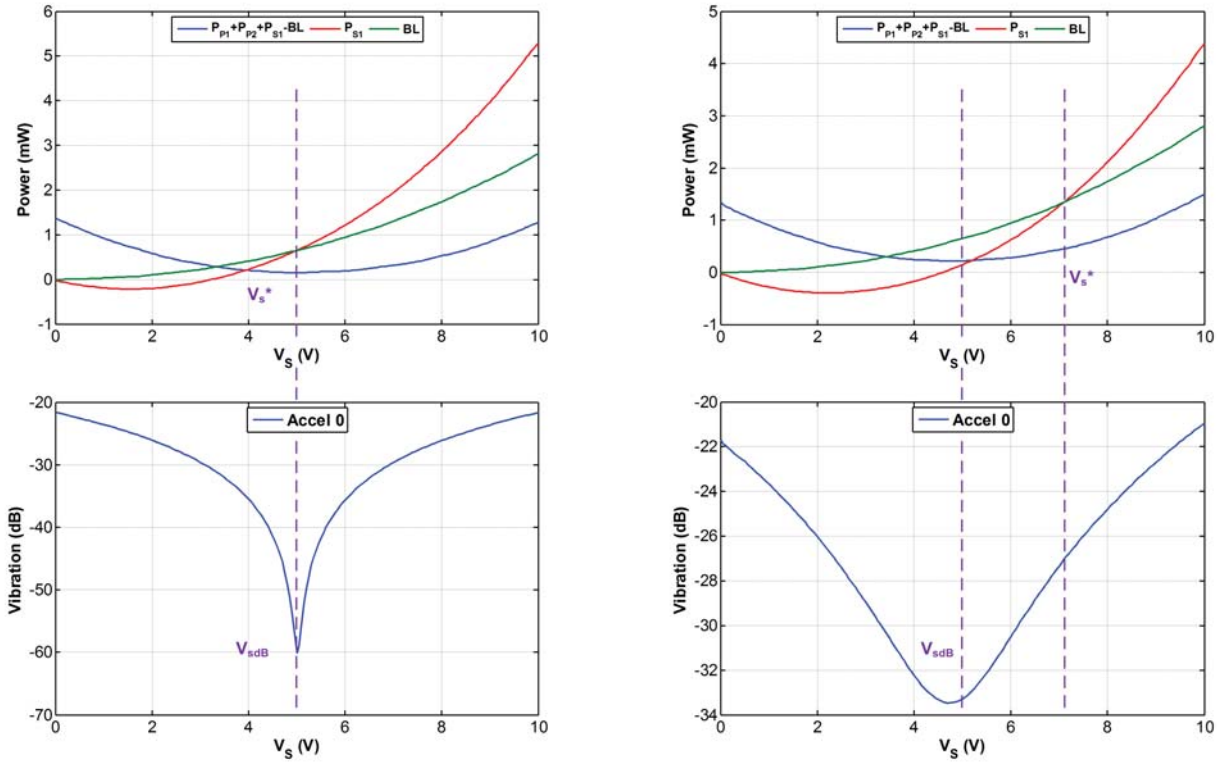

(a) (b)

Figure 4.20: (a) 0 degree primary phasing and (b)30 degree primary phasing. Two dashed vertical lines indicate the minimal vibration and MAP control, respective. $V_{p1} = 0.5$ V, $V_{p2} = 0.5$ V, $f = 1136$ Hz, S_1 phase $= 180^o$.

MAP control can be performed with the secondary phase neglected without a minimal control error.

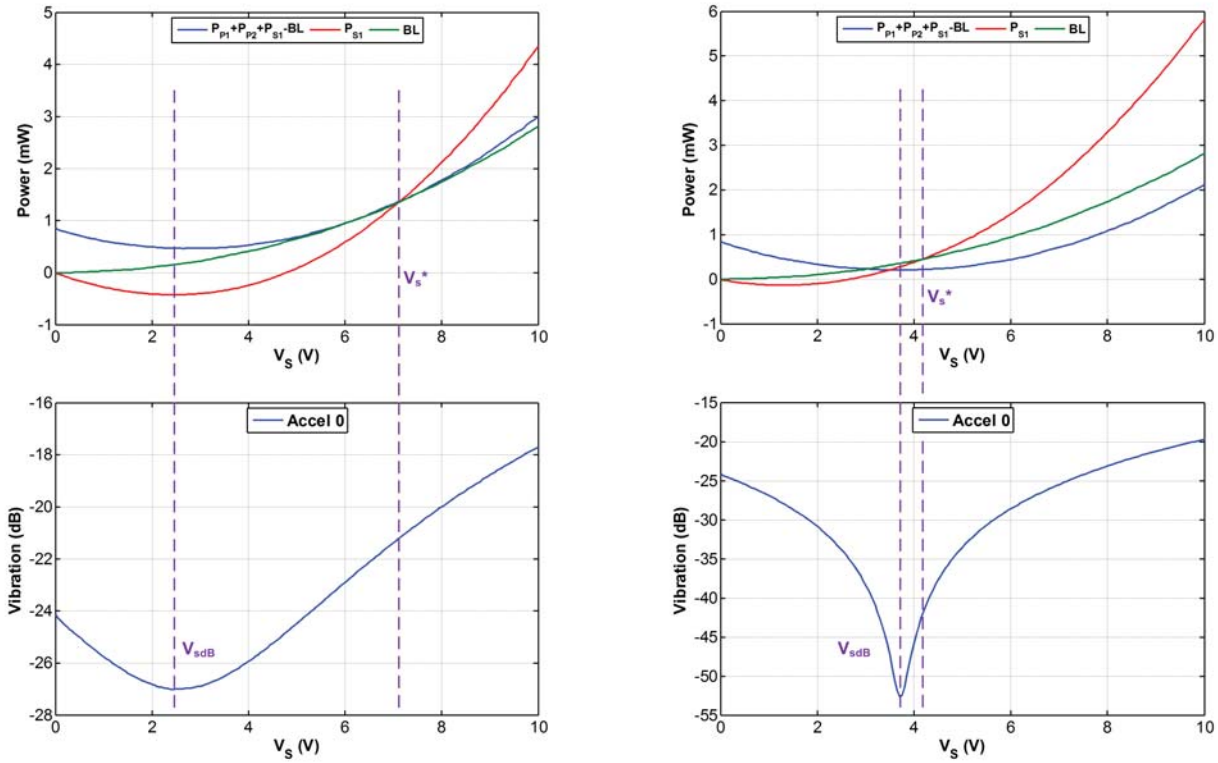

(a) (b)

Figure 4.21: (a) 90 degree primary phasing and S_1 phase = 180^o and (b)90 degree primary phasing with S_1 phase = 225^o. $V_{p1} = 0.5$ V, $V_{p2} = 0.5$ V, $f = 1136$ Hz.

MAP Demonstration on Composite Structure

A composite test rig was instrumented for multiple excitation control and preliminary tests preparation for the real time mMAP demonstration on a more realistic helicopter structure. The composite panel, a mock up of a helicopter fuselage skin, consists of two bays and single plate base panel. The composite panel consists of a panel skin with 6 plies of graphite for a total thickness of 0.045 inches and a Kevlar Core 0.75 inches thick and the weight of the panel is 14.48 lbs. The frequency response function, determined using a tap test, is used to

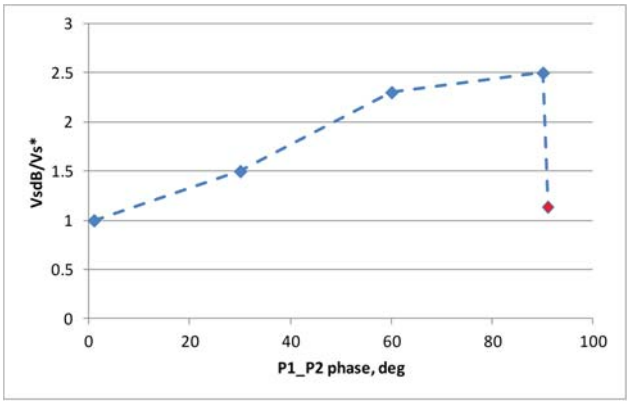

Figure 4.22: Convergence of MAP control vs primary phasing.

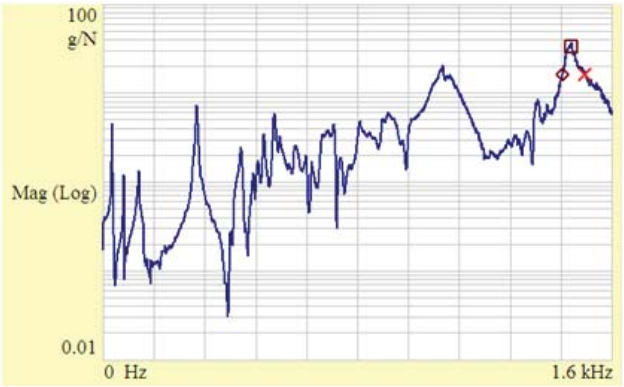

Figure 4.23: Frequency response function for the composite panel.

extract the damping values as shown in Fig. 4.23.

The damping value for different frequencies for the composite panel is given in Table 4.3. Structural damping was extracted using a multi-degree of freedom modal curve fitting technique within the IDEAS software.

Four piezoelectric patch actuator/sensors are mounted on symmetrically about the center of the panel as primary and secondary actuators as shown in Fig. 4.24. The panel is hung from

Table 4.3: Damping versus frequency for the composite panel

$Freq(Hz)$	293	539	874	1068	1473
$\eta\%$	3.0	2.6	4.0	8.9	4.8

Figure 4.24: Composite skin panel with two primary and two secondary piezoelectric patch actuator/sensors mounted.

two bungee cords to simulate a free-free boundary conditions. Actuators are mounted on the panel using an improved electroding method in which the copper foil is directly soldered to the PZT electrode. The actuators are driven by audio amplifiers.

Compared to the aluminum panel tested previously, two distinctive power consumption features are observed. First, the composite panel shows heavier structural damping as high as 10% so that the dynamic range of the electric power (on resonance vs off resonance) of each actuator around a resonance is significantly reduced (much smaller resonance power peaks). Second, the off-resonance power changes by a factor of four from 400 Hz to 1000 Hz, as seen in Fig. 4.25. While both panel damping and the piezoelectric dielectric loss are responsible for this frequency dependence, the former is believed to be dominant as the piezoelectric loss varies by less than 10% (as determined experimentally) in this frequency range. The power spectrum also shows there is very little identifiable modal activity beyond 1000 Hz due to heavy damping.

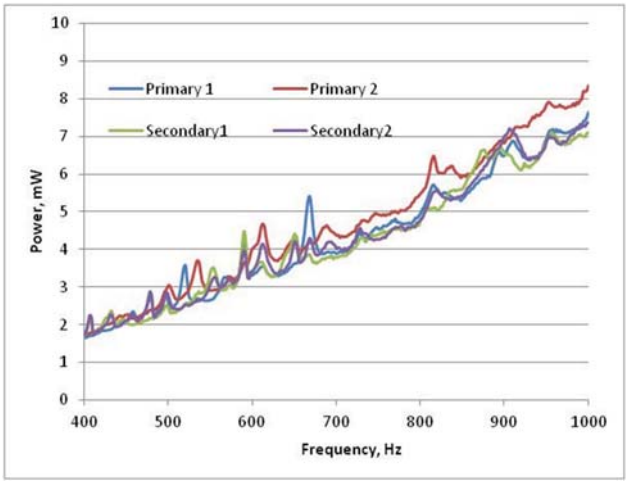

Figure 4.25: Electric power measurement of four actuator-sensor on the composite panel at 10 V.

For MAP control, the high structural damping constitutes a major challenge. Effective sensing and control of vibration by the secondary actuators relies on the structure's transfer mobility which is a function of material damping and structural configuration. The high damping weakens the communication between the primary and secondary. Figure 4.26 analytically shows the effect of the high structural damping on the MAP control. As the damping increases, the secondary actuator power approaches its aggregated loss in shape and value and the intersection of them becomes indistinct. This could result in a large uncertainty in experimental determination of the MAP control point when both the control circuit and aggregated loss have a limited signal to noise ratio.

Nonetheless, to validate the controllability on a high damping structure, we have performed a preliminary MAP test on the composite panel using the single primary and single secondary configuration. Figure 4.27 shows that the vibration reduction is comparable to the low damping case (-12 dB), however, the result agrees with the simulation results. The aggregated loss and secondary power curves run nearly parallel to each other in the figure and the experimental noise creates multiple intersections between these curves. Therefore, detecting the optimal control voltage becomes a challenge.

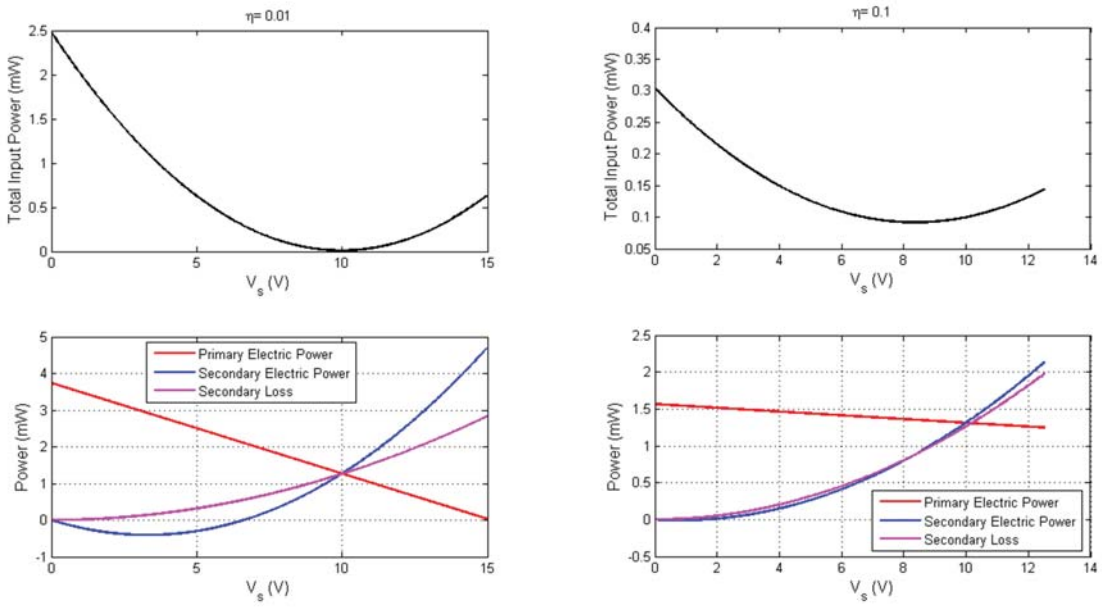

(a) (b)

Figure 4.26: Effect of structural damping on MAP control: (a) low damping 1% (b) composite high damping 10%.

To enhance MAP implementation, two techniques are being sought. One is to increase the primary excitation strength and to force more communication between the primary and secondary. The second technique is to aggressively filter the aggregated loss in order to obtain clean intersections. Figure 4.28 shows an effort to enhance the MAP determination with heavy damping loss. When the primary excitation is doubled, the secondary power P_{s2} is now more negative and the two power curves are more separated compared to the V_p=5 case. However, because of the instrument voltage range limitation, the new intersection between the secondary power and secondary loss cannot be observed. We anticipate that the two curves intersect near 15 V.

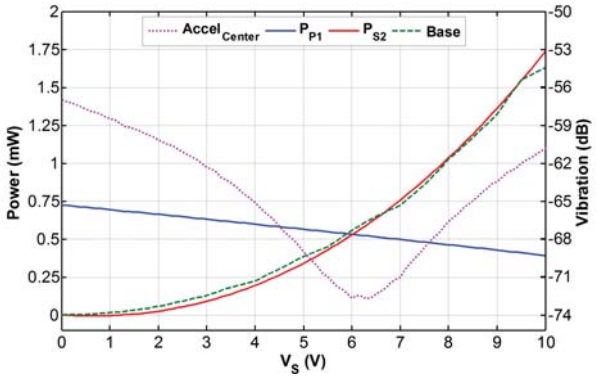

Figure 4.27: MAP control on high damping panel ($V_p = 5$ V, center accel).

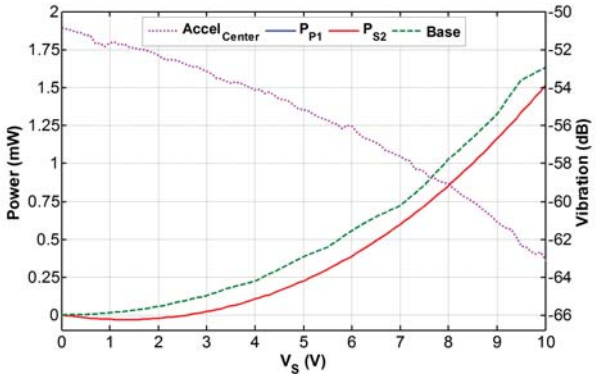

Figure 4.28: Effect of augmented primary excitation on MAP control $V_p = 10$ V, Center Accel. P_{p1} is out of range. Power scale is set to compare with $V_p = 5$ V case.

4.4 Summary

We summarize the key accomplishments presented in this chapter:

- The theory of MAP was extended for multiple primary excitations controlled by multiple secondary excitations.

- The effect of primary phasing on MAP control was investigated. It was shown that when the primary sources have zero relative phasing, the real secondary power is zero at optimal control. However, when the primary sources have arbitrary relative phasing, the secondary real power need not be zero at optimal conditions. Symmetry conditions under which the secondary real power is guaranteed to be zero at optimal control were derived. However, satisfying the symmetry constraints on the secondary locations with respect to the primary sources may be difficult in practice.

- An electro-mechanical model for a simply supported plate excited by multiple primary and multiple secondary PZT patch actuators was developed.

- MAP control with multiple primary and multiple secondary PZT actuators was demonstrated experimentally on a composite panel

Chapter 5

MAP Feasibility for Rotorcraft Vibration Control

In chapter §4, we developed the theory of MAP for multiple primary sources controlled by multiple secondary sources. It was shown that when the phasing between the primary sources is zero, then the secondary real power is zero at optimal control. However, when the primary sources have arbitrary relative phasing, then the secondary real power is not zero. This poses a challenge as MAP control is hard to implement if the secondary real power is not zero at optimal control. Also, when the primary sources have arbitrary phasing, computing the optimal secondary phase is not straight forward. Finally, extending MAP control to multiple secondary sources requires a feasible approach to find the optimal solution especially when the secondary sources are numerous. The main focus of this chapter is to assess the feasibility of MAP control for realistic structures having a distributed primary excitation with arbitrary relative phasing and possibly multiple frequencies controlled by a large number of secondary sources.

5.1 MAP Solution for Arbitrary Primary Phasing

In this section, we present new theoretical results for MAP control implementation for multiple primary sources with completely arbitrary phasing. In §5.1.1, we present the theory for multiple primary sources and one secondary source. We show that placing the secondary actuator at the intersection of the node lines of the neighboring modes, that is, the modes before and after the mode of interest, guarantees that the secondary real power is zero at optimal condition. We also show that the optimal secondary phase and amplitude can be exactly calculated without any knowledge about the primary sources and phasing at resonance and off-resonance frequencies. In §5.1.2, we present numerical simulations to validate the theoretical findings for resonance and off-resonance cases. In §5.1.3, we describe an iterative algorithm to find the optimal secondary sources and prove asymptotic convergence of the algorithm to the optimal solution. However, this approach is not feasible for large number of secondary sources. We present an alternative approach to find the optimal solution for large number of secondary sources.

5.1.1 MAP Solution for Multiple Primary and Single Secondary

Consider a two-dimensional structure that is excited by N primary sources (point forces) $p_1, p_2, \ldots, p_N$. The primary sources are assumed to have arbitrary phasing and given by

$$\boldsymbol{F}_p^T = [F_{p1} \quad F_{p2} \quad \ldots \quad F_{pN}] = [f_{p1}e^{j\phi_{p1}} \quad f_{p2}e^{j\phi_{p2}} \quad \ldots \quad f_{pN}e^{j\phi_{pN}}]$$

where f_{p_i} and ϕ_{p_i} are, respectively, the amplitude and phase of the i^{th} primary source. Assume that the structure is controlled by one secondary source given by

$$F_s = f_s e^{j\phi_s}$$

where f_s and ϕ_s are the amplitude and phase of the secondary excitation. Note that the optimal secondary source is

$$F_s^* = f_s^* e^{j\phi_s^*} = -R_{ss}^{-1}\boldsymbol{R}_{sp}\boldsymbol{F}_p \tag{5.1}$$

where f_s^* and ϕ_s^* are the optimal secondary amplitude and phase, R_{ss} is the real part of the point mobility and $\boldsymbol{R}_{sp}$ is the real part of the transfer mobility $\boldsymbol{M}_{sp}$ given by

$$\boldsymbol{R}_{sp} = \begin{bmatrix} R_{sp_1} & R_{sp_2} & \cdots & R_{sp_N} \end{bmatrix}. \tag{5.2}$$

The MAP condition requires that the optimal secondary solution (f_s^*, ϕ_s^*) lies on the $P_s = 0$ curve where P_s is the real secondary input power. In general, for arbitrary primary phasing, the optimal solution does not lie on the $P_s = 0$ curve. However, we show that optimizing the location of the secondary actuator guarantees that the optimal secondary solution lies on the $P_s = 0$ curve. This is a significant step towards implementation of MAP control technique for realistic excitations.

Consider the transfer mobility between the secondary source and the i^{th} primary source

$$M_{sp_i} = \sum_{n=1}^{\infty} \left(\eta\omega\omega_n^2 + j\omega(\omega_n^2 - \omega^2)\right) \frac{4\phi_n(x_s, y_s)\phi_n(x_{p_i}, y_{p_i})}{m\left[(\omega_n^2 - \omega^2)^2 + \omega_n^4\eta^2\right]} \tag{5.3}$$

where n represents the mode index (n_1, n_2), ω is the excitation frequency, ω_n is the n^{th} resonant frequency, η is the damping, ϕ_n is the n^{th} mode shape, (x_{p_i}, y_{p_i}) is the location of the i^{th} primary and (x_s, y_s) is the secondary location. When ω is close to ω_k, then most of the modal contribution can be assumed to come from the resonant frequencies ω_k, ω_{k-1} and ω_{k+1}. Equation (5.3) can be written as

$$M_{sp_i} \approx \sum_{n=k-1}^{k+1} \left(\eta\omega\omega_n^2 + j\omega(\omega_n^2 - \omega^2)\right) \frac{4\phi_n(x_s, y_s)\phi_n(x_{p_i}, y_{p_i})}{m\left[(\omega_n^2 - \omega^2)^2 + \omega_n^4\eta^2\right]} \tag{5.4}$$

Now, if we choose the location of the secondary source such that it lies on the intersection of the nodal lines of the mode shapes corresponding to ω_{k-1} and ω_{k+1}, then we have

$$\phi_{k-1}(x_s, y_s) = 0 \quad \& \quad \phi_{k+1}(x_s, y_s) = 0 \tag{5.5}$$

Using (5.5) in (5.4), we get

$$M_{sp_i} = \left(\eta\omega\omega_k^2 + j\omega(\omega_k^2 - \omega^2)\right) \frac{4\phi_k(x_s, y_s)\phi_k(x_{p_i}, y_{p_i})}{m\left[(\omega_k^2 - \omega^2)^2 + \omega_k^4\eta^2\right]} \tag{5.6}$$

$$= (a + jb)\delta_{sp_i} \tag{5.7}$$

where

$$a = \eta\omega\omega_k^2, \quad b = \omega(\omega_k^2 - \omega^2), \quad \delta_{sp_i} = \frac{4\phi_k(x_s, y_s)\phi_k(x_{p_i}, y_{p_i})}{m\left[(\omega_k^2 - \omega^2)^2 + \omega_k^4\eta^2\right]} \tag{5.8}$$

Next, we show that given (5.7), the optimal secondary solution lies on the $P_s = 0$ curve. The real secondary power can be expressed as

$$P_s = \frac{1}{2}\mathrm{Re}\left(F_s^H \boldsymbol{M}_{sp}\boldsymbol{F}_p\right) + \frac{1}{2}F_s^H R_{ss}F_s \tag{5.9}$$

where using (5.7), $\boldsymbol{M}_{sp}$ can be expressed as

$$\boldsymbol{M}_{sp} = (a + jb)\begin{bmatrix}\delta_{sp_1} & \delta_{sp_2} & \cdots & \delta_{sp_N}\end{bmatrix} = (a + jb)\boldsymbol{\delta}_{sp} \tag{5.10}$$

which gives

$$\boldsymbol{R}_{sp} = a\begin{bmatrix}\delta_{sp_1} & \delta_{sp_2} & \cdots & \delta_{sp_N}\end{bmatrix} = a\boldsymbol{\delta}_{sp} \tag{5.11}$$

Using (5.1) in (5.9), we get the secondary power at optimal condition as

$$P_s^* = -\frac{1}{2R_{ss}}\mathrm{Re}\left(\boldsymbol{F}_p^H \boldsymbol{R}_{ps}\boldsymbol{M}_{sp}\boldsymbol{F}_p\right) + \frac{1}{2R_{ss}}\boldsymbol{F}_p^H \boldsymbol{R}_{ps}\boldsymbol{R}_{sp}\boldsymbol{F}_p \tag{5.12}$$

Using (5.10) and (5.11), it can be seen that

$$\boldsymbol{R}_{ps}\boldsymbol{M}_{sp} = a(a + jb)\boldsymbol{\delta}_{ps}\boldsymbol{\delta}_{sp} \tag{5.13}$$

is symmetric. Since $\boldsymbol{R}_{ps}\boldsymbol{M}_{sp}$ is symmetric, (5.12) reduces to

$$\begin{aligned} P_s^* &= -\frac{1}{2R_{ss}}\left(\boldsymbol{F}_p^H \boldsymbol{R}_{ps}\boldsymbol{R}_{sp}\boldsymbol{F}_p\right) + \frac{1}{2R_{ss}}\boldsymbol{F}_p^H \boldsymbol{R}_{ps}\boldsymbol{R}_{sp}\boldsymbol{F}_p & (5.14)\\ &= 0 & (5.15)\end{aligned}$$

Thus, the optimal secondary solution lies on the $P_s = 0$ curve. Now, if we know the optimal secondary phase, then the optimal secondary amplitude can be easily calculated by sweeping the secondary amplitude. Next, we show how the secondary optimal phase can be computed.

Note that $\boldsymbol{M}_{sp}$, as given in (5.10), can be expressed as

$$\boldsymbol{M}_{sp} = \begin{bmatrix}\beta_1 & \beta_2 & \cdots & \beta_N\end{bmatrix} e^{j\psi} \tag{5.16}$$

where $\beta_i = \text{mag}((a+jb)\delta_{sp_i}))$ and

$$\psi = \tan^{-1}\frac{b}{a} = \tan^{-1}\frac{(\omega_k^2 - \omega^2)}{\eta\omega_k^2} \tag{5.17}$$

which gives

$$\boldsymbol{R}_{sp} = \begin{bmatrix}\beta_1 & \beta_2 & \cdots & \beta_N\end{bmatrix}\cos\psi \tag{5.18}$$

Using (5.1) and (5.18), the optimal secondary source can be written as

$$f_s^* e^{j\phi_s^*} = \cos\psi \sum_{i=1}^{N} \mu_i e^{j\phi_i} \tag{5.19}$$

where

$$\mu_i = -\frac{\beta_i f_{p_i}}{R_{ss}} \tag{5.20}$$

Rearranging, we get

$$f_s^* = \cos\psi \sum_{i=1}^{N} \mu_i e^{j(\phi_i - \phi_s^*)} \tag{5.21}$$

Since f_s^* is real, setting the imaginary part to zero provides a condition that the optimal phase has to satisfy

$$\sum_{i=1}^{N} \mu_i \sin(\phi_i - \phi_s^*) = 0 \tag{5.22}$$

The real secondary power can be expressed as

$$P_s = \frac{1}{2}R_{ss}f_s^2 + \frac{1}{2}\sum_{i=1}^{N} f_s\beta_i f_{p_i}\cos(\phi_i + \psi - \phi_s) \tag{5.23}$$

Setting $P_s = 0$ and expressing f_s in terms of ϕ_s, we get the equation for the $P_s = 0$ curve

$$\begin{aligned} f_s(\phi_s) &= \sum_{i=1}^{N} -\frac{\beta_i f_{p_i}}{R_{ss}}\cos(\phi_i + \psi - \phi_s) \\ &= \sum_{i=1}^{N} \mu_i \cos(\phi_i + \psi - \phi_s) \end{aligned} \tag{5.24}$$

Differentiating (5.24) with respect to ϕ_s gives

$$\frac{\partial f_s}{\partial \phi_s} = \sum_{i=1}^{N} \mu_i \sin(\phi_i + \psi - \phi_s) \tag{5.25}$$

If $\bar{\phi}_s$ is a solution to the equation

$$\frac{\partial f_s}{\partial \phi_s} = 0 \tag{5.26}$$

then,(5.25) gives

$$\sum_{i=1}^{N} \mu_i \sin(\phi_i + \psi - \bar{\phi}_s) = 0 \tag{5.27}$$

Comparing (5.22) and (5.27), the optimal secondary phase is given by

$$\phi_s^* = \bar{\phi}_s - \psi \quad \text{or} \quad \phi_s^* = \pi + \bar{\phi}_s - \psi \tag{5.28}$$

A special case is $\omega = \omega_k$ (resonance). In this case,

$$\psi = \tan^{-1} \frac{(\omega_k^2 - \omega^2)}{\eta \omega_k^2} = 0 \tag{5.29}$$

which gives the optimal secondary phase as

$$\phi_s^* = \bar{\phi}_s \quad \text{or} \quad \phi_s^* = \pi + \bar{\phi}_s \tag{5.30}$$

The new MAP algorithm for multiple primary sources and one secondary source is summarized:

- Suppose that $\omega \approx \omega_k$. Place the secondary source at the nodal intersection of the mode shapes for ω_{k-1} and ω_{k+1}.
- Find the phase $\bar{\phi}_s$ where the $P_s = 0$ curve is a minimum or a maximum.
- Calculate ψ according to (5.17).
- Calculate the optimal secondary phase ϕ_s^* according to (5.28).
- Set $\phi_s = \phi_s^*$ and sweep f_s till $P_s = 0$ to give the optimal f_s^*.

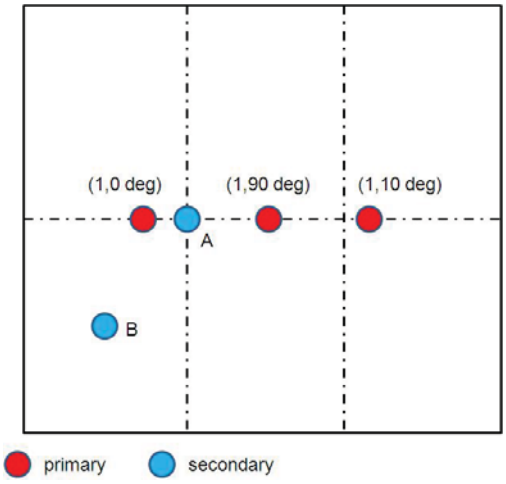

Figure 5.1: Primary source locations shown with corresponding amplitude and phase. Location A corresponds to the optimal secondary location while location B is not optimal

5.1.2 Simulation Results

We consider three primary point excitations with arbitrary phasing and one secondary point excitation acting on the simply-supported aluminum plate previously considered in other simulation studies. The primary sources with the relative phasing are shown in Fig 5.1. We assume that the excitation frequency is close to the resonant frequency of $\omega_k = 826$ Hz. The corresponding mode number is (1,3). Note that the neighboring frequencies are $\omega_{k-1} = 724$ Hz with mode number (3,1) and $\omega_{k+1} = 976$ Hz with mode number (3,2). Therefore, according to the theory, the optimal secondary location is at the intersection of the nodal lines for modes (3,1) and (3,2) as shown by location A in Figure 1. Location B shows a non-optimal secondary location. We consider three cases: (1) $\omega = 826$ Hz (resonance), (2) $\omega = 800$ Hz (off-resonance and left of 826 Hz) and $\omega = 850$ Hz (off-resonance and right of 826 Hz).

Figure 5.2 shows the simulation for resonance case where $P_s = 0$ line is plotted in the $f_s - \phi_s$ space. The contour lines for the total input power are superimposed. In Figure 5.2(a), it can be seen that the turning point of $P_s = 0$ curve (equivalent to minimum or maximum points

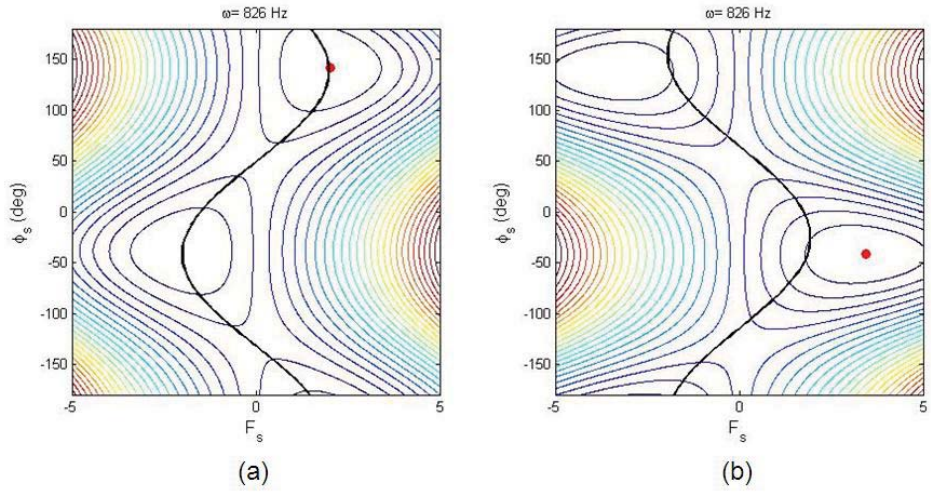

Figure 5.2: Resonance case $\omega = 826$ Hz. The $P_s = 0$ line is shown in dark. The contour lines for the total input power are superimposed. (a) Secondary located at A (b) Secondary located at B

when phase is plotted on the x-axis) corresponds to the optimal secondary shown in red, as suggested by the theoretical results. As expected, the total input power is minimized at the optimal condition. Figure 5.2(b) shows the simulation for the non-optimal location. It can be seen that the optimal solution (shown in red) does not lie on the $P_s = 0$ curve.

Figures (5.3) and (5.4) show the simulation for the off-resonance cases. The calculated optimal phase is indicated by the blue line. The intersection of the blue line with the $P_s = 0$ curve gives the estimated optimal secondary source which is close to the true optimal given by the red dot.

Next, we try to understand the trade-offs between total power attenuation and MAP implementation based on optimal secondary location with respect to the mode shapes. We consider a simply supported plate that is excited by 8 primary sources (point forces) along the edges as shown in Fig 5.5. The primary locations are indicated by red dots. The relative strength and phasing between the primary sources is arbitrary. For the simulations, we chose the primary sources to have the same amplitude but different phasing. Specifically, the phas-

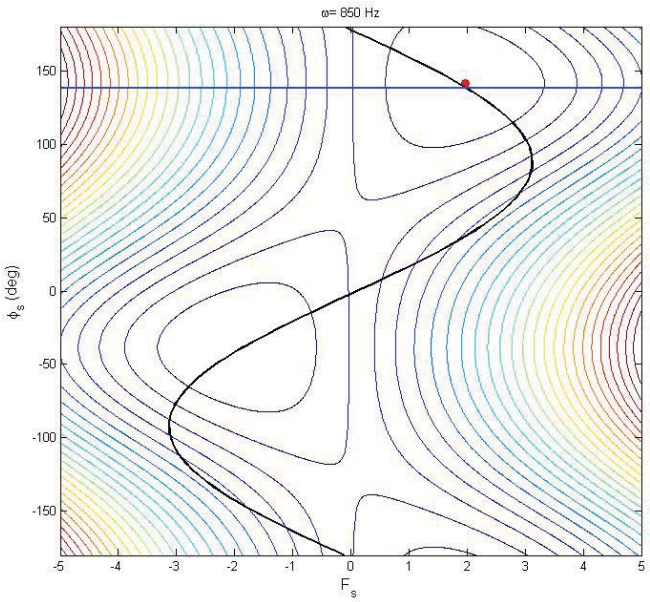

Figure 5.3: Off-resonance case $\omega = 850$ Hz. The $P_s = 0$ line is shown in dark. The contour lines for the total input power are superimposed.

ing was p = [0, 45, 30, 20, -30, -30, -60, 120] degrees with the ordering starting from bottom left and moving counter-clockwise. We consider off-resonance excitation frequency of 800 Hz which is close to the resonant frequency of 826 Hz. The secondary source location is varied in the interior of the plate and the optimal control is applied at each location assuming that the primary sources are known. The total power attenuation $P_{red} = (P_{nc} - P_c)/P_{nc}$, where P_{nc} is the total input power without any control and P_c is the input power with optimal control, is plotted. Note that P_{red}=1 for no control and P_{red}=0 for complete control. We compare the power attenuation at two different locations. Location A is optimal with respect to the mode shapes adjacent to 826 Hz. Location B is the plate center and hot spot for 826 Hz. It can be seen that the power attenuation at A is close to the maximum attenuation you can get. If one uses location B for the secondary, then we will get good power attenuation in the ideal case where the primary sources are known. However, for MAP control we rely only on the secondary power for control. Fig 5.6 shows the variation of the real secondary power at optimal control.

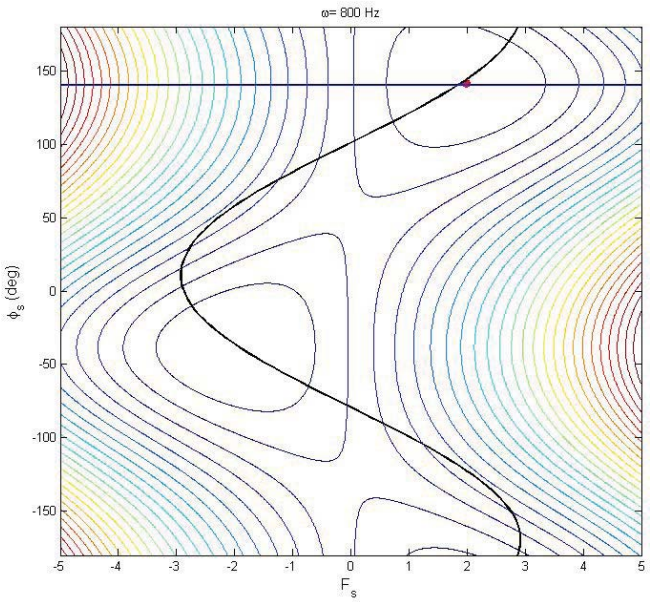

Figure 5.4: Off-resonance case $\omega = 800$ Hz. The $P_s = 0$ line is shown in dark. The contour lines for the total input power are superimposed.

It can be seen that the secondary real power at A is zero, as predicted by the theory, and hence MAP control can be implemented. However, at location B, the secondary real power is not close to zero and therefore MAP control is not suitable even though the attenuation is very good at B.

5.1.3 MAP Solution for Multiple Primary and Multiple Secondary Sources

In §5.1.1, we presented an algorithm to find the optimal secondary source when multiple primary sources with arbitrary phasing are present. Given that we know the optimal solution for one secondary source, we present two approaches to find the MAP solution for multiple

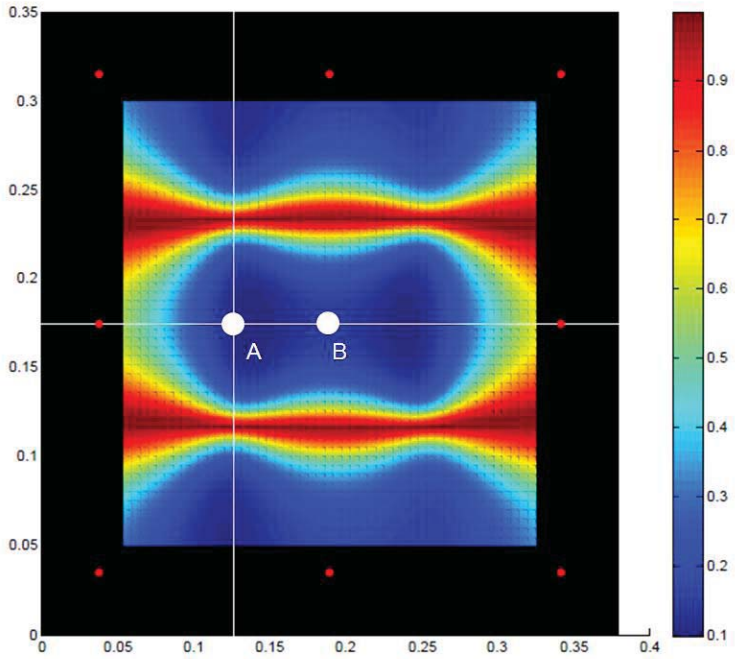

Figure 5.5: Simply supported plate excited by 8 primary sources with excitation frequency equal to 800 Hz. The total power attenuation is shown as a function of the secondary location. Location A shows the optimal location of secondary with respect to the neighboring mode shapes. Location B is plate center and hot spot for the mode at 826 Hz.

secondary sources. We first present an iterative algorithm to find the optimal secondary sources when multiple secondary sources are used for MAP control. We show that the iterative algorithm is asymptotically stable and converges to the optimal value. The iterative solution, however, is not feasible for large number of secondary sources. We present an alternative approach that is feasible for large number of secondary sources and more useful in practice.

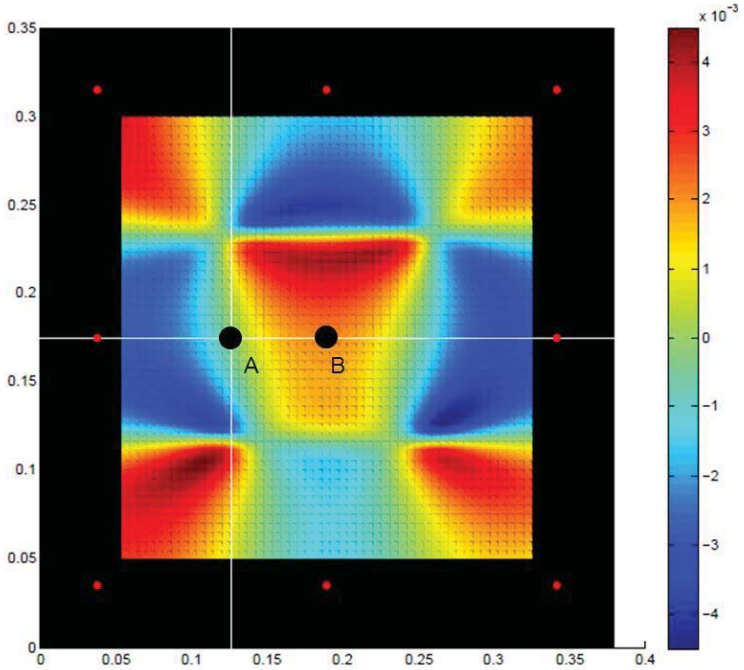

Figure 5.6: Simply supported plate excited by 8 primary sources with excitation frequency equal to 800 Hz. The real secondary power is shown as a function of the secondary location.

Iterative Algorithm

Without loss of generality, consider N primary sources (point forces) $p_1, p_2, \ldots, p_N$ with arbitrary phasing

$$\boldsymbol{F}_p^T = [F_{p1} \quad F_{p2} \quad \ldots \quad F_{pN}] = [f_{p1}e^{j\phi_{p1}} \quad f_{p2}e^{j\phi_{p2}} \quad \ldots \quad f_{pN}e^{j\phi_{pN}}] \tag{5.31}$$

For purposes of illustration, we consider two secondary sources s_1 and s_2 given by

$$\boldsymbol{F}_s^T = [F_{s1} \quad F_{s2}] = [f_{s1}e^{j\phi_{s1}} \quad f_{s2}e^{j\phi_{s2}}] \tag{5.32}$$

Recall that the optimal secondary sources are given by

$$\boldsymbol{F}_s^* = -\boldsymbol{R}_{ss}^{-1}\boldsymbol{R}_{sp}\boldsymbol{F}_p \tag{5.33}$$

where the point and cross-mobility $\boldsymbol{R}_{ss}$ and $\boldsymbol{R}_{sp}$ are given by

$$\boldsymbol{R}_{ss} = \begin{bmatrix} R_{s_1s_1} & R_{s_1s_2} \\ R_{s_2s_1} & R_{s_2s_2} \end{bmatrix} \tag{5.34}$$

and

$$\boldsymbol{R}_{sp} = \begin{bmatrix} R_{s_1p_1} & R_{s_1p_2} & \cdots & R_{s_1p_N} \\ R_{s_2p_1} & R_{s_2p_2} & \cdots & R_{s_2p_N} \end{bmatrix} = \begin{bmatrix} \boldsymbol{R}_{s_1p} \\ \boldsymbol{R}_{s_2p} \end{bmatrix} \tag{5.35}$$

The iterative algorithm is as follows:

1. Assuming only s_1 to be active, find the optimal $F^o_{s_1}$.
2. Fix s_1 to be $F^0_{s_1}$ and find the optimal s_2, $F^0_{s_2}$, by treating s_1 as a primary source.
3. Fix s_2 to be $F^0_{s_2}$ and find the optimal s_1, $F^1_{s_1}$, by treating s_2 as a primary source.
4. Fix s_1 to be $F^1_{s_1}$ and find the optimal s_2, $F^1_{s_2}$, by treating s_1 as a primary source.
5. Repeat the iteration procedure till $|F^{k+1}_{s_i} - F^k_{s_i}| \leq \epsilon$ where $i = 1, 2$ and ϵ is some convergence metric.

The iterative procedure can be represented as a map:

$$F^k_{s_i} \rightarrow F^{k+1}_{s_i} \tag{5.36}$$

for $i = 1, 2$. Next, we show that the iterative map given in Eq. 5.36 is asymptotically stable and converges to the true optimal value given in Eq 5.33.

Stability of the Iterative Algorithm

Assuming s_1 only, the optimal value of s_1 is given by

$$F^0_{s_1} = -\frac{\boldsymbol{R}_{s_1p}\boldsymbol{F}_p}{R_{s_1s_1}} = \alpha_1 \quad \text{(say)} \tag{5.37}$$

Treating s_1 as a primary source equal to $F^0_{s_1}$, we get the optimal s_2 as

$$F^0_{s_2} = -\frac{\boldsymbol{R}_{s_2 p}}{R_{s_2 s_2}}\boldsymbol{F}_p - \frac{R_{s_1 s_2}}{R_{s_2 s_2}}F^0_{s_1} = \alpha_2 + \beta_2 F^0_{s_1} \tag{5.38}$$

Treating s_2 as a primary source equal to $F^0_{s_2}$, we get the optimal s_1 as

$$\begin{aligned} F^1_{s_1} &= \alpha_1 - \frac{R_{s_1 s_2}}{R_{s_1 s_1}}F^0_{s_2} \\ &= \alpha_1 + \beta_1 F^0_{s_2} \end{aligned} \tag{5.39}$$

Using (5.38) in (5.39), we get

$$F^1_{s_1} = \alpha_1 + \beta_1\alpha_2 + \beta_1\beta_2 F^0_{s_1} \tag{5.40}$$

Similarly, $F^1_{s_2}$ can be expressed as

$$F^1_{s_2} = \alpha_2 + \beta_2\alpha_1 + \beta_1\beta_2 F^0_{s_2} \tag{5.41}$$

From (5.40) and (5.41), in general, we have the following iterative map:

$$\begin{aligned} F^{k+1}_{s_1} &= \alpha_1 + \beta_1\alpha_2 + \beta_1\beta_2 F^k_{s_1} \\ F^{k+1}_{s_2} &= \alpha_2 + \beta_2\alpha_1 + \beta_1\beta_2 F^k_{s_2} \end{aligned} \tag{5.42}$$

Next, we show that the steady state solution of the iterative map given in (5.42) corresponds to the true optimal solution. From (5.42), the steady state solution satisfies

$$\begin{aligned} F^*_{s_1} &= \alpha_1 + \beta_1\alpha_2 + \beta_1\beta_2 F^*_{s_1} \\ F^*_{s_2} &= \alpha_2 + \beta_2\alpha_1 + \beta_1\beta_2 F^*_{s_2} \end{aligned} \tag{5.43}$$

which gives

$$\begin{aligned} F^*_{s_1} &= \frac{1}{1-\beta_1\beta_2}\left(\alpha_1 + \beta_1\alpha_2\right) \\ F^*_{s_2} &= \frac{1}{1-\beta_1\beta_2}\left(\alpha_2 + \beta_2\alpha_1\right) \end{aligned} \tag{5.44}$$

Using expressions for $\alpha_1, \alpha_2, \beta_1$ and β_2, we get

$$\begin{aligned} \boldsymbol{F}_s^* = \begin{bmatrix} F_{s_1}^* \\ F_{s_2}^* \end{bmatrix} &= -\frac{1}{R_{s_1s_1}R_{s_2s_2} - R_{s_1s_2}^2} \begin{bmatrix} R_{s_2s_2} & -R_{s_1s_2} \\ -R_{s_1s_2} & R_{s_1s_1} \end{bmatrix} \boldsymbol{R}_{sp}\boldsymbol{F}_p \\ &= -\boldsymbol{R}_{ss}^{-1}\boldsymbol{R}_{sp}\boldsymbol{F}_p \end{aligned} \tag{5.45}$$

which shows that the equilibrium point of the iterative map is the optimal secondary source distribution. Next, we show that the iterative scheme is asymptotically stable. Consider the map for F_{s_1}

$$F_{s_1}^{k+1} = \alpha_1 + \beta_1\alpha_2 + \beta_1\beta_2 F_{s_1}^k$$

The map is linear and the eigenvalue is $\lambda = \beta_1\beta_2$. Asymptotic stability is guaranteed if $\lambda < 1$. Therefore, we need

$$\beta_1\beta_2 = \frac{R_{s_1s_2}^2}{R_{s_1s_1}R_{s_2s_2}} < 1$$

Since $\boldsymbol{R}_{ss}$ is positive definite, we have

$$R_{s_1s_1}R_{s_2s_2} - R_{s_1s_2}^2 > 0 \Rightarrow \frac{R_{s_1s_2}^2}{R_{s_1s_1}R_{s_2s_2}} < 1$$

which guarantees asymptotic stability.

Alternative Solution for Multiple Secondary Sources

The iterative approach presented in the previous section is not feasible for large number of secondary sources. For large number of secondary sources, we need a more practical solution. In what follows, we present an alternative approach that is feasible when the secondary sources are large in number. Since the location of the secondary sources in known, we assume we can compute $\boldsymbol{R}_{ss}$ experimentally before running MAP control. Recall that the optimal secondary sources are

$$\boldsymbol{F}_s^* = -\boldsymbol{R}_{ss}^{-1}\boldsymbol{R}_{sp}\boldsymbol{F}_p \tag{5.46}$$

Note that we assume $\boldsymbol{R}_{ss}$ is known. However, $\boldsymbol{R}_{sp}\boldsymbol{F}_p$ is not known. First, compute the optimal secondary sources one at a time. That is,

$$\hat{F}_{s_j} = -\frac{1}{R_{s_j s_j}} \boldsymbol{R}_{s_j p} \boldsymbol{F}_p \quad \forall \quad j = 1, 2, \ldots, m \tag{5.47}$$

Writing (5.47) compactly, we get

$$\hat{\boldsymbol{F}}_s = -\text{diag}(\boldsymbol{R}_{ss})^{-1} \boldsymbol{R}_{sp} \boldsymbol{F}_p \tag{5.48}$$

where

$$\hat{\boldsymbol{F}}_s^T = [\hat{F}_{s_1} \quad \hat{F}_{s_2} \quad \ldots \quad \hat{F}_{s_m}]$$

Equation (5.48) can be re-written as

$$\boldsymbol{R}_{sp} \boldsymbol{F}_p = -\text{diag}(\boldsymbol{R}_{ss}) \hat{\boldsymbol{F}}_s \tag{5.49}$$

Using (5.49) in (5.46), we get the optimal secondary sources as

$$\boldsymbol{F}_s^* = \boldsymbol{R}_{ss}^{-1} \text{diag}(\boldsymbol{R}_{ss}) \hat{\boldsymbol{F}}_s \tag{5.50}$$

Thus, for m secondary sources, one needs to run MAP test m times to calculate the optimal secondary sources.

5.1.4 FEM Model

A FEM model was built to verify MAP control authority and global vibration reduction and also guide the experimental test rig design and validation. The design consists of a thin aluminum plate riveted to rigid aluminum angles and is representative of a realistic airframe structure. Point force or line moment excitations were applied to the angles as primary excitation. The force amplitude and phase of a secondary point force excitation

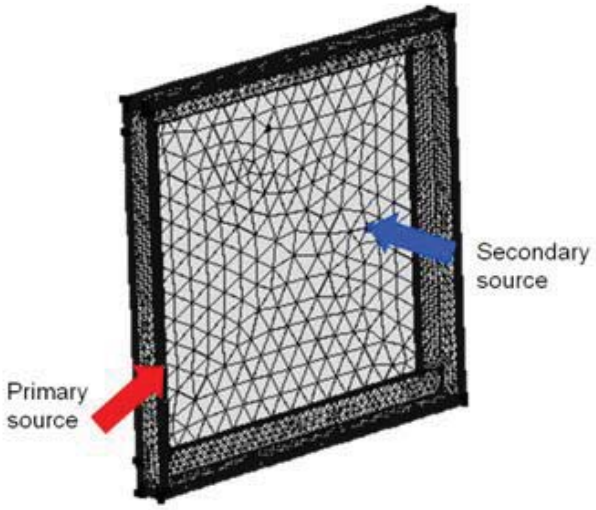

Figure 5.7: Finite element model of test rig.

were swept until the non trivial MAP point was found. The location of the secondary source was not optimized. A picture of the finite element model is presented in Fig. 5.7. Numerical boundary conditions were free-free.

Flexural kinetic energies for a single primary point force excitation for both the system and the plate subcomponent are presented in Fig. 5.8. Frequency responses exhibit many modes in the 500 to 2500 Hz interval. The system's flexural kinetic energy with and without MAP control around three of the structure's resonant frequencies (937, 1012, and 1215 Hz) are presented in Fig.5.9. MAP produced over 8 dB of attenuation at 937 and 1215 Hz, and no control at 1012 Hz. This lack of control for that particular resonance was due to the secondary excitation being located on a nodal line of the underlying structural mode.

The effect of the MAP control on the radiated sound field is presented in Fig. 5.10. When modes could be controlled, the radiated sound power was reduced by 9.5 and 8.5 dB at 937 Hz and 1215 Hz, respectively. Figures 5.8 and 5.9 show that there is a direct relationship between structural vibration and interior noise.

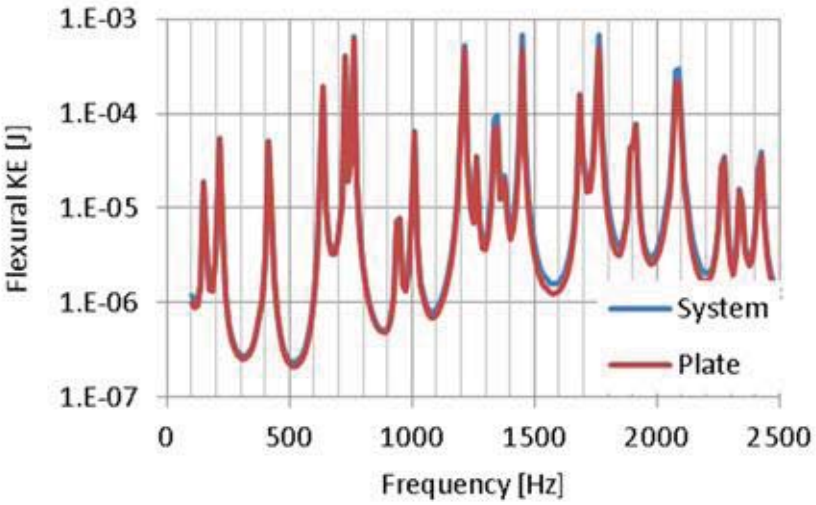

Figure 5.8: Rig flexural kinetic energy

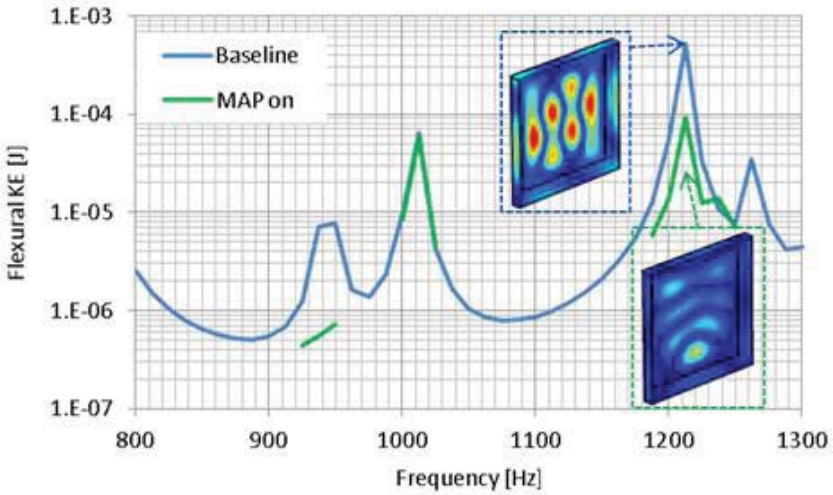

Figure 5.9: Flexural Kinetic Energy with and without MAP control.

5.2 Power Model for a Generic Actuator

The power model of a generic PZT actuator was developed in §3.4. Specifically, we relate the net electrical power in the actuator, the quantity that is measured, to the net mechanical

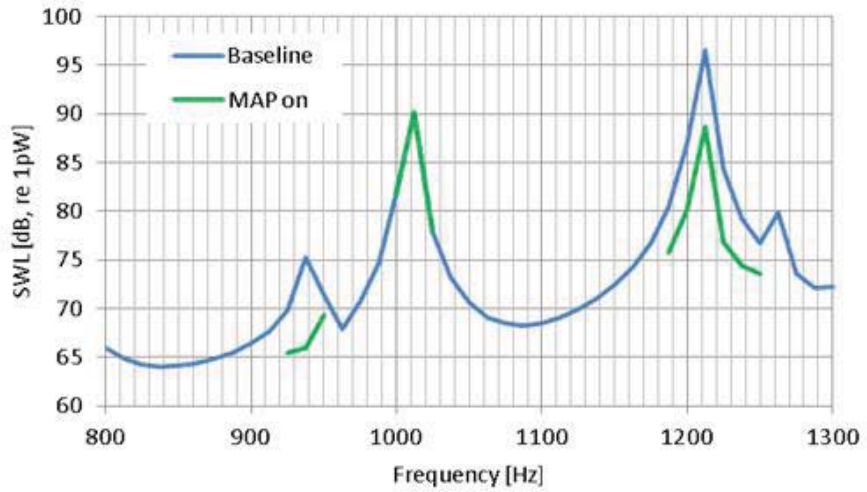

Figure 5.10: Radiated sound power with and without MAP control.

power, the quantity that is controlled, through the dielectric loss using the following equation:

$$\bar{P}_e = \frac{1}{2}\frac{\omega\, a^2}{h}|\bar{\mathrm{V}}|^2\, \bar{\varepsilon}_{33}\delta + \bar{P} \tag{5.51}$$

Equation (5.51) shows that the net input electrical power $\bar{P}_e$ is equal to the sum of the dielectric loss and the net input mechanical power $\bar{P}$. Note that even though Eq. (5.51) was derived for a PZT actuator, a similar relation can be derived for other actuators, for example, proof-mass actuators.

5.3 Test Rig and Plate Characterization

The main experimental efforts this year include: 1) verification of global power minimization using MAP, 2) implementation of MAP control on a realistic and sophisticated aircraft structure, and 3) experimental validation of the new MAP theory developed in §5.1.

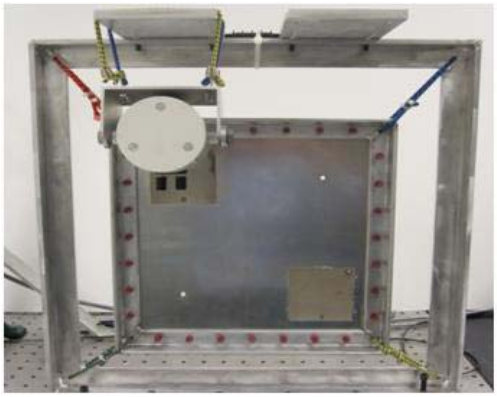

Figure 5.11: Test rig with a shaker and a PZT sensor/actuator pair.

A test apparatus was constructed to mimic a representative rotorcraft skin structure with more realistic vibration load paths from bulkhead to skin. An aluminum plate, 12 x 12 x 1/8 inches, was riveted by 28 aircraft grade rivets to a welded 1 x 1 inch aluminum angle frame. This design introduces contact surface and Coulomb damping to the test rig. The plate assembly is suspended by 4 bungee cords to mimic a free-free boundary condition, as shown in Figure 5.11. Two PZT patch sensor/actuators (2.5 x 2.5 x 0.005 inches) are bonded to the upper left and low right corners, respectively, one acting as a primary actuator (disturbance) and the other acting as a secondary actuator (control). A mini-shaker is attached to the plate via a piano wire stinger at the aluminum side wall as an alternative primary actuator to mimic distributed vibration load along the edges of the side walls to the aluminum plate.

The structural dynamic characterization of the newly constructed plate was conducted with a Polytec PSV-400/OFV5000 Laser Scanning Doppler Vibrometer (LSDV) as shown in Figure 5.12. The LSDV scans the plate surface in a grid of 320 x 320 nodes, and a laser pointer dwells on each node for a certain period to measure average vibration velocities orthogonal to the plane. The plate is excited by either the shaker or the primary PZT with a broad frequency band noise signal. The frequency response function (FRF) of the vibration velocities with respect to the excitation at each node is then calculated, and mode shapes of any selected frequencies are extracted from the FRFs.

Figure 5.12: Polytec Laser Scanning Doppler Vibrometer

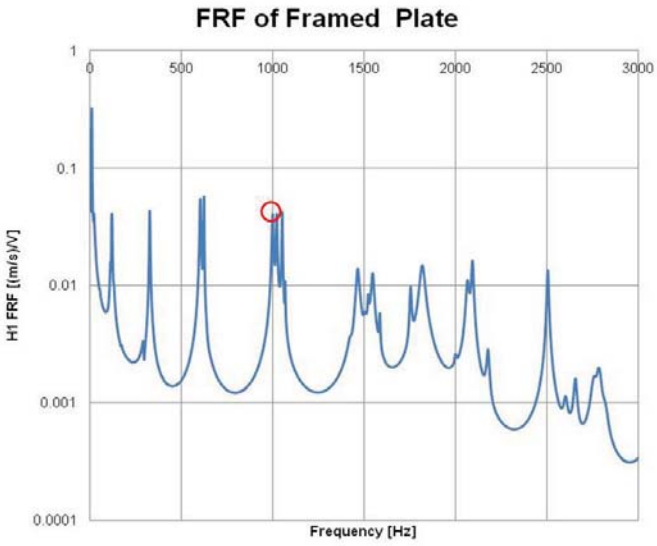

Figure 5.13: FRF of the plate measured by LSVD with shaker excitation. Red circle indicates the frequency selected for MAP testing

Figure 5.13 shows the measured mobility at the center of the plate for a shaker excitation at the edge of the side. There are over 20 strong vibration modes in the 0-3000 Hz frequency range. The modal cluster around 1000 Hz is of particular interest and is selected for MAP

control and analysis. The velocity mode shapes of 3 frequencies, 624 Hz, 999 Hz and 1052 Hz were extracted from the FRFs at all the nodes, as shown in Figure 5.14. The (2,2) mode of the plate at 999 Hz is selected for MAP control due to symmetry of the mode shape with respect to PZT actuator locations.

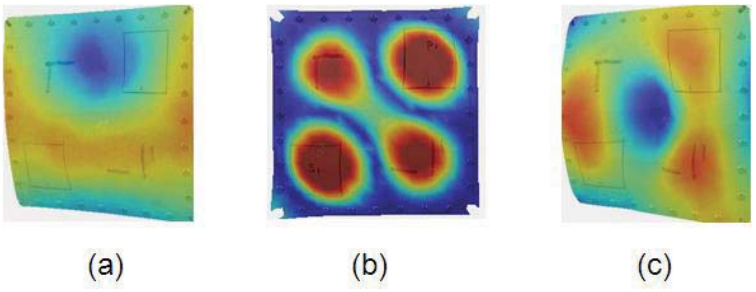

Figure 5.14: Velocity modal shapes for (a) 624 Hz (b) 999 Hz and (c) 1052 Hz

5.4 Experimental Validation of MAP Control

The validation of the global energy minimum at optimal control was conducted using a pair of PZT patches rather than using the shaker (as primary) and a PZT patch (secondary) due to some uncertainty and slight asymmetry of the mode shapes imposed by the attachment of the shaker. A frequency of 999 Hz (2,2 mode) was selected for MAP control. As can be seen from Figure 5.13, this frequency is closely coupled to other two modes. Minimization of global kinetic energy of the plate at optimal MAP control is verified by:

- Measuring velocity mode shapes of the plate at various excitation levels
- Calculating global kinetic energy of the plate

$$P_k = \sum_{i=1}^{l} \sum_{j=1}^{n} \frac{1}{2} m_{i,j} v_{i,j}^2 \tag{5.52}$$

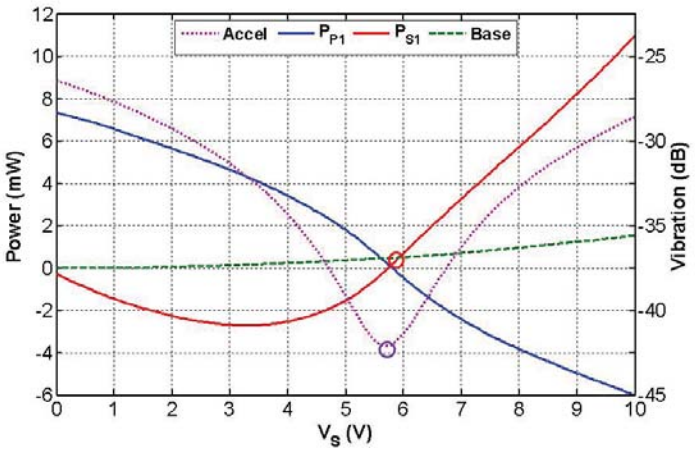

Figure 5.15: MAP control with a pair of PZT patch sensor/actuators. Red circle indicates MAP predicted optimal control at V_s=5.94V. Purple circle indicates optimal control at V_s=5.70V as predicted by the accelerometer.

where $v_{i,j}$ and $m_{i,j}$ are the vibration velocity and the mass of plate element at location i and j, respectively and $l \times n$ is the LSDV scan grid size.

- Identifying the optimal MAP control voltage V_s^* by sweeping V_s applied to the secondary actuator.
- Checking the correlation between V_s^*, minimum P_k and minimum acceleration measurement.

The harmonic primary excitation is kept constant at $V_p = 5$ V with primary phase equal to 0°. The optimal secondary phase was estimated to be 183.8° with respect to the primary. This is close to the true optimal of 180° (or 0°). The secondary voltage V_s is swept from 0 to 10 volts while its phase is kept fixed at 183.8°. The secondary power is acquired and compared to the predetermined aggregated power loss. Meanwhile, the acceleration of the plate center is monitored by the accelerometer. Figure 5.15 shows that the MAP criterion (intersection of the baseline with the secondary real electric power) predicts the optimal control to be $V_s = 5.94$ V while the acceleration reading indicates maximum vibration reduction(from -26

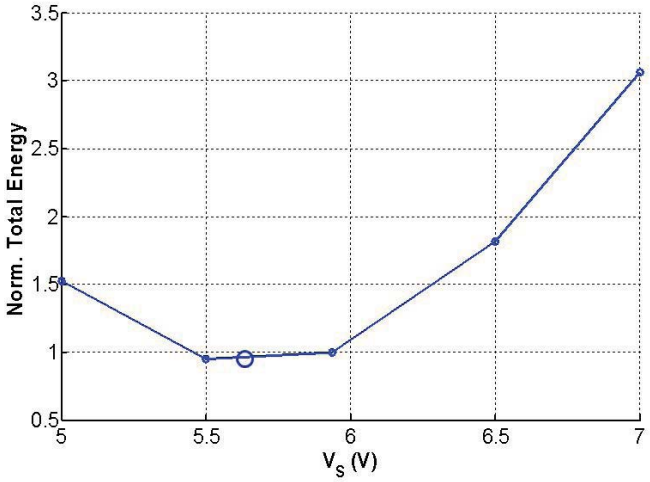

Figure 5.16: Normalized total kinetic power of the plate around optimal MAP control. Blue circle indicates global kinetic power of the plate at $V_s = 5.60$ V, and the normalized total energy is 28.1 at no control ($V_s = 0$).

dB to -42 dB) at $V_s = 5.70$ V. Figure 5.16, from the LSDV measurements, shows the total kinetic energy of the plate calculated from the mode shapes at different secondary voltages and normalized with respect to the total power at optimal control, that is, at $V_s = 5.94$ V and shows that the global power minimum occurs when $V_s = 5.60$ V. It can be seen that the acceleration measurement predicts the global energy minimum very well even though it is slightly off the hot spot of the mode shape.

5.4.1 Change in Mode Shapes with MAP Optimal Control

The effect of MAP control on mode shapes of the plate at 999 Hz is shown in Figure 5.17. The MAP control significantly reduces the vibration magnitude in the entire plate. It was also observed that the PZT actuators placed on the hot spots of the mode shape do not change the mode shape of a resonance frequency while significantly reducing the amplitude of the vibration. This test has demonstrated that optimal MAP control corresponds to minimum

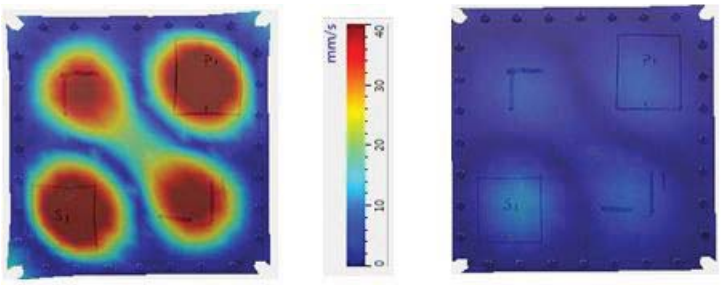

Figure 5.17: Velocity modal shapes in mm/s for no-control condition and with optimal MAP control ($V_s = 5.5$V). The low left square is the primary (excitation) and upper right the secondary (control).

global kinematic energy of the plate. The test also demonstrates that MAP control is capable of reducing the vibration of a plate with complexity in structure and damping mechanism effectively.

5.4.2 Validation of New MAP Algorithm

The main idea behind the new algorithm is to optimally locate the secondary actuator such that the cross mobility terms can be approximated as a single mode. This guarantees that MAP solution holds, that is, the optimal solution lies on the $P_s = 0$ curve for any arbitrary phasing of the primary actuators. The optimal secondary amplitude and phase can be determined for resonance and off-resonance cases. We used the shaker as the primary excitation and one of the PZT patches as the secondary actuator as shown in Fig. 5.11, §5.3. The excitation frequency was kept at 994 Hz. Figure 5.18 shows the experimental mode shape corresponding to 994 Hz. The secondary PZT actuator s_1 is shown in bottom left and is located close to the hot spot and is optimal for 994 Hz.

The first step in the new MAP algorithm is to find the optimal secondary phase. For resonant excitation, the optimal phase is given by the secondary phase at which the secondary power

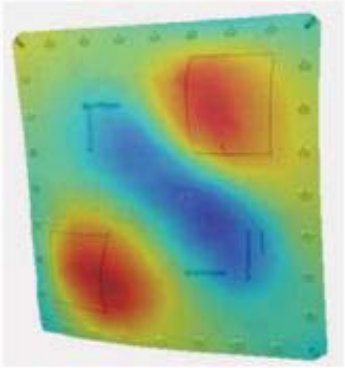

Figure 5.18: Experimental mode shape corresponding to resonant frequency 994 Hz

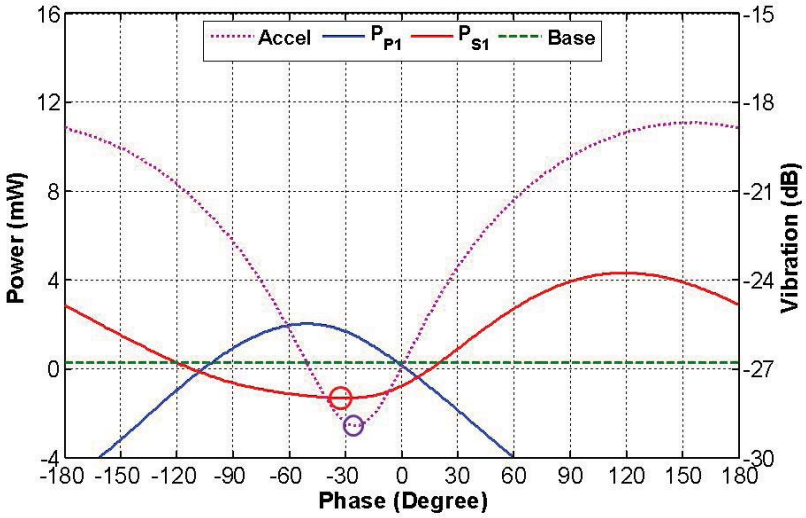

Figure 5.19: Plot showing implementation of optimal phase search. The optimal secondary phase is the phase at which the secondary phase is minimum or maximum.

is either a minimum or maximum for a given voltage. The primary excitation was 5 V and the phase was set to zero. With the secondary voltage equal to 3 V, the secondary phase was varied to find the phase for which the secondary power is a minimum or maximum. Figure

5.19 shows the variation of the secondary power P_s with respect to the secondary phase. It can be seen that the estimated optimal phase is -31^o where P_s is minimum, indicated by the red circle in Figure 5.19. Figure 5.19 also shows that the accelerometer reading, located close to the plate center, indicates that the vibration minimum occurs at -26^o (purple circle) which is close to the estimated value of -31^o.

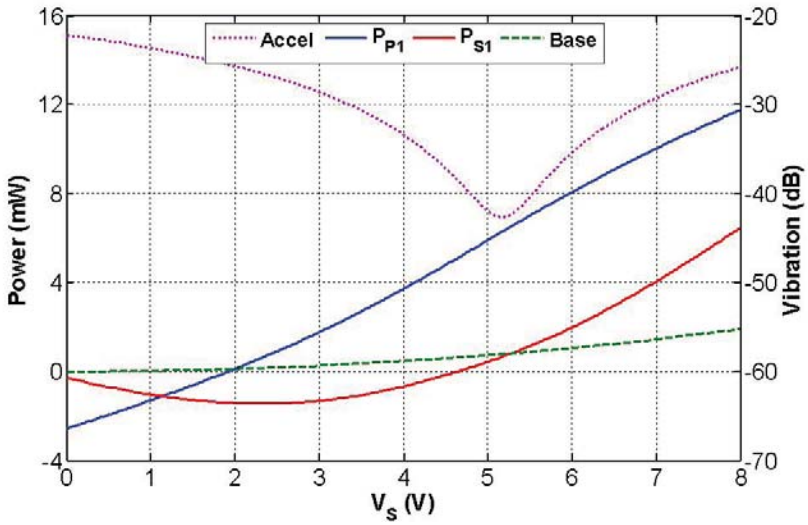

Figure 5.20: MAP control with secondary phase = -31^o

The next step is to fix the secondary phase at the optimal phase and sweep the secondary voltage to get the optimal voltage, indicated by intersection of the secondary power and the baseline loss curve. Figure 5.20 shows MAP performance when the secondary phase was set to -31^o. It can be seen from the accelerometer reading that a vibration reduction of 20 dB is achieved. When the secondary phase was set to -26^o, the MAP performance was greatly enhanced leading to a vibration reduction of 44 dB, see Figure 5.21.

In summary, the new MAP algorithm provides a novel way to find the optimal secondary phase and amplitude without any knowledge about the primary sources.

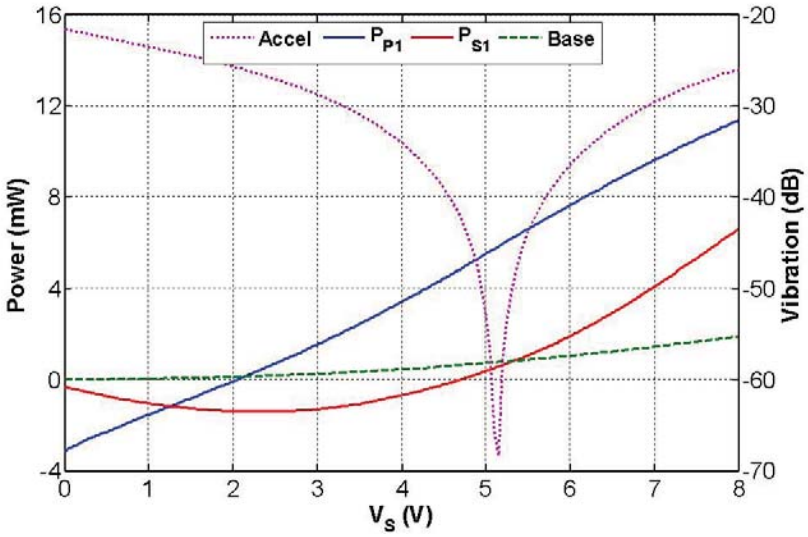

Figure 5.21: MAP control with secondary phase = -26^o

5.5 Rotorcraft Airframe Mockup

Modal analysis of the riveted structure revealed asymmetrical mode shapes and split resonance peaks that likely were resulting from asymmetrical boundary conditions due to the rivets and small variations in this fabricated structure. These experimental modes shapes could not be easily predicted using finite element models. To position secondary actuators for MAP, it is best to know the structural mode shapes to guarantee optimal control. Hence, to minimize the uncertainty in the mode shapes, we constructed a test structure without rivets but of similar geometry than the original panel. This new structure could be easily modeled and had predictable mode shapes and good separation of resonance frequencies.

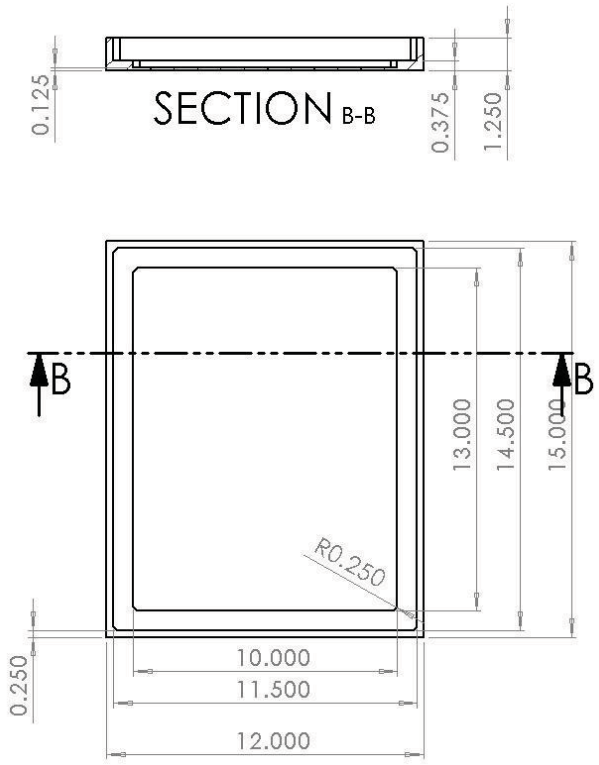

Figure 5.22: Test Plate Dimensions

5.5.1 Test Rig

The new test plate was fabricated through a milling process to enable seamless integration of angle frames to the plate. Detailed dimensions of the test plate are shown in Fig. 5.22. The assembly is suspended in air by 4 bungee cords to mimic free-free boundary conditions, as shown in Fig. 5.23. A mini-shaker is attached to the plate via a piano wire stinger at the aluminum side wall to mimic distributed vibration load along the edge of the plate.

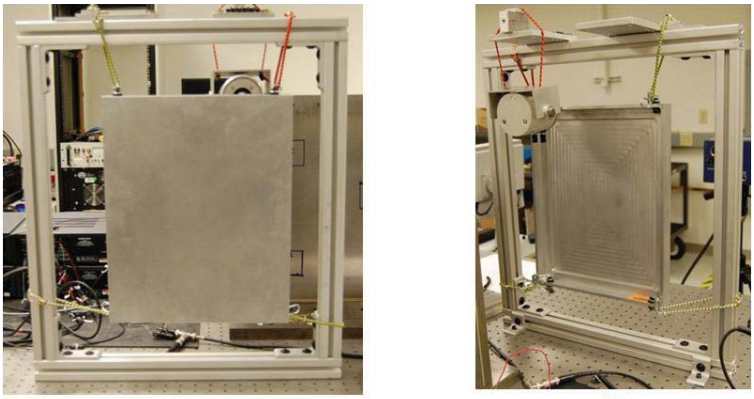

Figure 5.23: Picture of Test Rig showing (a) Front Face and (b) Back Face

5.5.2 Comparison between experimental mode shapes and FEM Analysis

The velocity frequency response function (FRF) of the plate is acquired by Laser Scanning Doppler Vibrometer (LSDV) and the plate is excited with broad band noise by the mini-shaker. Figure 5.24(a) shows FRF of the plate measured by LSDV and shaker excitation. A finite element analysis (FEA) of the plate was done to compare the frequency response and mode shapes. The frequency response from FEA is shown in Fig. 5.24(b). The experimental modal frequencies were within 1% of FEA results for frequencies within 500-2000 Hz range. We also compared the mode shapes for different resonant frequencies. For example, Fig. 5.25(a) shows the experimental mode shape, a (2,2) mode, for 947 Hz. Figure 5.25(b) shows that mode shape obtained from the FEA model at 940 Hz which is in excellent agreement with the experimental mode shape. Such good agreement is also evident at other resonant frequencies. For example, figures 5.26 and 5.27 compare the experimental mode shape with the mode shape calculated using FEA for 850 Hz and 1073 Hz respectively.

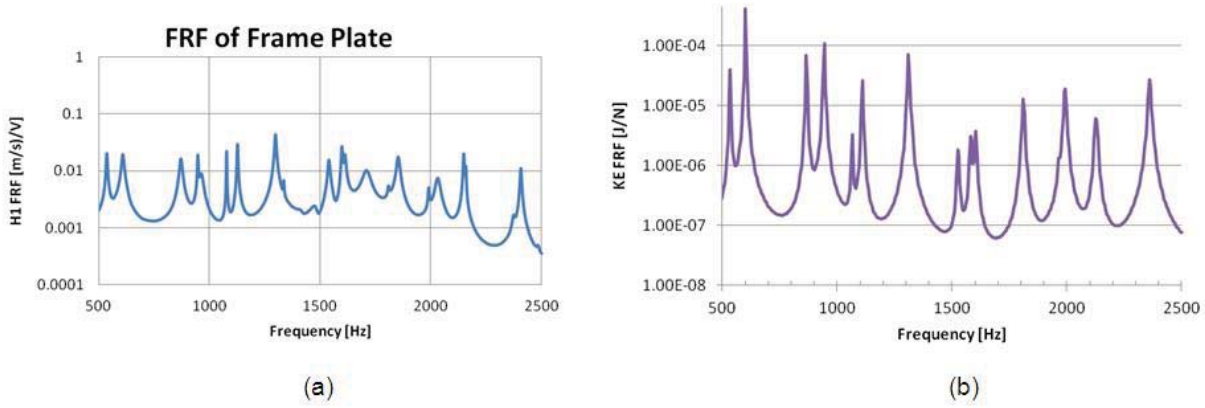

Figure 5.24: (a) FRF of the plate measured by LSVD and shaker excitation (b) Total plate KE per N of force, from FEA

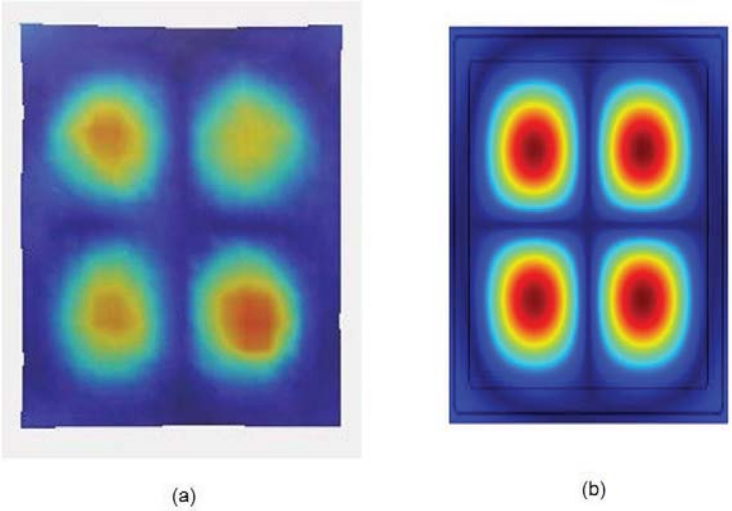

Figure 5.25: Mode shape comparison (a) Velocity modal shape at 947 Hz measured by LSVD and shaker excitation (b) Calculated vibration mode shape at 940 Hz

5.6 Effectiveness of MAP Control

In this section, we present experimental results that demonstrate the effectiveness of MAP control for single and multi-frequency excitation. We use the shaker as the primary excitation

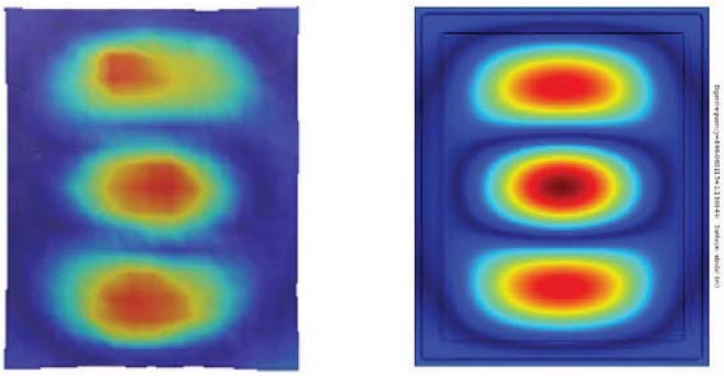

Figure 5.26: Mode shape comparison (a) Velocity modal shape at 850 Hz measured by LSVD and shaker excitation (b) Calculated vibration mode shape at 850 Hz

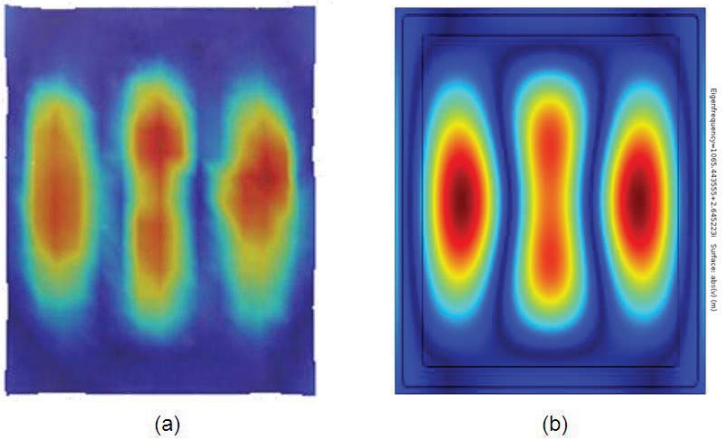

Figure 5.27: Mode shape comparison (a) Velocity modal shape at 1073 Hz measured by LSVD and shaker excitation (b) Calculated vibration mode shape at 1073 Hz

source and a PZT patch, located at the plate center, as the secondary excitation. The primary excitation has two resonant frequencies, 850 Hz and 1073 Hz. Figure 5.26 shows that the PZT location is optimal with respect with respect to the mode at 850 Hz whereas

Table 5.1: Primary Excitation Parameters

ω_{p11}	850 Hz	ω_{p12}	1073 Hz
V_{p11}	2.5 V	V_{p12}	4 V
ϕ_{p11}	30°	ϕ_{p12}	0°

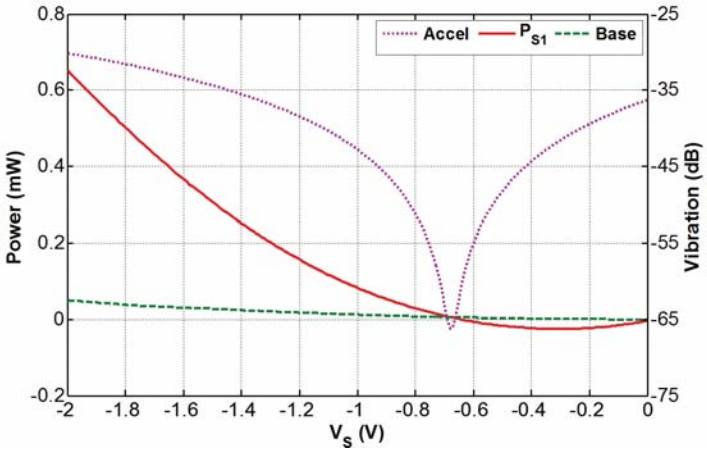

Figure 5.28: Voltage sweep showing the optimal secondary voltage at 850 Hz while control for 1073 Hz is off.

figure 5.27 shows that the PZT location, though good, is not the best location for the mode at 1073 Hz. As we discuss later, this is a good test of the effectiveness of MAP for sub-optimal locations of the PZT actuator. The primary excitation parameters are shown in Table 5.1. An accelerometer located at the plate center measured the local vibration levels whereas the global vibration was measured using the laser vibrometer.

850 Hz control with 1073 Hz not controlled

We use a frequency-by-frequency approach for controlling multi-frequency excitation. First, the optimal secondary voltage and phase are determined for the mode at 850 Hz while the

mode at 1073 Hz is not controlled. The optimal secondary phase corresponding to 850 Hz was found to $\phi_{s11} = 25.09^{o}$. With the secondary phase equal to the optimal phase, the voltage is varied till the secondary real power intersects the baseline curve to give the optimal voltage. See Fig. 5.28. It can be seen that at the optimal voltage, the local vibration is a minimum resulting in a 30 dB reduction.

1073 Hz control with 850 Hz controlled

With the control for 850 Hz on, the mode at 1073 Hz is controlled next. In this case, the optimal phase was determined to be $\phi_{s12} = -6.198^{o}$. With the secondary phase equal to the optimal phase, the voltage was varied to find the optimal secondary voltage at 1073 Hz as seen in Fig. 5.29. The local vibration level is minimum at optimal secondary voltage and the local vibration reduction is close to 20 dB.

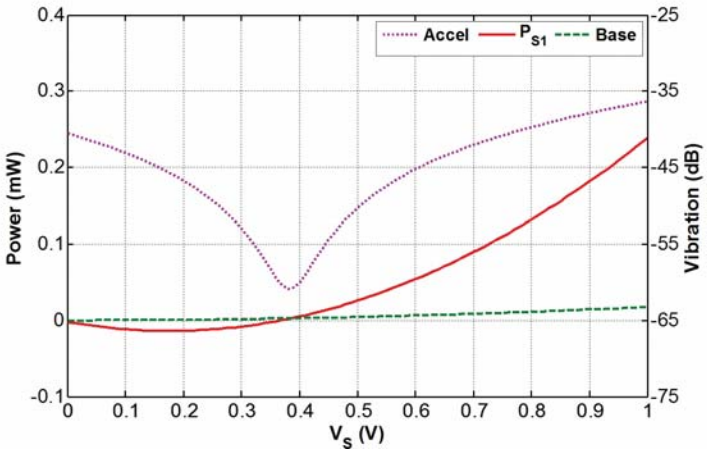

Figure 5.29: Voltage sweep showing the optimal secondary voltage at 1073 Hz while control for 850 Hz is active.

850 Hz control with 1073 Hz controlled

Finally, we control the 850 Hz excitation again while 1,073 Hz is under control. The optimal phase was estimated to be $\phi_{s11} = 26.010^{o}$ with local vibration reduction of 38.31 dB, which is 8.31 dB more than the single frequency case. Note that the local vibration reduction improved as a result of better optimal phase estimation. See Fig. 5.30. The vibration reduction for 1073 Hz was unaffected.

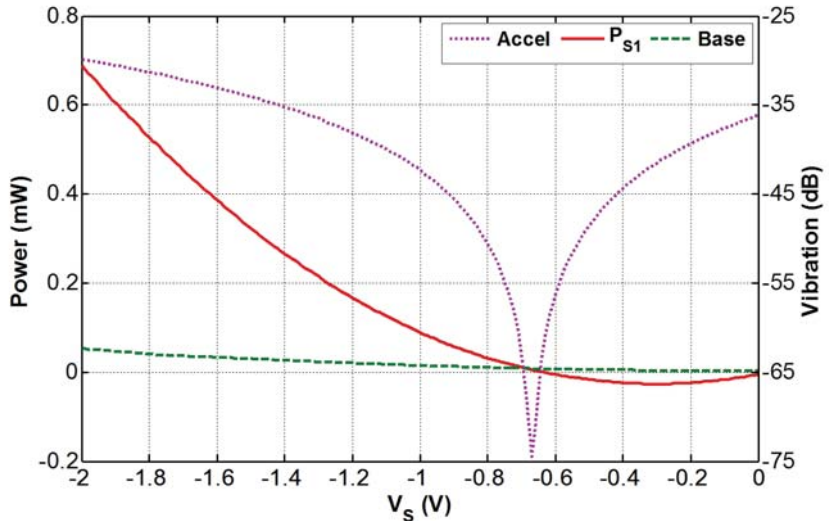

Figure 5.30: Voltage sweep showing the optimal secondary voltage at 850 Hz while control for 1073 Hz is on.

Global Vibration Reduction

Figures 5.29-5.30 show that MAP control results in significant local vibration reduction at both 850 Hz and 1073 Hz. However, it is important to verify whether we get similar performance globally. The global vibration levels were measured using the laser vibrometer. Figure 5.31 show the global vibration in dB with and without control. Figure 5.32 show

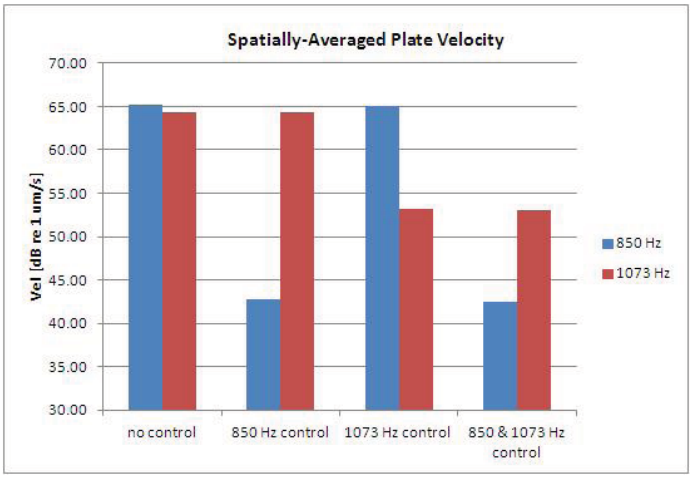

Figure 5.31: Plot showing global vibration levels with and without MAP control

the global vibration reduction. It can be seen that vibration reduction is around 22-23 dB for 850 Hz excitation whereas the 1073 Hz excitation was reduced by 11-12 dB. Though the global vibration reduction is not as high as the local reduction, as expected, it is still very significant.

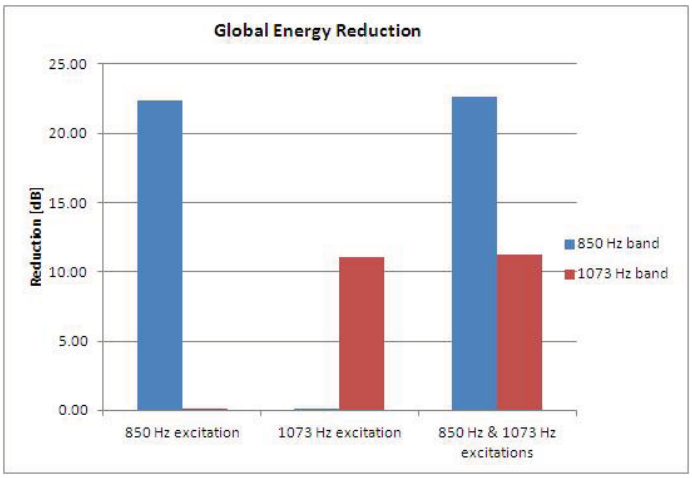

Figure 5.32: Global vibration reduction with MAP control.

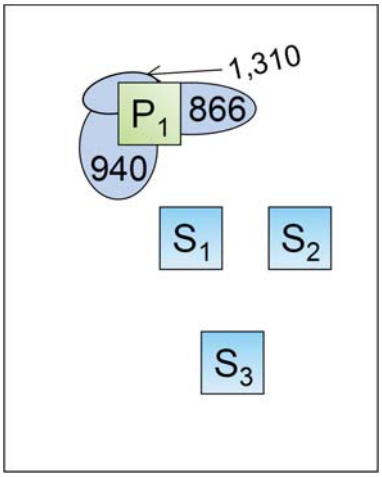

Figure 5.33: Illustration of PZT patch locations.

The above results demonstrate the effectiveness of MAP control for single and multi-frequency excitation. Also, note that dB reduction for the mode at 1073 Hz is less than the reduction at 850 Hz. This is due to the fact that the PZT location for 1073 Hz is sub-optimal. However, it is important to note that a global reduction of 11-12 dB is significant and demonstrates effectiveness of MAP control even when the PZT location is not optimal.

5.6.1 MAP Control with Multiple Secondary Controllers and Multiple Frequency

The LabVIEW code developed for testing was modified to excite and control three frequency signals with arbitrary phases. The shaker was used as the primary excitation source, and three PZT patches shown in Fig. 5.33 were used as secondary excitation sources. S_1 is placed at the center of the plate where optimal vibration reduction for 851.1 Hz (3 by 1 mode) is expected. Similarly, S_2 is located at the modal peak of 1,320 Hz. P_1 and S_3 are positioned at the intersection of 866, 940, and 1310 Hz based on FE analysis. The primary excitation has three resonant frequencies, 851.1, 945.2, and 1319.8 Hz. The primary excitation parameters are shown in Table 5.2. Table 5.3 shows estimated MAP parameters after phase and voltage

search for the MAP control.

Table 5.2: Primary Excitation Parameters

F_{Sh1}	851.1 Hz	F_{Sh2}	945.2 Hz	F_{Sh3}	1319.8 Hz
V_{Sh1}	2.5 V	V_{Sh2}	4.0 V	V_{Sh3}	3.0 V
ϕ_{Sh1}	30°	ϕ_{Sh2}	0°	ϕ_{Sh3}	60°

Table 5.3: Estimated Control Parameters (S_1, S_2, and S_3)

F_{S1}	851.1 Hz	F_{S3}	945.2 Hz	F_{S2}	1319.8 Hz
V_{S1}	-0.525 V	V_{S3}	-0.59 V	V_{S2}	-1.78 V
ϕ_{S1}	26.84°	ϕ_{S3}	135.83°	ϕ_{S2}	58.86°

With the control strategy established, the plate was excited, and the vibration response measured using the vibrometer at 99 (9 x 11 grid) locations on the test plate, phase-referenced to an accelerometer located at the back side of the S_3 center. The resulting mode shapes are captured in Fig. 5.34. The columns (left to right) summarize the different phases of multi-frequency MAP control: no control and three PZT control. The spatially averaged vibration response is depicted in Fig. 5.35. The control case reduces the global plate response at all three frequencies of 851.1, 945.2 and 1319.8 Hz with significant reductions. For the baseline case, the average vibratory responses were around 60 to 65 dB (0 dB at 1 m/s) for the no control case as depicted in Fig. 5.35. When control was applied to the three modes, the vibratory response exhibited significant reductions for each mode (19, 4.4, and 9.9 dB reduction, respectively).

MAP Control with Strategically Positioned Single Secondary

Experimental results presented here demonstrate the vibration reduction capability of a single secondary for multiple-frequency disturbance. The input to the shaker is kept unchanged (see Table 5.2), while only S_3 is used to control three frequencies. As previously described, S_3 is placed at the intersection of three mode shapes (851.1, 945.2 and 1319.8 Hz). Phase

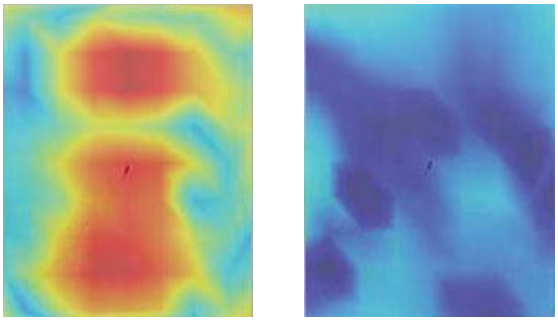

(a) 851 Hz (Baseline) (b) 851 Hz (Control)

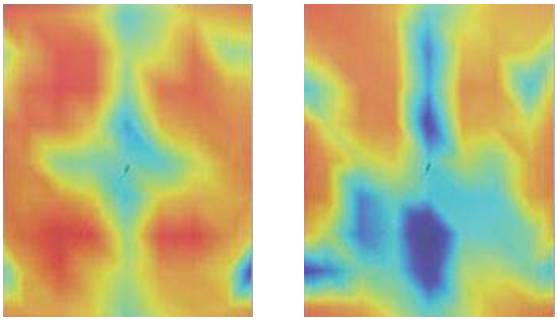

(c) 945 Hz (Baseline) (d) 945 Hz (Control)

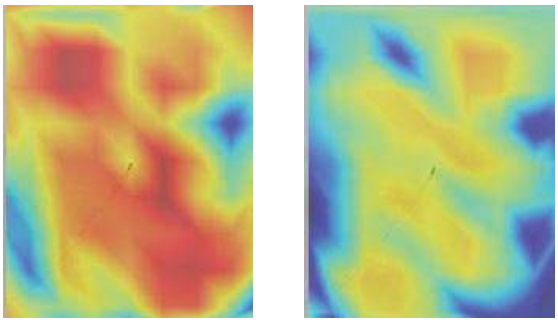

(e) 1320 Hz (Baseline) (f) 1320 Hz (Control)

Figure 5.34: Experimental Deflection Shapes for Three PZT Control

and voltage search for control parameter estimation was done before global vibration measurement as shown in Table 5.4.

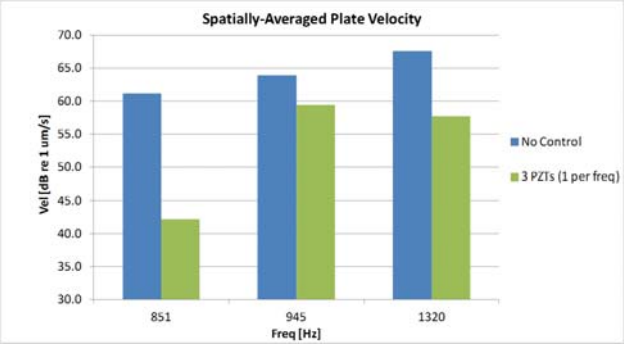

Figure 5.35: Average plate response with and without MAP control

Table 5.4: Estimated Control Parameters (S_3 only)

F_{S31}	851.1 Hz	F_{S32}	945.2 Hz	F_{S33}	1319.8 Hz
V_{S31}	0.755 V	V_{S32}	-0.59 V	V_{S33}	0.975 V
ϕ_{S31}	29.84°	ϕ_{S32}	135.83°	ϕ_{S33}	43.67°

Figure 5.36 shows the mode shapes before and after MAP control is applied for the respective frequencies. The spatially averaged vibration response is depicted in Fig. 5.37. The control cases reduce the global plate response at all three frequencies of 851.2, 943.7 and 1204.2 Hz with significant reductions as summarized in Fig. 5.38. It is noticeable that even a single PZT (S_3) alone can control multiple frequencies equivalently to three PZTs to which individual frequencies are assigned. In such a condition, a single control placed at the intersection of multiple (i.e., three and more) frequency modes can be used effectively to reduce overall vibration levels.

MAP for Off-Resonance Control

The excitation frequency was set to be harmonics of 300 Hz (600, 900, and 1,200 Hz), simulating gearbox vibrations not associated with natural frequencies of the test rig. Only S_3 was used for control. The primary excitation parameters are shown in Table 5.5 and

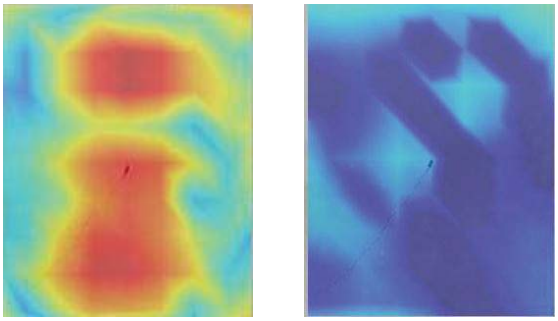

(a) 851 Hz (Baseline) (b) 851 Hz (Control)

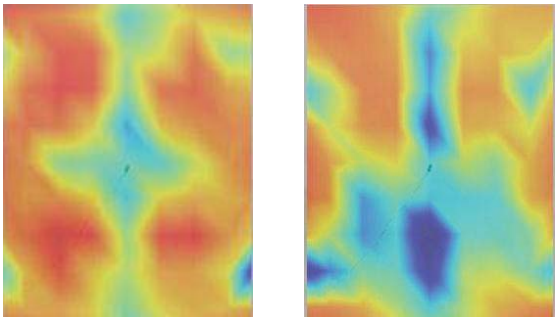

(c) 945 Hz (Baseline) (d) 945 Hz (Control)

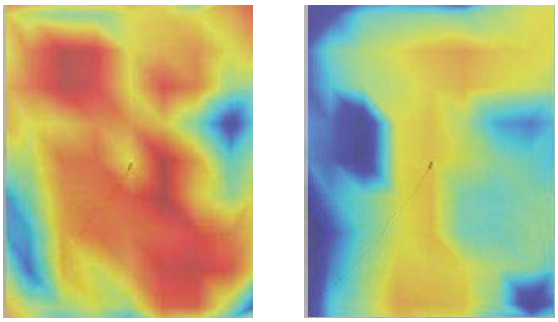

(e) 1320 Hz (Baseline) (f) 1320 Hz (Control)

Figure 5.36: Experimental Deflection Shapes for Multi-frequency control using a Single PZT Control

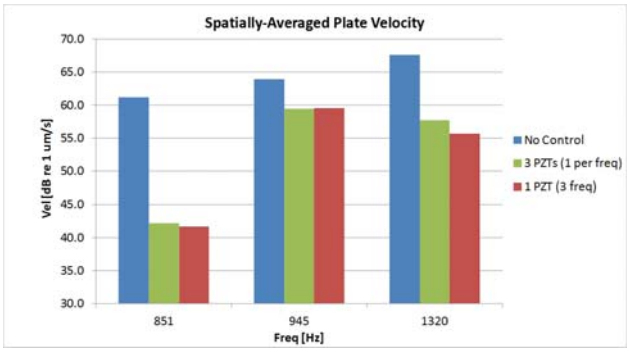

Figure 5.37: Average plate response with and without MAP control

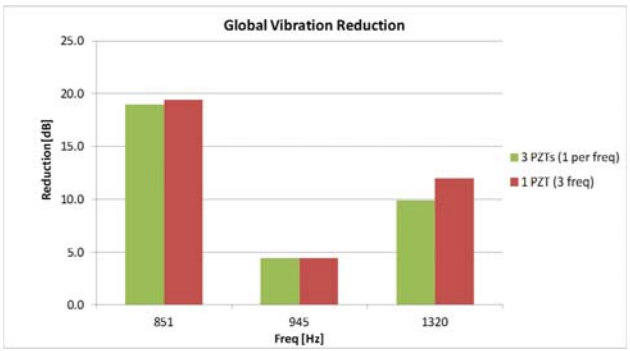

Figure 5.38: Plot showing global vibration with and without MAP control

Table 5.6 shows estimated MAP parameters after phase and voltage search for the MAP control. For the off resonance control, the challenge is that the amount of possible vibration reduction is dependent on the controller characteristic. Figure 5.39 is the baseline curve of S_3 PZT patch showing power directly measured from the PZT with respect to frequency. The red solid line is the mechanical response of the test rig which can be suppressed to baseline level (dotted line). At off-resonance frequencies, the amount of structural vibration is very close to the baseline power level, which complicates the MAP control algorithm search for optimal control parameters.

Figure 5.40 shows vibration plots before and after the MAP control is turned on. A 7.5 dB reduction was achieved at 1200 Hz, which is close to a resonance frequency of 1204 Hz. In

Table 5.5: Primary Excitation Parameters

F_{Sh1}	600 Hz	F_{Sh2}	900 Hz	F_{Sh3}	1200 Hz
V_{Sh1}	1.0 V	V_{Sh2}	6.0 V	V_{Sh3}	3.0 V
ϕ_{Sh1}	30°	ϕ_{Sh2}	0°	ϕ_{Sh3}	60°

Table 5.6: Estimated Control Parameters (S_3 only)

F_{S31}	600 Hz	F_{S32}	900 Hz	F_{S33}	1200 Hz
V_{S31}	-5.3 V	V_{S32}	0.37 V	V_{S33}	0.8 V
ϕ_{S31}	$-30°$	ϕ_{S32}	$-80°$	ϕ_{S33}	45°

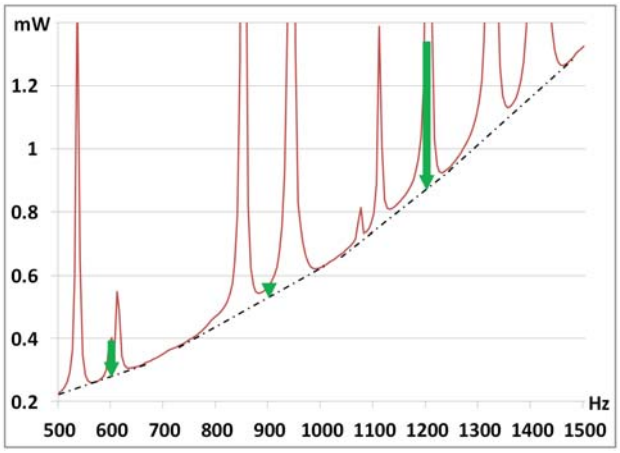

Figure 5.39: Plot showing S_3 baseline when 6.75 V is applied.

600 Hz and 900 Hz cases, while local mode shape changes were evident, no significant global reduction was made. For application of the MAP control algorithm to real structures, it is suggested to closely analyze the external vibration sources, and structural responses of the target structure. Then controller position can be determined based on a trade study to reduce global vibration response due to resonance and off-resonance frequencies.

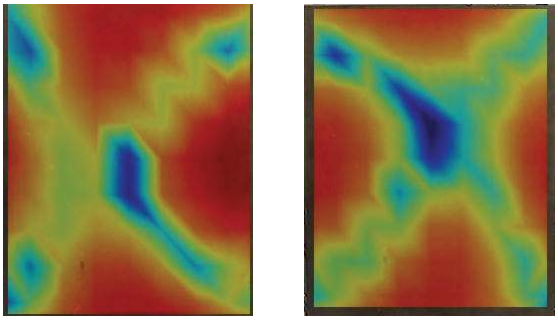

(a) 600 Hz (Baseline)

(b) 600 Hz (Control)

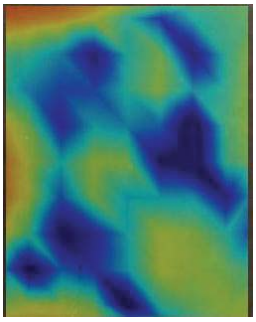

(c) 900 Hz (Baseline)

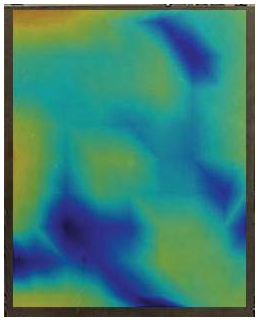

(d) 900 Hz (Control)

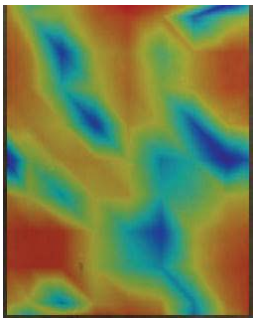

(e) 1200 Hz (Baseline)

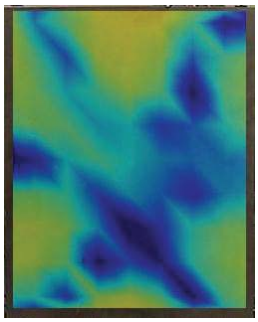

(f) 1200 Hz (Control)

Figure 5.40: Experimental Deflection Shapes for Off-Resonance Control using a Single PZT Control

5.7 Summary

The key accomplishments of the MAP feasibility analysis and rotorcraft vibration reduction are:

- The feasibility of the MAP control approach was assessed for multiple primary sources with arbitrary phasing. It was shown that optimizing the location of the secondary actuator with respect to the mode shapes guarantees that the secondary real power is zero at optimal control for resonance and off-resonance frequencies. An algorithm to find the optimal phase and magnitude of the secondary source was developed.
- A stable iterative scheme was developed to find the MAP solution for multiple secondary sources. The iterative algorithm is attractive for small number of secondary sources. An alternative approach was developed that is feasible for large number of secondary sources.
- Designed, modeled and built a test rig to mimic rotorcraft construction. Demonstrated MAP control with primary excitation using shaker with multiple frequencies and multiple secondary actuators for control.
- This research has led to an improvement in the technology readiness level (TRL) from 1 to 3-4.

Chapter 6

Effect of MAP Vibration Control on Radiated Noise For a Simple Interior Structure

We present some preliminary analysis showing the potential benefit of MAP control to reduce noise in the passenger cabin due to the main rotor transmission excitation, the NASA program goal. Helicopter gearbox excitations are transmitted to the fuselage via rigid connections at the transmission well. Subsequently, the frame and skins of the fuselage transmit the vibrations produced by the main gearbox and radiate sound into the cabin interior. While representative of helicopter interior skin panel, the plate structure used for the development of MAP control was relatively small and had few structural modes in the 500 to 2500 Hz range. A fully coupled vibro-acoustic finite element model of a larger, more realistic and modally denser structure was used to evaluate MAP potential. Although recognized as a rather simplistic representation of a real helicopter interior, this model is a step closer to evaluating MAP performance on radiated interior noise levels. Up to this point, the MAP development program focused on demonstrating vibration reductions that are expected to lead to noise reduction.

6.1 Model description

An acoustic cavity of dimension $1 \times 1.1 \times 1.03m^3$ is enclosed in an aluminum structure composed of 2-mm thick panels with $20 \times 20mm^2$ beams in all corners. The panels are modeled as shells, whereas the reinforcement beams are solid elements. A schematic of the structure is presented in Fig. 6.1. The base of the structure was simply supported.

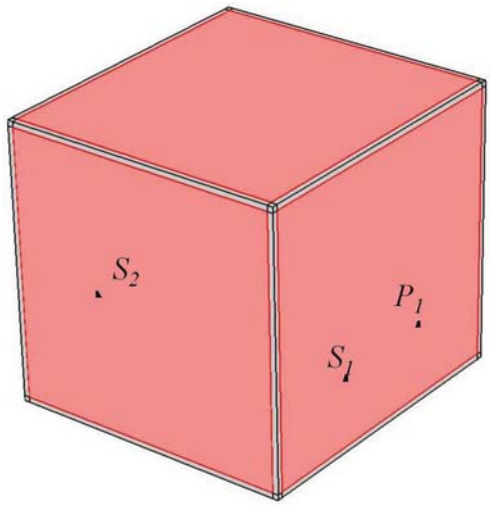

Figure 6.1: Schematic of the box structure.

A primary point force excitation P_1 is applied to one panel of the structure. MAP control was applied using a single secondary point force. The secondary was either located on the same panel as the primary (S_1), or on an adjacent panel (S_2). The locations of (S_1) or (S_2) were not optimized for a broad range control or single mode control, but assigned by visual inspection on hotspots of the forced response at 505 Hz (P_1 only).

6.2 Results

The performance of the controller was evaluated by using the structural kinetic energy in all the panels, as well as the averaged sound pressure levels (SPL) in the acoustic cavity. The frequency responses without control are presented in Fig. 6.2. The many peaks in the structural responses suggest that the modal density is already relatively high, whereas there is still a lot of separation between peaks in the acoustic response.

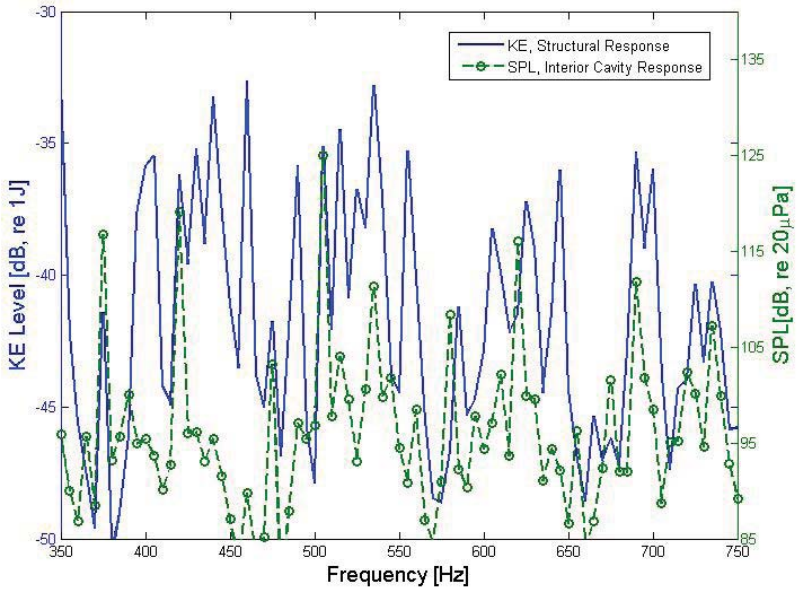

Figure 6.2: System frequency responses for the box structure with no control.

For this study, the structure was excited at 505 Hz, a frequency close to a resonance of the acoustic cavity, and also in a range where the structure is modally dense. The structural and acoustical fields at 505 Hz are presented in Fig. 6.3. Results when MAP control is applied at S_1 are shown in Fig. 6.4. The MAP condition, where the structural kinetic energy is minimized, is noted with the vertical dashed line. The total kinetic energy level was reduced by 6.1 dB, and the averaged SPL dropped by 13.8 dB. While the kinetic energy

was minimized at MAP, a greater SPL reduction (15.5 dB) could be achieved for slightly larger force amplitude since the acoustic resonance is not exactly at 505 Hz and MAP controls the underlying dominant structural mode.

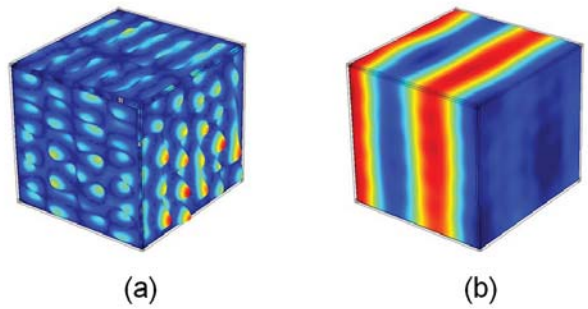

Figure 6.3: Response fields at 505 Hz (no control). (a) Structural displacement (b) Acoustic pressure

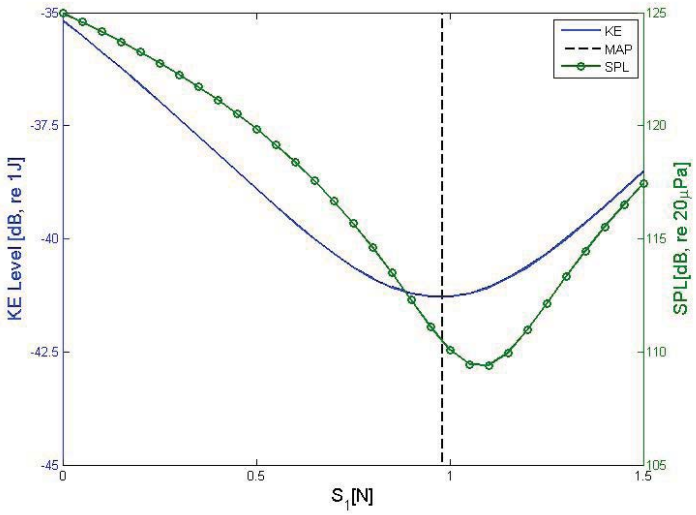

Figure 6.4: The total kinetic energy and SPL for S_1 MAP Control

With MAP control applied at S_2, the total kinetic energy level was reduced by 7.0 dB, and the averaged SPL dropped by 13.6 dB. Thus, MAP control can be very effective at reducing

the injected power even when the secondary actuation is located away from the primary sources and in a system where energy has many paths to propagate.

Results of the MAP control as applied on the complex structure demonstrate that MAP has good potential at reducing sound inside a cavity, even if the secondary forces are not in close proximity to the primary excitations. The study was limited to a single point of control and should be expanded to multiple actuators and multiple frequencies to evaluate the performance of the control. In addition, the control was applied at a frequency close to both a structural and acoustic resonance. Other cases of interest include frequencies where at most one of the domains is very close to a resonance.

Chapter 7

Conclusions and Next Steps

A novel active vibration control strategy called Minimum Actuation Power (MAP) is presented for a structure excited by multiple primary (excitation) sources and controlled by multiple secondary (control) sources. MAP is an optimal control strategy that minimizes the total input power into the structure by monitoring the input power from the secondary source only and therefore does not need any knowledge about the primary sources.

The theory of MAP was first developed for a structure excited by a single primary source and controlled by a single secondary source. It was shown that the real input(mechanical) power in the secondary source goes exactly to zero when the total input power from both the primary and secondary source is minimized. This leads to a novel way to implement MAP control without explicit knowledge about the magnitude and location of the primary excitation. In order to validate the theoretical findings, a model for a simply supported plate excited by a primary piezo-electric (PZT) patch actuator and controlled by a secondary piezo-electric patch actuator was developed. An electromechanical coupling model of piezoelectric patch actuator with a plate structure is developed. A simple relation between the real electrical power and the real input power of the piezo-electric actuator was developed. This enabled implementing MAP control using the real electric power in the secondary actuator. The effectiveness of MAP control was demonstrated for resonant and off-resonant excitation

frequencies. It was first shown through simulations that optimizing the location of the secondary actuator can help control otherwise uncontrolled modes very effectively. The MAP theory was extended to multi-frequency excitation and simulations were presented to validate the theory. A test setup that mimics simply supported boundary conditions was built to validate the theoretical findings. To implement MAP using electrical power, tests were done to characterize the power consumption of the plate and the dielectric loss of the piezo-electric patch actuators. The MAP control algorithm was tested for on-resonance and off-resonance frequencies and effectiveness of MAP for vibration reduction. We demonstrated up to 47 dB vibration reduction at resonance and 7 dB vibration reduction at off-resonance, as measured by a single accelerometer at the plate center. There was good qualitative agreement between the experimental results and theoretical findings.

The MAP control approach was extended to multiple primary excitations with zero relative phasing and multiple secondary excitations. It was shown that when the primary excitations have the same phasing, then the real secondary power is zero when the total input power is minimized. However, when the primary excitations have arbitrary phasing, the secondary real power is not always zero when the total input power is minimized. It was shown that the MAP condition is exactly satisfied when the secondary sources are located symmetrically with respect to the primary sources. However, such a constraint on the secondary source locations is hard to satisfy in practice. Extending the single actuator model, we developed an electro-mechanical model for a simply supported plate excited by multiple primary and multiple secondary PZT patch actuators. Performance of MAP control as a function of the location and number of the secondary sources was assessed. It was seen that increasing the number of secondary sources improves vibration reduction. Also, multiple secondary sources can be useful when vibration reduction over a frequency band is sought. Experimental validation of MAP control was demonstrated in the lab with two primary and two secondary excitations using an aluminum plate as well as a composite panel. For example, we demonstrated 20 dB vibration reduction for the aluminum plate and 12 dB vibration reduction for the composite plate, as measured by a single accelerometer at the plate center. A test for real-time implementation was developed to automate MAP control strategy.

The feasibility of MAP control approach for reducing airframe vibrations due to the rotorcraft main rotor transmission and the reduction of corresponding sound levels in the passenger cabin was assessed using a more meaningful metric for vibration reduction, the global

kinetic energy of the plate structure. MAP feasibility was assessed for multiple primary excitation sources with arbitrary relative phasing and with multiple frequencies controlled by multiple secondary sources. In order to circumvent the problem of placing the secondary actuators symmetrically with respect to the primary sources to satisfy the MAP condition, it was shown that placing the the secondary sources at the intersection of the node lines of the neighboring modes can guarantee that the secondary real power is zero at optimal conditions even when the primary sources have arbitrary phasing. An algorithm to compute the optimal secondary phase and magnitude was developed for resonant and off-resonant excitation frequencies. A stable iterative solution for finding the MAP solution for multiple secondary sources was developed. The stable iterative solution, however, is not feasible for large number of secondary sources. An alternative feasible approach was developed to find the MAP solution when the secondary sources are large in number. A test rig to mimic rotorcraft construction was designed, modeled and built. MAP control with primary excitation using shaker, in addition to PZT, with multiple frequencies and multiple secondary actuators for control was demonstrated. It was shown that MAP control achieved significant vibration reduction with average global vibration reduction of the order of 15-20 dB for single frequency with one secondary actuator. A single secondary actuator was optimized to control multiple frequencies, in some cases up to 3 frequencies with 8-10 dB average global vibration reduction for each frequency.

A fully coupled vibro-acoustic finite element model of a larger, more complex and modally denser box type structure was used as a quick evaluation of the potential of MAP to reduce noise in the passenger cabin due to the main rotor transmission excitation. It was shown that MAP control resulted in 6.1 dB reduction in the total kinetic energy of the structure while the averaged sound pressure levels (SPL) in the acoustic cavity dropped by 13.8 dB at resonant excitation. This preliminary analysis clearly shows the potential of MAP in reducing interior noise in a helicopter cabin.

Next Steps

Possible future directions include establishing physical system design rules for actuator density that leverages the highly distributed actuation opportunities offered by MAP and op-

timal actuator positions on a generic panel. It is important to quantify the cost/benefit of MAP on an aircraft-level system for both tonal and broadband sources using analysis and tests. Finally, there is a need for better understanding of the vibration path and the structural contributions to interior noise using a detailed diagnostic survey of vibro-acoustic problem and the impact of composite structures and improved gear designs or gear noise reduction technologies should be studied to assess the interior noise challenges of the future.

Bibliography

[1] T. J. Sutton, S. J. Elliott, M. J. Brennan, K. H. Heron, and D. S. C.Jessop. Active isolation of multiple structural waves on a helicopter gearbox support strut. *Journal of Sound and Vibration*, 205:81–101, 1997.

[2] S. Asiri, A A. Baz, and D. Pines. Active periodic struts for a gearbox support system. *Smart Materials and Structures*, 15:1707–1714, 2006.

[3] P. Belanger, A. Berry, Y. Pasco, O O. Robin, Y. St-Amant, and S. Rajan. Multi-harmonic active structural acoustic control of a helicopter main transmission noise using the principal component analysis. *Applied Acoustics*, 70:153–164, 2009.

[4] W. Welsh, C. Fredrickson, C. Rauch, and I. Lyndon. Flight test of an active vibration control system on the uh-60 black hawk helicopter. In *Proceedings of the American Helicopter Society 51st Annual Forum, Fort Worth, Texas*, 1995.

[5] R. K. Goodman and T. A. Millott. Design, development and flight testing of the active vibration control system for the sikorsky s-92. In *Proceedings of the American Helicopter Society 56th Annual Forum, Virginia Beach, Virginia*, 2000.

[6] T. A. Millott, R. K. Goodman, J. K. Wong, W. A. Welsh, J. R. Correia, and C. E. Cassil. Risk reduction flight test of a pre-production active vibration control system for the uh-60m. In *Proceedings of the American Helicopter Society 59th Annual Forum, Phoenix, Arizona*, 2003.

[7] J. K. Wong, W. A. Welsh, R. Lamb, and K. Dyer. Risk reduction flight test of a pre-production active vibration control system for the mh-60s. In *Proceedings of the AHS Vertical Lift Aircraft Design Conference, San Francisco, California*, 2006.

[8] P. A. Nelson and S. J. Elliott. *Active control of sound*. Academic Press, 1993.

[9] S. M. Kuo and D. R. Morgan. *Active noise control systems*. Wiley, 1996.

[10] S. J. Elliott. *Signal processing for active control*. Academic Press, 2001.

[11] S. J. Elliott, P. A. Nelson, I. M. Stothers, and C. C. Boucher. In-flight experiments on the active control of propeller-induced cabin noise. *Journal of Sound and Vibration*, 140:219–238, 1990.

[12] P. J. B. Jackson and C. F. Ross. Application of active noise control in corporate aircraft. In *Proceedings of the ASME International Congress and Exposition, Active Control of Vibration and Noise, Atlanta, Georgia*, 1996.

[13] I. U. Borchers, U. Emborg, A. Sollo, E. H. Waterman, J. Paillard, P. N. Larsen, G. Venet, P. Goeransson, and V. Martin V. Advanced study for active noise control in aircraft. In *Fourth Aircraft Interior Noise Workshop, NASA Langley*, pages 129–141, 1992.

[14] K. Kochan, D. Sachau, and H. Breitbach. Active noise control inside the loadmaster area of a turboprop transport aircraft. In *Proceedings of the 15th AIAA/CEAS Aeroacoustics Conference, Miami, Florida*, 2009.

[15] M. R. Jolly, M. A. Norris, D. J. Rossetti, J. L. Potter, and J. V. Warne K. F. Delfosse. A demonstration of active control for helicopter cabin noise reduction. In *Proceedings of the 20th European rotorcraft forum*, pages 1–14, 1994.

[16] D. G. MacMartin, M. W. Davis, C. A. Yoerkie, and W. A. Welsh. Helicopter gear-mesh anc concept demonstration. In *Proceedings of the Proceedings of Active 97*, pages 529–542, 1997.

[17] T. A. Millott, W. A. Welsh, C. A. Yoerkie, D. G. MacMartin, and M. W. Davis. Flight test of active gear-mesh noise control on the s-76 aircraft. In *Proceedings of theAmerican Helicopter Society 54th Annual Forum, Washington, D.C*, 1998.

[18] C. R. Fuller, S. J. Elliott, and P. A. Nelson. *Active control of vibration*. Academic Press, 1996.

[19] A. Preumont. *Vibration control of active structures*. Kluwer, 2002.

[20] C. R. Fuller, S. D. Snyder, C. H. Hansen, and R. J. Silcox. Active control of interior noise in model aircraft fuselages using piezoceramic actuators. *AIAA Journal*, 30(11):2613–2617, 1992.

[21] W. T. Baumann, W. R. Saunders, and H. H. Robertshaw. Active suppression of acoustic radiation from impulsively excited structures. *Journal of the Acoustical Society of America*, 90(6):3202–3208, 1991.

[22] R. L. Clark and C. R. Fuller. A model reference approach for implementing active structural acoustic control. *Journal of the Acoustical Society of America*, 92(3):1534–1544, 1992.

[23] P. Gardonio, E. Bianchi, and S. J. Elliott. Smart panel with multiple decentralized units for the control of sound transmission. part ii: design of the decentralized control units. *Journal of Sound and Vibration*, 274:193–213, 2004.

[24] Y. Aoki, P. Gardonio, and S. J. Elliott. Rectangular plate with velocity feedback loops using triangularly shaped piezoceramic actuators: Experimental control performances. *Journal of the Acoustical Society of America*, 123(3):1421–1426, 2008.

[25] P. A. Nelson, A. R. D. Curtis, S. J. Elliott, and A. J. Bullmore. The minimum power output of free field point sources and the active control of sound. *Journal of Sound and Vibration*, 116 (3), 1987.

[26] S. J. Elliott, P. Joseph, P. A. Nelson, and M. E. Johnson. Power output minimization and power absorption in the active control of sound. *Journal of the Acoustical Society of America*, 90(5), 1991.

[27] M. E. Johnson and S. J. Elliott. Measurement of acoustic power output in the active control of sound. *Journal of the Acoustical Society of America*, 93(3), 1993.

[28] O. Bardou, P. Gardonio, S. J. Elliot, and R. J. Pinnington. Active power minimization ans power absorption in a plate with force and moment excitation. *Journal of Sound and Vibration*, 208 (1):111–151, 1997.

[29] P. A. Nelson, A. R. D. Curtis, S. J. Elliott, and A. J. Bullmore. The equivalent impedance of power-minimising vibration controllers on plates. *Journal of Sound and Vibration*, 283 (1-2), 2005.

[30] J. J. Dosch. Self-sensing piezoelectric actuator for collocated. *Journal of Intelligent Material Systems and Structures*, 3 (1):166–185, 1992.

[31] C. Liang, F. P. Sun, and C. A. Rogers. Determination of the optimal actuator locations and configurations based on actuator power factors. In *Proceedings of the Fourth International Conference on Adaptive Structures*, 1993.

[32] C. Liang, F. P. Sun, and C. A. Rogers. Investigation of the energy transfer and power consumption of adaptive structures. In *Proceedings of the 31st Conference on Decision and Control*, 1992.

[33] S. Zhou, C. Liang, and C. A. Rogers. Coupled electro-mechanical impedance modeling to predict power requirement and energy efficiency of piezoelectric actuators integrated with plate-like structures. In *Proceedings of the M A S M E Adaptive Structures Forum*, 1994.

[34] N. W. Hagood, W. H. Chung, and A. von Flotow. Modeling of piezoelectric actuator dynamics for active structural control. *Journal of Intelligent Material Systems and Structures*, 1(1).

[35] D. J. Warkentin and F. E. Crawley. Power amplification for piezoelectric actuators in controlled structures. *MIT Space Engineering Research Center Technical Report*, SERC 4-95, 1995.

[36] M. C. Brennan and A. R. McGowan. Piezoelectric power requirements for active vibration control. In *Proceedings of Smart Structures and Materials*, pages 660–669, 1997.

[37] G. E. Simmers, J. R. Hodgkins, D. D. Mascarenas, G. Park, and H. Sohn. Improved piezoelectric self-sensing actuation. *Journal of Intelligent Material Systems and Structures*, 15(12):941–953, 2004.

[38] T. Jordan, Z. Ounaies, J. Tripp, and P. Tcheng. Electrical properties and power considerations of a piezoelectric actuator. *NASA/CR-2000-209861, ICASE Report No. 2000-8*, 2000.

[39] M. I. Frecker. Recent advances in optimization of smart structures and actuators. *Journal of Intelligent Material Systems and Structures*, 14:207–216, 2003.

[40] A. M. Sadri, J. R. Wright, and R. J. Wynne. Modeling and optimal placement of piezoelectric actuators in isotropic plates using genetic algorithms. *Smart Materials and Structures*, 8 (4):490, 2003.

[41] G. Pavic. Role of damping on energy and power in vibrating systems. *Journal of Sound and Vibration*, 281:45–71, 2005.

[42] A. V. Oppenheim and R. W. Schafer. *Discrete-Time Signal Processing*. Prentice Hall, 1999.

[43] S. Zhou, C. Liang, and C. A. Rogers. An impedance based system modeling approach for induced strain actuator driven structures. *Journal of Vibration and Acoustics*, 118:323–332, 1996.

Appendix A

Total input power due to primary and secondary patches

Let us assume that the primary and secondary patch edges are discretized into an equal number of elements, say q. Let p_i and s_i represent the coordinates of the center of the i^{th} primary and secondary patch element respectively where $i = 1, \ldots, q$. Let M_p and M_s be the primary and secondary moments acting on each element respectively. Consider the point p_i on the primary patch. The angular velocity at this point is a sum of the angular velocity induced by the the primary and secondary patch moments and can be expressed as

$$W_{p_i} = \sum_j W_{p_i p_j} + \sum_j W_{p_i s_j} \tag{A.1}$$

where $W_{p_i p_j}$ is the angular velocity induced at p_i due to the moment M_p at location p_j and $W_{p_i s_j}$ is the angular velocity induced at p_i due to the moment M_s at location s_j. The angular

velocities $W_{p_ip_j}$ and $W_{p_ip_j}$ can be expressed as

$$\begin{aligned} W_{p_ip_j} &= P_{p_ip_j} M_p \\ W_{p_is_j} &= P_{p_is_j} M_s \end{aligned} \tag{A.2}$$

where $P_{p_ip_j}$ and $P_{p_is_j}$ are the cross mobility terms given by [28]

$$\begin{aligned} P_{p_ip_j} &= \sum_{n=1}^{\infty} \left(\eta\omega\omega_n^2 + j\omega(\omega_n^2 - \omega^2)\right) \frac{4\,\psi_n^{\delta_{p_i}}(p_i)\,\psi_n^{\delta_{p_j}}(p_j)}{m\left[(\omega_n^2 - \omega^2)^2 + \omega_n^4\eta^2\right]} \\ P_{p_is_j} &= \sum_{n=1}^{\infty} \left(\eta\omega\omega_n^2 + j\omega(\omega_n^2 - \omega^2)\right) \frac{4\,\psi_n^{\delta_{p_i}}(p_i)\,\psi_n^{\delta_{s_j}}(s_j)}{m\left[(\omega_n^2 - \omega^2)^2 + \omega_n^4\eta^2\right]} \end{aligned} \tag{A.3}$$

where η is the structural damping, m is the plate mass, ω is the excitation frequency (assumed same for primary and secondary excitation) and ω_n is the n^{th} resonant frequency given by

$$\omega_n = \sqrt{\frac{EH^2}{12(1-\mu^2)\rho}} \left(\left(\frac{n_1\pi}{L_x}\right)^2 + \left(\frac{n_2\pi}{L_y}\right)^2 \right) \tag{A.4}$$

where n refers to the mode index (n_1, n_2), E is the modulus of elasticity, μ is the Poison ratio and ρ be the density of the plate material. The function $\psi_n^{\delta_p}(p)$ is given by

$$\psi_n^{\delta_p}(p) = \frac{n_1\pi}{L_x}\cos(\delta_p)\cos\left(\frac{n_1\pi x_p}{L_x}\right)\sin\left(\frac{n_2\pi y_p}{L_y}\right) + \frac{n_2\pi}{L_y}\sin(\delta_p)\sin\left(\frac{n_1\pi x_p}{L_x}\right)\cos\left(\frac{n_2\pi y_p}{L_y}\right) \tag{A.5}$$

where (x, y) are the coordinates of the point p and δ_p is the angle made by the moment axis with the x axis. Note that for the primary (or secondary) patch, $\delta_{p_i}(\text{or}\,\delta_{s_i}) = 0$, $\pi/2$, π and $3\pi/2$ for all elements i along edges 1, 2, 3 and 4 respectively.

The total power input due to the primary patch is given by

$$\bar{P}_p = \frac{1}{2}\text{Re}\left(M_p^* \sum_i W_{p_i}\right) \tag{A.6}$$

Using (A.1) and (A.2) in (A.6), the total input power due to the primary patch can be expressed as

$$\bar{P}_p = \frac{1}{2}\text{Re}\left(M_p^* P_{pp} M_p + M_p^* P_{ps} M_s\right) \tag{A.7}$$

where P_{pp} represents the equivalent angular mobility due to the primary patch given by

$$P_{pp} = \sum_i \sum_j P_{p_i p_j} \tag{A.8}$$

and P_{ps} represent the cross angular mobility given by

$$P_{ps} = \sum_i \sum_j P_{p_i s_j} \tag{A.9}$$

Similarly, the total power input due to the secondary patch can be shown to be

$$\bar{P}_s = \frac{1}{2}\mathrm{Re}\left(M_s^* P_{sp} M_p + M_s^* P_{ss} M_s\right) \tag{A.10}$$

where $P_{sp} = P_{ps}$ represents the cross angular mobility and

$$P_{ss} = \sum_i \sum_j P_{s_i s_j} \tag{A.11}$$

represents the equivalent angular mobility due to the secondary patch.

Appendix B

Total Input Power and Global Energy

The modal response of the structure can be written as

$$w(\omega, x, y) = \sum_i q_i(\omega)\phi_i(x, y) \tag{B.1}$$

where $\phi_i(x, y)$ is the mode shape,

$$q_i(\omega) = \frac{1}{m}\frac{f_i}{\Omega_i}$$

is the complex modal amplitude, m is the mass,

$$f_i = \sum_k F_k(\omega)\phi_i(x_k, y_k)$$

is the modal force and

$$\Omega_i(\omega) = \omega_i^2(1 + j\eta_i) - \omega^2$$

is the modal frequency factor where ω_i is the natural frequency and η_i is the loss factor. The overall time averaged kinetic energy and potential energy of the structure can be written as [41]

$$\overline{E}_{kin} = \frac{m\omega^2}{4}\sum_i |q_i|^2 \tag{B.2}$$

$$\overline{E}_{pot} = \frac{m}{4}\sum_i w_i^2|q_i|^2 \tag{B.3}$$

Similarly, the total input power can be expressed in terms of the modal amplitudes as

$$\bar{P} = \frac{m\omega}{2}\sum_i \eta_i w_i^2|q_i|^2 \tag{B.4}$$

Iin general there is no simple relation between $\bar{P}$ and $\overline{E}_{kin}$ and $\overline{E}_{pot}$. However, if the forcing frequency is close to the natural frequency, then the total input power can be relation to the total vibrational (kinetic) energy. If $\omega \approx \omega_i$, then a single mode dominates the response. In such a case, we have

$$\overline{E}_{kin} = \overline{E}_{pot} \approx \frac{m\omega_i^2}{4}|q_i|^2 \tag{B.5}$$

$$\bar{P} \approx \frac{m\omega_i}{2}\eta_i w_i^2|q_i|^2 \tag{B.6}$$

Thus, we have

$$\bar{P} = 2\eta_i\omega_i\overline{E}_{kin} \Rightarrow \overline{E}_{kin} = \frac{\bar{P}}{2\eta_i\omega_i} \tag{B.7}$$

Thus

$$\min \bar{P} \equiv \min \overline{E}_{kin} \tag{B.8}$$

That is, minimizing the total input power is equivalent to minimizing the total vibrational energy.

When the excitation frequency is not close to the resonant frequency, that is, $\omega \not\approx \omega_i$, then we can relate the total input power to the potential energy of the structure. Assume that

the loss factor is the same for all modes. That is, $\eta_i = \eta$ for all i. In this case, comparing (B.3) and (B.4), we get

$$\bar{P} = 2\eta\omega\overline{E}_{pot} \tag{B.9}$$

The net input power is proportional to the potential energy at all frequencies. Thus, in this case

$$\min \bar{P} \equiv \min \overline{E}_{pot} \tag{B.10}$$

That is, minimizing the net input power is equivalent to minimizing the total potential energy

If there is high modal overlap, it can be argued that

$$\overline{E}_{pot} \approx \overline{E}_{kin}$$

for all frequencies except below the first resonance frequency. The argument is as follows [41]

"Below the resonance potential energy of a particular mode is larger than kinetic, while the opposite applies above the resonance. In the case of high modal overlap, at any particular excitation frequency, the (lower) kinetic energy of modes having the eigenvalues above the excitation frequency will become compensated by the (higher) kinetic energy of lower modes. Inverse compensation effect will apply to potential energy. As a result, the global kinetic and potential energies in modally overlapped systems can be shown to match closely at all frequencies except below the first resonance where the compensation cannot take place"

That is,

$$\bar{P} \approx 2\eta\omega\overline{E}_{kin} \tag{B.11}$$

for all $\omega \geq \omega_1$. Thus,

$$\min \bar{P} \equiv \min \overline{E}_{kin} \tag{B.12}$$

Thus, in general, if there is high modal overlap and if the loss factor is same for all modes, then minimizing the total input power is equivalent to minimizing the total vibrational energy for all frequencies except below the first resonance frequency.

REPORT DOCUMENTATION PAGE

Form Approved
OMB No. 0704-0188

1. REPORT DATE *(DD-MM-YYYY)*	2. REPORT TYPE	3. DATES COVERED *(From - To)*
01-01-2014	Contractor Report	

4. TITLE AND SUBTITLE

Active Vibration Control for Helicopter Interior Noise Reduction Using Power Minimization

5a. CONTRACT NUMBER
NNL11AA06C

5b. GRANT NUMBER

5c. PROGRAM ELEMENT NUMBER

6. AUTHOR(S)

Mendoza, J.; Chevva, K.; Sun, F.; Blanc, A.; Kim, S. B.

5d. PROJECT NUMBER

5e. TASK NUMBER

5f. WORK UNIT NUMBER
380046.02.07.04.01.05

7. PERFORMING ORGANIZATION NAME(S) AND ADDRESS(ES)

NASA Langley Research Center
Hampton, Virginia 23681

8. PERFORMING ORGANIZATION REPORT NUMBER

9. SPONSORING/MONITORING AGENCY NAME(S) AND ADDRESS(ES)

National Aeronautics and Space Administration
Washington, DC 20546-0001

10. SPONSOR/MONITOR'S ACRONYM(S)
NASA

11. SPONSOR/MONITOR'S REPORT NUMBER(S)
NASA/CR-2014-218147

12. DISTRIBUTION/AVAILABILITY STATEMENT

Unclassified - Unlimited
Subject Category 71
Availability: NASA CASI (443) 757-5802

13. SUPPLEMENTARY NOTES

Langley Technical Monitor: Randolph H. Cabell

14. ABSTRACT

This report describes work performed by United Technologies Research Center (UTRC) for NASA Langley Research Center (LaRC) under Contract NNL11AA06C. The objective of this program is to develop technology to reduce helicopter interior noise resulting from multiple gear meshing frequencies. A novel active vibration control approach called Minimum Actuation Power (MAP) is developed. MAP is an optimal control strategy that minimizes the total input power into a structure by monitoring and varying the input power of controlling sources. MAP control was implemented without explicit knowledge of the phasing and magnitude of the excitation sources by driving the real part of the input power from the controlling sources to zero. It is shown that this occurs when the total mechanical input power from the excitation and controlling sources is a minimum. MAP theory is developed for multiple excitation sources with arbitrary relative phasing for single or multiple discrete frequencies and controlled by a single or multiple controlling sources. Simulations and experimental results demonstrate the feasibility of MAP for structural vibration reduction of a realistic rotorcraft interior structure. MAP control resulted in significant average global vibration reduction of a single frequency and multiple frequency excitations with one controlling actuator. Simulations also demonstrate the potential effectiveness of the observed vibration reductions on interior radiated noise.

15. SUBJECT TERMS

control; excitation; noise; reduction; simulation; structural; vibration

16. SECURITY CLASSIFICATION OF:			17. LIMITATION OF ABSTRACT	18. NUMBER OF PAGES	19a. NAME OF RESPONSIBLE PERSON
a. REPORT	b. ABSTRACT	c. THIS PAGE			STI Help Desk (email: help@sti.nasa.gov)
					19b. TELEPHONE NUMBER *(Include area code)*
U	U	U	UU	202	(443) 757-5802